MM-Wave RF-MEMS Switches in SiGe BiCMOS Technologies

vorgelegt von
M. Sc.
Selin Tolunay Wipf

an der Fakultät IV – Fakultät Elektrotechnik und Informatik
der Technischen Universität Berlin
zur Erlangung des akademischen Grades

Doktor der Ingenieurwissenschaften
- Dr.-Ing. -

genehmigte Dissertation

Promotionsausschuss:

Vorsitzender:	Prof. Dr.-Ing. Friedel Gerfers
Gutachter:	Prof. Dr.rer.nat. Bernd Tillack
Gutachter:	Prof. Dr.-Ing. Wolfgang Heinrich
Gutachter:	Prof. Dr.-Ing. Ingmar Kallfass

Tag der wissenschaftlichen Aussprache: 24. September 2019

Berlin 2020

Copyright

Abstract

In the last decade, silicon germanium (SiGe) bipolar complementary metal oxide semiconductor (BiCMOS) technologies opened a new cost-efficient market for the mm-wave applications. Starting with the commercial use of automotive radars at 77 GHz, the market now has a strong interest on radar, sensor and imaging products at mm-wave and sub-THz frequencies. The latest developments on SiGe hetero bipolar transistors (HBTs) with an f_{max} of beyond 700 GHz boost the research and development effort on circuit and system areas to take share from the new market. In parallel to the developments on SiGe HBT performances, extra functionalities to the standard BiCMOS processes can be added by following the "More than Moore" path. With the followed path, different modules that include photonics, microfluidics or micro-electro- mechanical system (MEMS) can be integrated into the circuits and systems for multi-functionality. Radio frequency micro- electro- mechanical system (RF-MEMS) switches can offer very high RF isolation, very low insertion loss, high signal linearity, almost zero power consumption, very large bandwidth and miniaturization. With their superior RF performances they can be used in switching and reconfigurable matching networks, phase arrays or active circuits.

In this thesis, mm-wave RF-MEMS switches in SiGe BiCMOS technologies are developed. Initially the process integration of the RF-MEMS switches is presented, including different wafer-level packaging approaches. The process integration is followed by electromagnetic modeling and RF optimization of a thin film wafer-level encapsulated RF-MEMS switch for D-band (110 – 170 GHz) applications in 0.13 µm SiGe BiCMOS technology. After the demonstration of the D-band switch, a second type of switch in 0.13 µm SiGe BiCMOS technology is developed and demonstrated for J-band (220 – 325 GHz) applications. The thesis continues with different RF-MEMS design examples in both 0.25 µm and 0.13 µm SiGe BiCMOS technologies. In the 0.13 µm SiGe BiCMOS technology, an RF-MEMS based D-band single-pole double-throw (SPDT) switch and in the 0.25 µm SiGe BiCMOS technology, wafer-level packaged K-band (18–27 GHz) single-pole single-throw (SPST), RF-MEMS based SPDT switches and a charge pump with the SPST switch are demonstrated. Lastly, yield analyses of the developed examples in the 0.25 µm SiGe BiCMOS technology are given.

Zusammenfassung

In den vergangenen zehn Jahren sind die SiGe BiCMOS Technologien in den Markt der mm-Wellen Anwendungen vorgedrungen. Beginnend mit dem kommerziellen Einsatz von Autoradarsystemen bei 77 GHz, hat der Markt nun ein großes Interesse an Radar, Sensor und Bildgebungsprodukten bei mm-Wellen und Sub-THz Frequenzen. Die neuesten Entwicklungen auf dem Gebiet der SiGe HBT mit einem f_{max} von mehr als 700 GHz beschleunigen die Forschungs und Entwicklungsanstrengungen in den Bereichen Schaltkreise und Systeme, um vom neuen Markt zu profitieren. Parallel zu den Fortschritten bei den SiGe HBT Eigenschaften werden, der "More than Moore" Strategie entsprechend, zusätzliche Funktionalitäten in den BiCMOS Prozess integriert. Demzufolge, können verschiedene Module wie zum Beispiel Photonik, Mikrofluidik oder MEMS in den Schaltungen und Systemen verwendet werden, wodurch deren Funktionalität deutlich erweitert wird. RF-MEMS Schalter haben eine sehr hohe HF-Isolation, eine sehr geringe Einfügedämpfung, eine hohe Signallinearität, nahezu keine Leistungsaufnahme, eine sehr große Bandbreite und sind sehr kompakt. Mit ihren hervorragenden HF-Eigenschaften können sie als HF-Schalter, in konfigurierbaren Anpassungsnetzwerken, in Phasenschieber Schaltungen und in aktiven Schaltungen eingesetzt werden. In dieser Arbeit wurden mm-Wellen RF-MEMS Schalter in zwei SiGe BiCMOS Technologien entwickelt. Zunächst wird die Prozessintegration der RF-MEMS nebst verschiedenen Verkapselungskonzeptenen vorgestellt. Auf die Prozessbeschreibung folgt die elektromagnetische Modellierung und HF-Optimierung eines, mittels Dünnfilm auf Wafer-Level, verkapselten RF-MEMS Schalters für D-Band Anwendungen in einer 0.13 µm SiGe BiCMOS Technologie. Im folgenden Abschnitt wird die Entwicklung eines zweiten Schalters in derselben Technologie für J-Band Anwendungen beschreiben. Die Dissertation setzt mit RF-MEMS Designbeispielen aus der 0.25 µm und der 0.13 µm SiGe BiCMOS Technologie fort. In der 0.13 µm SiGe BiCMOS Technologie wurde ein RF-MEMS D-Band SPDT Schalter und in der 0.25 µm Technologie ein auf Wafer-Level verkapselter K-Band SPST Schalter, ein RF-MEMS SPDT Schalter und ein mittels integrierter Ladungspumpe gesteuerter SPST Schalter entworfen. Abschließend wird die Ausbeute der entwickelten Demonstratorschaltungen aus der 0.25 µm SiGe BiCMOS Technologie dargestellt und diskutiert.

Acknowledgment

First of all, I would like to thank my 'Doktor-Vater' Prof. Dr. Bernd Tillack for providing me the opportunity to work in IHP on my PhD thesis. I would like to express my special gratitude to my supervisor, Dr. Mehmet Kaynak, for all his support and technical guidance throughout all these years.

I am very thankful to my colleagues, Alexander Göritz and Matthias Wietstruck who I have worked with on RF–MEMS switches. Without their support, it would have been a much more difficult journey.

I appreciate my colleagues from Heterointegration of Devices and Technologies group and Electrical Characterization group of IHP for their friendship and technical support.

Finally, my deepest gratitude goes to my husband Christian Wipf, my mother Zuhal Tolunay and my father Ahmet Engin Tolunay who were always there for me with their unconditional love and endless support. Without them I would not manage to finalize my PhD journey successfully.

Contents

Glossary

AlCu	aluminum copper
AR	aspect ratio
BEOL	back-end-of-line
BiCMOS	bipolar complementary metal oxide semiconductor
C-V	Capacitance-Voltage
CMOS	complementary metal oxide semiconductor
CMP	chemical mechanical polishing
CO_2	carbon dioxide
CP	charge pump
DC	direct current
DEC	dynamic evaluation circuit
DHBT	double hetero bipolar transistor
EDX	energy dispersive X-ray
EM	electromagnetic
ESCC	European Space Components Coordination
FEM	finite-element-method
FEOL	front-end-of-line
FET	field-effect transistor
FIB	focus ion beam
GSG	ground signal ground
GSGSG	ground signal ground signal ground
GSM	global system for mobile communications
HBT	hetero bipolar transistor

HDR	high deposition rate
HFVPE	hydrofluoric acid vapor phase etching
HV	high-voltage
IC	integrated circuit
IL	insertion loss
InP	indium phosphide
ISO	isolation
ISS	impedance standard substrate
LDV	laser-doppler-vibrometer
LRM+	Thru-Reflect-Match plus
LRRM	Thru-Reflect-Reflect-Match
LTE	long-term evolution
M1	Metal1
M2	Metal2
M3	Metal3
M4	Metal4
M5	Metal5
MEMS	micro- electro- mechanical system
MIM	metal-insulator-metal
MIMO	multiple input multiple output
PECVD	plasma enhanced chemical vapor deposition
RF-MEMS	Radio frequency micro- electro- mechanical system
RIC	representative integrated circuit
RIE	reactive ion etching
SEM	scanning electron microscopy
Si	silicon
Si_3N_4	silicon nitride
SiGe	silicon germanium
SiO_2	silicon dioxide
SL	signal line

SOI	silicon on isolator
SOLT	short open load thru
SPDT	single-pole double-throw
SPST	single-pole single-throw
SW#1	switch-1
SW#2	switch-2
TCV	technology characterization vehicle
T-line	transmission line
T/R	transmit/receive
TiN	titanium nitride
TM1	TopMetal1
TM2	TopMetal2
VNA	vector network analyzer
WLE	wafer-level encapsulated
WLP	wafer-level packaging

List of symbols

A	area of two parallel plates	m^2
C_{cont}	contact air capacitance of RF-MEMS switch	F
C_{elec1}	parasitic capacitance between membrane and left side HV electrode	F
C_{elec2}	parasitic capacitance between membrane and right side HV electrode	F
$C_{encapSL1}$	lumped-1 capacitance between TM2 plate and M5 RF-SL	F
$C_{encapSL2}$	lumped-2 capacitance between TM2 plate and M5 RF-SL	F
$C_{encapSL3}$	lumped-3 series lumped-1 capacitance between TM2 plate and M5 RF-SL	F
$C_{encapSL4}$	lumped-4 series lumped-1 capacitance between TM2 plate and M5 RF-SL	F
C_{off}	off-state/up-state contact air capacitance	F
C_{on}	on-state/down-state contact air capacitance	F
$C_{parallelplate}$	parallel-plate capacitance	F
C_{subst}	substrate capacitance between ground and RF-SL	F
d	distance between two parallel plates	m
d_{off}	off-state distance between membrane and RF-signal line	m
d_{on}	on-state distance between membrane and RF-signal line	m
ε_0	permittivity of free space	F/m
ε_r	relative permittivity of material between two paralel plates	
f_{max}	maximum oscillation frequency	Hz
f_T	unity current gain frequency	Hz
L_{arm}	inductance of membrane arm	H
L_{arm1}	inductance of the membrane arms (left side)	H
L_{arm2}	inductance of the membrane arms (right side)	H
L_{encap1}	lumped-1 series inductance of TM2 plate	H
L_{encap2}	lumped-2 series inductance of TM2 plate	H
L_{encap3}	lumped-3 series inductance of TM2 plate	H

L_{encap4}	lumped-4 series inductance of TM2 plate	H
L_{encap5}	lumped-5 series inductance of TM2 plate	H
L_{total}	total inductance of membrane, arms and ground-ring of RF-MEMS switch	H
R_{arm1}	series resistor of the membrane arms (left side)	Ω
R_{arm2}	series resistor of the membrane arms (right side)	Ω
R_{encap1}	lumped-1 series resistance of TM2 plate	Ω
R_{encap2}	lumped-2 series resistance of TM2 plate	Ω
R_{encap3}	lumped-3 series resistance of TM2 plate	Ω
R_{encap4}	lumped-4 series resistance of TM2 plate	Ω
R_{encap5}	lumped-5 series resistance of TM2 plate	Ω
R_{subst}	substrate resistance between ground and RF- SL	Ω
t_{off}	switch-off time of RF-MEMS switch	s
t_{on}	switch-on time of RF-MEMS switch	s

1 Introduction

1.1 Motivation and Background

New generation communication system technologies demand for not only miniaturization but also multifunctionality. In this point of view, MEMS technology is a promising option in order to add functionality to the RF systems. A variety of MEMS devices (switches [1, 2], tunable capacitors [3, 4], high-Q inductors [5, 6] and resonators [7, 8], etc.) are under study throughout the world since they serve as fundamental building blocks in telecommunication and radar systems for RF and mm-wave applications. In recent years, there is a growing need and interest in RF-MEMS switches for mm-wave application as a result of their low insertion-loss, high isolation, high linearity, near-zero power consumption and low fabrication cost [9].

The main interest of the microelectronic industry is on the commercial applications which operate below 40 GHz, thus; the developments of RF-MEMS switches in the literature are mostly in this frequency band. With the high performance semiconductor technologies, recently developed radar and imaging applications are moving towards the upper frequencies of the mm-wave spectrum. Specifically, SiGe BiCMOS technology is a proven technology for the mm-wave applications such as 77 GHz automotive radar [10], and is promising for the emerging applications such as 140 GHz radar front-ends for active imaging systems [11] or THz spectroscopic systems at 240 GHz and beyond [12]. For such high frequencies, complementary metal oxide semiconductor (CMOS) and BiCMOS technologies offer high speed transistors. Recently, 0.13 µm SiGe BiCMOS processes have reached a unity current gain frequency (f_T) of 505 GHz and a maximum oscillation frequency (f_{max}) of 720 GHz [13]. With the high performance HBTs, SiGe technologies have become more attractive for mm-wave frequency applications during the last decade.

Following the "More than Moore" approach [14], monolithic or hybrid integration techniques can provide different technology modules in the baseline technologies [15–17]. One of the modules that can be added into the CMOS or BiCMOS technologies is the RF-MEMS switch module. The decision of the integration technique for the RF-MEMS switch modules in CMOS/BiCMOS technologies is driven by different

factors. Compared to the monolithic integration of MEMS devices, the hybrid integration solutions such as interposer techniques, chip-to-wafer bonding, wafer-to-wafer bonding, or any other wafer stacking and 3D integration techniques offer more flexibility in terms of combining MEMS devices with CMOS/BiCMOS chips fabricated in different technologies. Since MEMS devices have larger sizes compared to standard CMOS/BiCMOS devices; the cost per chip including CMOS/BiCMOS circuits and MEMS devices together are increased in case of monolithic integration. However, against the flexibility of the hybrid integration, the monolithic integration has four main advantages. In [18], these main advantages are defined as; "1) miniaturization, 2) single-chip integration offering low manufacturing/testing cost for large-volume production, 3) reduction of parasitic effects due to the use of on-chip interconnects, and 4) improvement of device sensitivity and signal-to-noise ratio due to the close proximity of the electronics (amplifiers and read out circuits) to the MEMS device".

In the past, RF-MEMS switches have been demonstrated with high isolation in W-band (75 – 110 GHz) [19]. On the other side, the monolithically integrated RF-MEMS switches have shown low insertion loss (IL) (<0.5 dB) up to 140 GHz in 2010 [20] and recently up to 300 GHz [21]. At such high frequencies, the integration of the RF-MEMS switches together with the other system blocks requires minimum parasitics to minimize the undesired effects. Parasitic losses can be minimized with shorter connections to the active circuits with monolithic integration of the RF-MEMS switches in SiGe technologies. The integration of the RF-MEMS switches into a 0.25 µm SiGe BiCMOS technology has been firstly demonstrated in [22] and showed valuable results for this integration technique with respect to robustness and reliability [23]. The monolithic integration of the RF-MEMS switch into 0.13 µm SiGe BiCMOS process technology gives the possibility to use RF-MEMS components together with very high performance HBTs [13, 24] and provides circuits with unprecedented low attenuation, to be used as SPDT switches [25] in phased arrays [26, 27]. In [25], a transceiver integrated circuit (IC) with novel fully integrated differential RF-MEMS SPDT switch for short-range F-band radar systems is presented in IHP's 0.13 µm SiGe BiCMOS technology. Shortly, IHP's 0.13 µm SiGe BiCMOS technology is well-fitting for the RF and mm-wave applications with the high performance HBTs and the CMOS devices and gives the possibility to integrate the on-chip MEMS actuation circuitry.

Although the RF-MEMS switches have shown that they can provide good RF performances in all the mm-wave range, packaging is still the challenge on the way to their commercialization [28]. Similar to the all other electronic components, a good RF-MEMS package should not only provide the interface to the next level, but should

also be cost and area effective. However, the packaging of the RF-MEMS devices is more complex than the packaging of the other electronic components since there is a need for a cavity inside the package. Moreover, the type of package has also a significant effect on their long term reliabilities. Besides, it should be preferably fabricated using the wafer-level processes to increase the throughput since thousands of RF-MEMS devices can be fabricated on a single 8-inch wafer.

The main motivation of this thesis is to expand the operating frequency range of high performance RF-MEMS switches for the future need of the market on the mm-wave applications such as radar, imaging and spectroscopy.

Main objectives of this thesis are:

- Design, electromagnetic (EM) modeling and RF optimization of a thin film wafer-level encapsulated (WLE) RF-MEMS switch for D-band (110 – 170 GHz) applications.
- Design and EM modeling of an RF-MEMS SPST switch in J-band (220 – 325 GHz) and an RF-MEMS SPDT switch at 140 GHz targeted frequency with beyond state-of-the-art performance figures in D-band (110 – 170 GHz).
- Yield analysis and the effect of the silicon (Si) cap packaging of K-band (18 – 27 GHz) RF-MEMS test vehicles.

1.2 Status of the RF-MEMS switch technologies

1.2.1 RF-MEMS switches - Principle of operation

RF-MEMS switches can be divided into four groups in terms of actuation principles; electrostatic [29–31], piezoelectric [32–34], electrothermal [35, 36] and electromagnetic [37]. Most of the developed RF-MEMS switches are based on electrostatic actuation and their main advantages are their simplicity in technological implementation, fast switching and low power consumption [38]. Electrostatically actuated switches can be divided into two basic types with a contact perspective; capacitive and ohmic switches. The top and cross sectional views of capacitive and ohmic RF-MEMS switches are shown in Fig. 1.1.

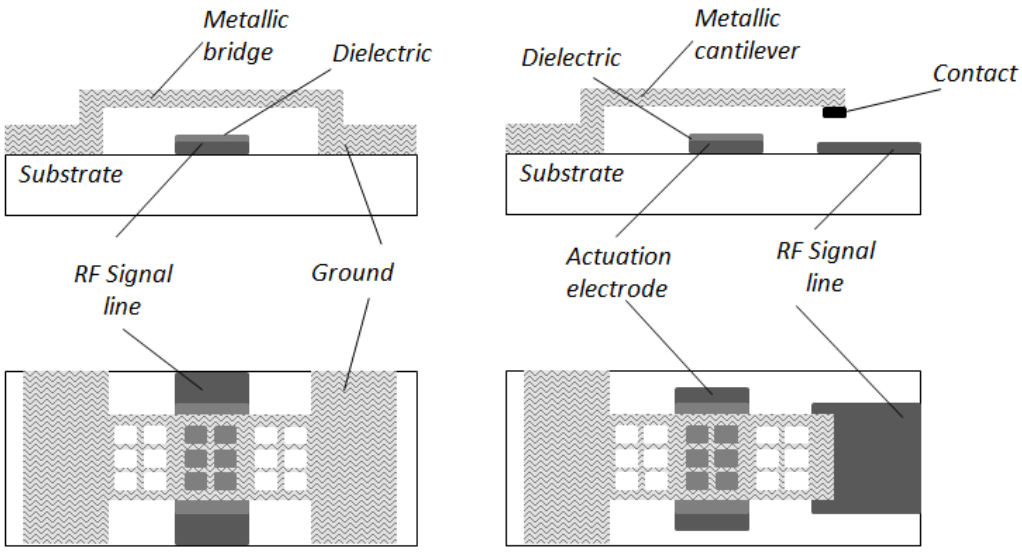

(a) (b)

Figure 1.1: Cross-sectional and top views of (a) capacitive shunt and (b) ohmic series types of RF-MEMS switches.

Capacitive Switches with electrostatic actuation:

Capacitive type of RF-MEMS switches can switch the RF signal on and off with the low and high capacitances in the contact region. When the movable membrane is in the upper position, it provides low capacitance to the RF- signal line (SL). By applying a high-voltage (HV) between the RF- SL and the grounded membrane, the movable membrane moves closer to the RF- SL and provides a high capacitance. The high contact capacitance creates a LC series resonance together with the inductance of the movable membrane. The dielectric on top of the RF- SL provides direct current (DC) isolation between the RF- SL and the movable membrane. Although the capacitive type of RF-MEMS switches can be used in both shunt and series circuit configurations, the typical circuit configuration with the capacitive type of RF-MEMS switches is the shunt configuration.

Ohmic Switches with electrostatic actuation:

Ohmic type of RF-MEMS switches can switch the RF signal on and off with the low and high ohmic contacts. In the up-state, the ohmic switch creates an open between the RF- SL and the movable membrane. On the other side, in the down-state RF-signal is shorted to the movable membrane with the low contact resistance. Although the ohmic type of RF-MEMS switches can be used in both shunt and series circuit configurations, the typical circuit configuration with the ohmic type of RF-MEMS switches is the series configuration.

The performance of the ohmic RF-MEMS switches in down-state is limited by the contact resistance and the switch inductance that increases with higher frequencies. On the other side, the limitation for the capacitive RF-MEMS switches is the down-state capacitance. To be able to provide a short circuit at lower frequencies very high capacitances need to be achieved. However to achieve a high down-state capacitance is not preferable due to the necessity of a bulky RF-MEMS switch.

Briefly, the ohmic RF-MEMS switches are more suitable for applications below mm-wave and the capacitive RF-MEMS switches are more suitable for applications at mm-wave and also above. In this thesis, capacitive RF-MEMS switches are chosen due to the targeted mm-wave frequency applications.

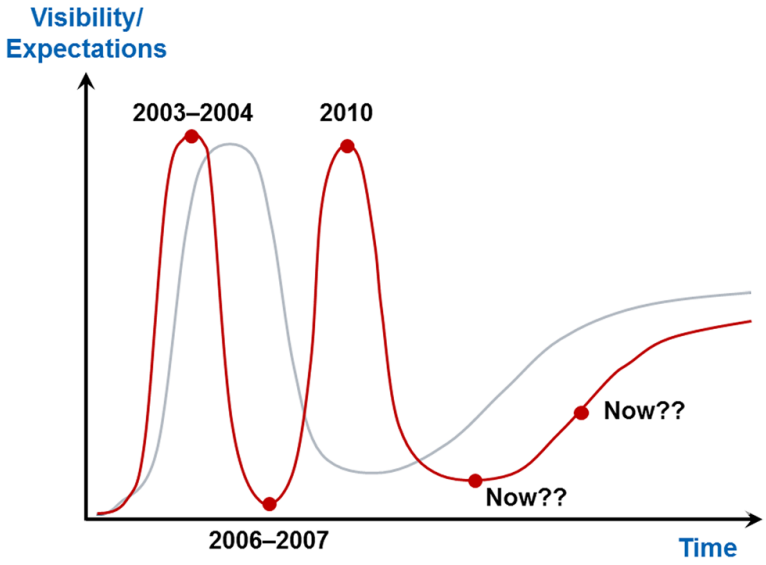

Figure 1.2: "Behaviour of the hype curve [45] of RF-MEMS technology based upon the market forecasts published through the last decade and the fluctuating expectations for mass-market outcomes [39]".

1.2.2 Market overview of RF-MEMS devices

In the beginning of the 21th century, market volume expectations for RF-MEMS devices are reported with a focus on their expected impacts in the mass production of mobile handsets. The reported market volumes for RF-MEMS devices are reviewed in [39] and itemized below;

- 2004–2005: "The market volume was expected to reach from 700 $M (Millions of US Dollars) to 1 $B (Billions of US Dollars) in 2009 [40]".
- 2009: "WTC in 2006 predicted a downsized market volume of around 10 $M in 2009 and 70 $M in 2011 [41]".
- 2010: "IHS Inc. consolidated the RF-MEMS market figure to a few $M in 2009, and predicted a volume of 225 $M in 2014 [42]".
- 2012: "IHS Inc. in 2012 shrunk down the forecast for 2014 market to less than 100 $M [43]".
- 2013: "Yole Developpement estimated a market volume of around 50 $M in 2014 and of less than 350 $M in 2018 [44]".

By summarizing the above given market forecasts, [39] has published the graphical presentation (Fig. 1.2) for the expected mass-market outcomes of the RF-MEMS technology with respect to the years. It has been stated in [39, 46] that RF-MEMS experienced two peaks for the expectations followed by disappointments. The first disappointment phase was in around 2006-2007 which was linked with intrinsic factors as reliability, packaging and integration. Since researchers started to address these intrinsic problems, extrinsic factors were to be faced for the success of the technology. These were not directly linked to the technology itself but the needs and the acceptance of the market. The market was not strong enough to demand high performance and reconfigurable devices.

With the new full screen smartphones, the quality of the communication degraded as the mobile smartphones became smaller and thinner which made it difficult to incorporate the performance-enhancing circuitry required to counter dropped cellphone calls and raise voice quality [47]. Fig. 1.3 shows the degradation of connection quality with each generation of communication, from global system for mobile communications (GSM) to long-term evolution (LTE) [48]. Since the smartphones had low antenna efficiency due to multi band operation, the market needed tunable antennas to overcome this problem [49] and a change in the strategy [46]. In the recent few years within this scenario, RF-MEMS adaptive impedance tuners started to get into the consumer market of 4G - LTE smartphones [50]. Although the demanded reconfigurability of the tunable antennas can be realized by integrating pin diodes [51], varactors [52, 53], or MEMS [54–56]; the RF-MEMS devices differs with better performance (in terms of Q, isolation, and linearity) but have the disadvantage of higher cost for the technology [57].

The growing market interest for the RF-MEMS based products is expected to become much bigger especially with the 5G mobile devices [46]. Nevertheless, before the 5G mobile devices, an RF-MEMS device in a Samsung cellphone, Focus Flash, is identified by a research firm IHS in 2012. The identified device was an RF-MEMS based adaptable impedence tuner which was manufactured by WiSpry [58] and it became the first known RF-MEMS based volume-shipped products [59]. Fig. 1.4 shows the cross-section of a complete WiSpry MEMS capacitor with an integrated charge pump (CP) [60].

In the following years, in 2014, Cavendish Kinetics [48] and Chinese ZTE Corporation announced that Nubia Z7 smartphone includes a smart antenna that is powered by Cavendish Kinetics‘ SmarTune antenna tuning solution. “Our revolutionary SmarTune antenna tuning solution controls the electrical characteristics of the antenna and

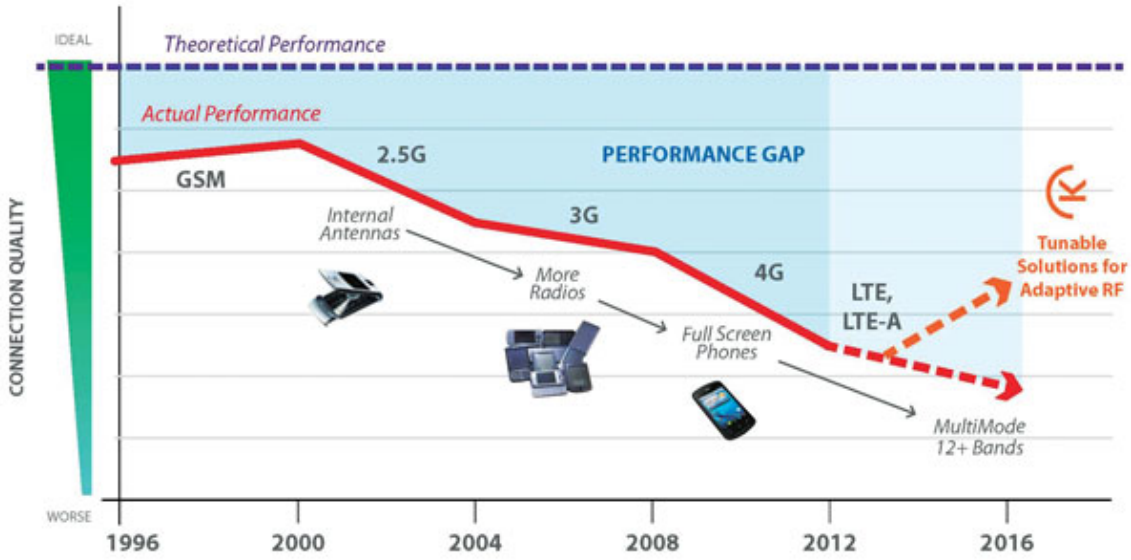

Figure 1.3: The degradation of connection quality with each generation of communication, from GSM to LTE due to greater use of cellular communications. This problem is addressed to be solved by RF-MEMS tuning [48].

optimizes its performance by shifting its resonating frequency, so that it is always optimally matched to the operating frequency," said Paul Dal Santo, CEO of Cavendish Kinetics [61]. Fig. 1.5 shows the MEMS array inside Cavendish Kinetics' SmarTune antenna tuner [62]. In 2015, Cavendish Kinetics announced that they shipped the SmarTune solution in five different smartphone models to optimize the performance of LTE multiple input multiple output (MIMO) antenna; and in 2017, it announced that ten manufacturers for 40 different smartphone models (including the Samsung Galaxy A8), have adopted their SmarTune RF MEMS antenna tuners. Cavendish Kinetics claims that their "RF-MEMS Tuners outperform traditional silicon on isolator (SOI) switch based antenna tuning solutions by 2-3 dB, resulting in much higher data rates (up to double) and improved battery life (up to 40%)" and states that the smartphone manufacturers recognize the benefit of aperture tuning over impedance matching, and find that the SmarTune solution allows them to design high efficiency antennas for slimmer smartphones, without sacrificing radio performance [61].

Other examples for RF-MEMS devices that are commercially available since 2016 in the market are ADGM1304 and ADGM1004 MEMS switches for 0 Hz (DC) to 14 GHz operation frequencies from Analog Devices [63]. The introduced switches are hermetically sealed in Si cap and contain two dies including driver circuits and MEMS

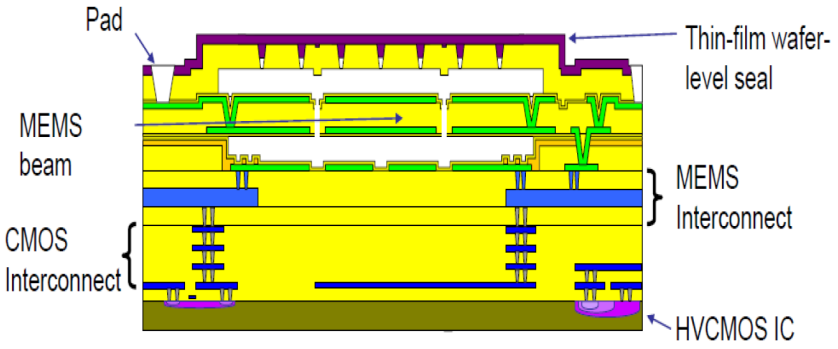

Figure 1.4: Cross-section of the complete WiSpry MEMS capacitor with an integrated CP [60].

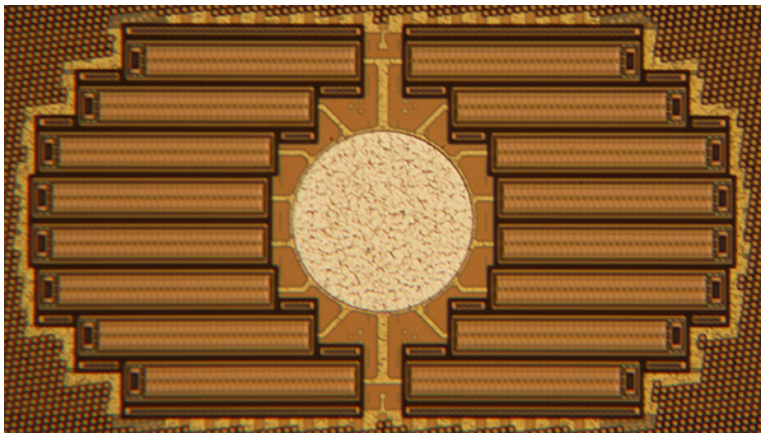

Figure 1.5: "MEMS array inside Cavendish Kinetics' antenna tuner" [62].

switch. Fig. 1.6 shows the commercially avaible MEMS switch technology of Analog Devices. Analog Devices claims that the introduced MEMS switches are "95 percent smaller, 30 times faster, 10 times more reliable, and use 10 times less power than conventional electromechanical relays" and with their superior performances can replace electromechanical relays (in e.g. automatic test equipments) [64].

In summary, RF-MEMS technology solutions are getting more attention as they become more mature. Larger market volumes for RF-MEMS based products are expected in the future, especially concerning the 5G mobile devices and communication infrastructures [46]. As a result of this demand, it is expected that the hyper curve of RF-MEMS technology will look more pleasant in the future.

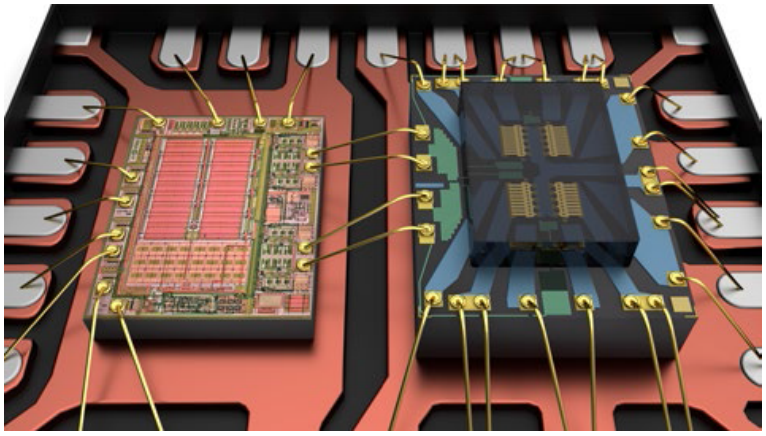

Figure 1.6: "MEMS switch technology of Analog Devices with driver circuits (Left) and MEMS switch (Right) mounted on and wire bonded to a metal lead frame" [64].

1.3 Structure of the thesis

This thesis begins with the process integration chapter of RF-MEMS switches in IHP's high performance SiGe BiCMOS technologies. These monolithically integrated RF-MEMS switches are real single chip solutions with the advantages of miniaturization and minimum parasitics compared to the hybrid integrated switches. Although the process integration of the RF-MEMS modules [65] are not in the main work of this thesis, the thesis begins with the general process flows of the RF-MEMS modules in Chapter 2 to give a better understanding for the electromagnetically modeled and characterized RF-MEMS switches in the following chapters. Additional to the general process flows of the RF-MEMS modules, the two different packaging approaches for the RF-MEMS switches are also briefly explained in Chapter 2. In short, for the 0.25 µm SiGe BiCMOS technology a Si cap wafer-level packaging technique and for the 0.13 µm SiGe BiCMOS technology a thin film wafer-level encapsulation technique is selected.

The developed RF-MEMS switches target applications in mm-wave with a special focus on above 110 GHz applications. The main work of this thesis is given in Chapter 3 and presents the D-band and J-band RF-MEMS switches in 0.13 µm SiGe BiCMOS technology. More specifically, Chapter 3 presents initially an EM model and a small-signal (lumped-element) model of RF-MEMS switches in D-band and J-band. The EM model of the RF MEMS switches are developed to be able to roughly estimate the RF performances before their fabrications. After the fabrication of the switches, the developed EM models are used to get accurate S-parameter simulation results. In

parallel as alternative to the EM models, the small-signal models of the fabricated RF-MEMS switches are developed for faster simulations to predict the RF performances of the switches from a pure electrical point of view. The experimental results of the 0.13 µm SiGe BiCMOS embedded RF-MEMS switches show beyond state of the art RF performances in D-Band and J-band with high on- off-state contact capacitance ratios (C_{on} / C_{off}).

Chapter 4 presents different RF-MEMS design examples in the both SiGe BiCMOS technologies. Specifically, it presents a D-band RF-MEMS SPDT switch including the EM modeling and experimental results, and K-band RF-MEMS test vehicles including the experimental results, yield analysis and investigation for the effect of the Si cap packaging on RF performances.

Finally, Chapter 5 gives the conclusion of the thesis and includes the future perspective of this work.

2 Technology

2.1 Introduction

Integration of MEMS devices with CMOS electronics can be done in different approaches; pre-CMOS, intra-CMOS, post-CMOS and post processing of CMOS-BEOL layers. These four approaches are summarized in [18]: In pre-CMOS approach MEMS devices are fabricated before the CMOS devices; in intra-CMOS approach they are fabricated in parallel; in post-CMOS approach MEMS devices are fabricated after the CMOS devices and in post processing of CMOS-BEOL layers approach MEMS are embedded in CMOS BEOL layers. Each approach has its advantages and limitations, and should be selected accordingly.

Monolithic integrations of RF-MEMS devices into BiCMOS BEOL have advantages in terms of stable process conditions and minimum parasitics, however it also has risk of yield degradation for the CMOS devices. The yield degradation of CMOS devices must be avoided by keeping the stress level of the complete stack, front-end-of-line (FEOL) and BEOL. In 2009, process integration of RF-MEMS module into IHP's 0.25 µm SiGe BiCMOS technology was demonstrated [22]. For the success of the integration, it was necessary to optimize the mechanical stress of the metalization layer (Metal3 (M3)) used for the movable membrane. The developed M3 recipe did not significantly affect the M3 sheet resistance and the requirement of the process specifications were still fulfilled. In this thesis, the developed RF-MEMS devices are monolithically integrated into IHP's 0.25 µm and 0.13 µm BiCMOS BEOLs [66].

This chapter provides general overviews of the process integration of RF-MEMS modules in both IHP technologies; 0.25 µm (SG25) and 0.13 µm (SG13) SiGe BiCMOS technologies. Section 2.2 provides introduction of IHP's 0.25 µm SiGe BiCMOS technology, detailed information about the process integration of MEMS module in 0.25 µm node and the process flow of Si cap wafer-level packaging for the RF-MEMS switches. In the next section, Section 2.3, introduction of IHP's 0.13 µm SiGe BiCMOS technology, detailed information about the process integration of MEMS module in 0.13 µm node and the process flow of thin-film wafer-level encapsulation for the RF-MEMS switches are provided.

2.2 Integration of MEMS module in 0.25 µm SiGe BiCMOS Technology

IHP's 0.25 µm node has three main BiCMOS technologies; SG25H3 and SG25H4 and SGB25V. SGB25V technology includes 3 different HBTs with maximum f_{max} of 95 GHz. SG25H3 technology offers HBTs with f_{max} up to 180 GHz. The highest performance of 0.25 µm IHP technologies is the SG25H4 with the f_{max} values for HBTs up to 220 GHz. The main performance parameters of HBTs for different 0.25 µm technologies [67] are summarized in Table 2.1.

Table 2.1: Main performance parameters of HBTs for different 0.25 µm technologies of IHP [67].

SG25V	High Performance	Medium Voltage	High Voltage
f_{max}	95 GHz	90 GHz	70 GHz
f_T	75 GHz	45 GHz	25 GHz
BV_{CEO}	2.4 V	4 V	7 V

SG25H3	High Performance	Medium Voltage	High Voltage
f_{max}	180 GHz	140 GHz	80 GHz
f_T	110 GHz	45 GHz	25 GHz
BV_{CEO}	2.3 V	5 V	7 V

SG25H4	npn1	npn2
f_{max}	190 GHz	220 GHz
f_T	190 GHz	180 GHz
BV_{CEO}	1.9 V	1.9 V

The BEOL of the 0.25 µm SiGe BiCMOS technology offers three thin and two thick aluminum copper (AlCu) layers, and tungsten vias in between. The cross section of the FEOL with the detailed BEOL module is shown in Fig. 2.1. The thin metal layers are named from bottom to top as Metal1 (M1), Metal2 (M2), M3. The two thick metal layers are TopMetal1 (TM1) and TopMetal2 (TM2). Additionally, metal-insulator-metal (MIM) capacitor is available between M2 and M3 in order to achieve a high capacitance density of 1 fF/µm^2. The passivation on top includes thickness of 1.5 µm silicon dioxide (SiO_2) and 0.4 µm silicon nitride (Si_3N_4).

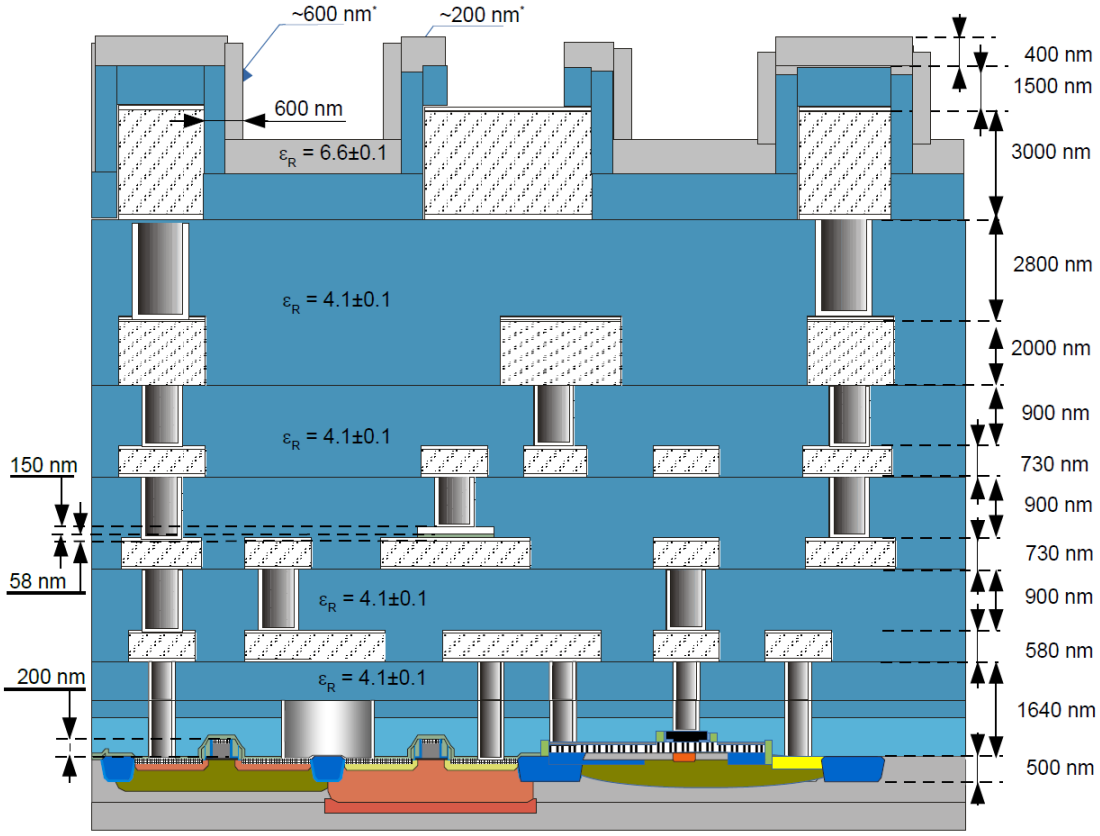

Figure 2.1: The cross section of the SG25H3/H4 BEOL [68].

2.2.1 Process integration of MEMS module

The integration of the RF-MEMS switches into a BiCMOS process gives the possibility to use them together with CMOS electronics and high performance HBTs [24]. The integration of the RF-MEMS switches into IHP's 0.25 µm SiGe BiCMOS technology was firstly demonstrated in [22] and showed valuable results with respect to robustness and reliability [23]. Fig. 2.2 summarizes the additional process steps for RF-MEMS switch integration into IHP's SG25 BiCMOS process. After finalizing the SG25 BiCMOS process, the first lithography step is done to determine the area of the RF-MEMS switch for the passivation nitride opening. Later on, it is followed by the reactive ion etching (RIE) process to open the passivation nitride in the determined MEMS area. After the RIE process, the second lithography step is done to determine the same MEMS area where the RF-MEMS switch will be wet etched from. Following the second lithography step, RF-MEMS switch is wet etched down to M1 where

the high voltage electrodes of the switch were patterned. Before finalizing the RF-MEMS switch integration, the wafer is cleaned and rinsed. Finally, the carbon dioxide (CO_2) critical point drying step is applied in order to prevent the unwanted stiction of the RF-MEMS switch after the suspended membrane is released by the wet etching.

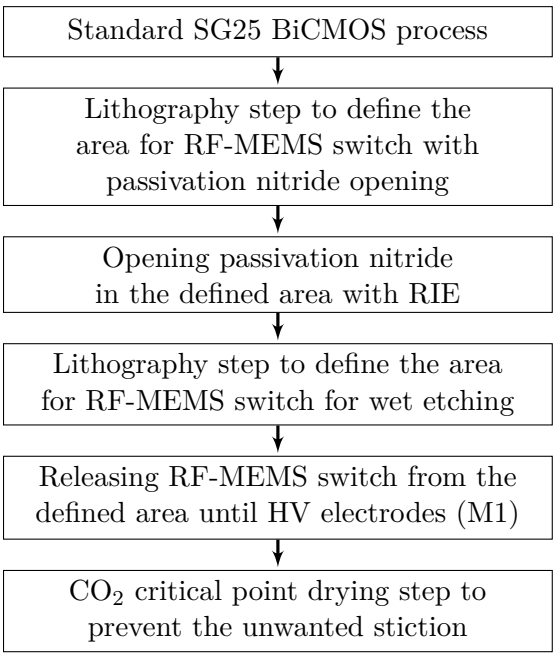

Figure 2.2: Additional process steps for RF-MEMS switch integration into the SG25 BiCMOS process.

Fig. 2.3 shows the cross section of the embedded SG25 RF-MEMS switches. The RF-MEMS switches are built between the M1 and the M3. The high-voltage electrodes are defined in M1, the RF-SL in M2 and the suspended membrane in M3. A thin Si_3N_4/ titanium nitride (TiN) stack, which is part of the BiCMOS MIM capacitor, forms the contact region and provides DC isolation between the grounded membrane and the RF-SL. The first generation SG25 BiCMOS embedded RF-MEMS switch is shown in Fig. 2.4 [22].

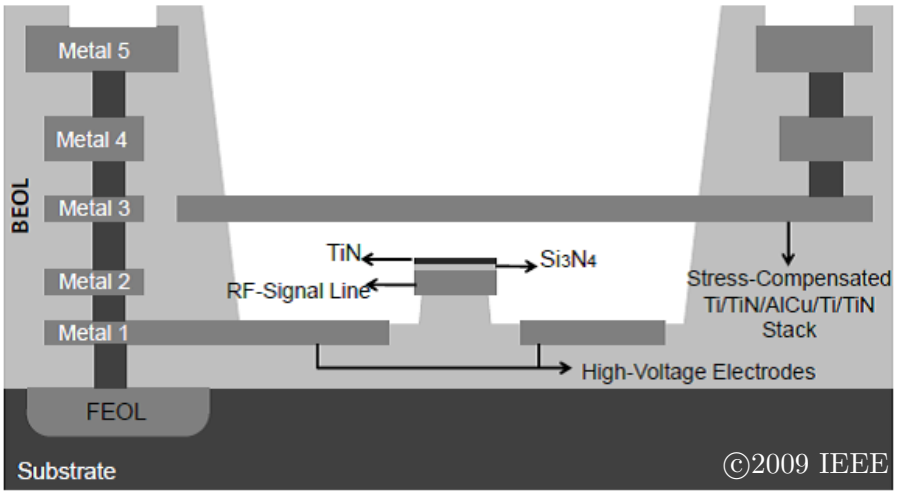

Figure 2.3: Cross section of embedded SG25 RF-MEMS switches [22].

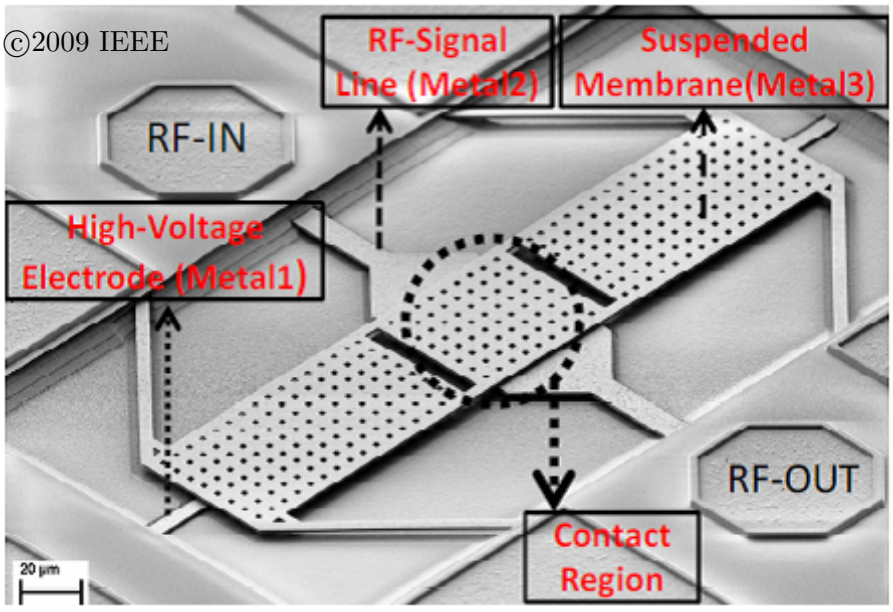

Figure 2.4: SEM image of the SG25 RF-MEMS switch [22].

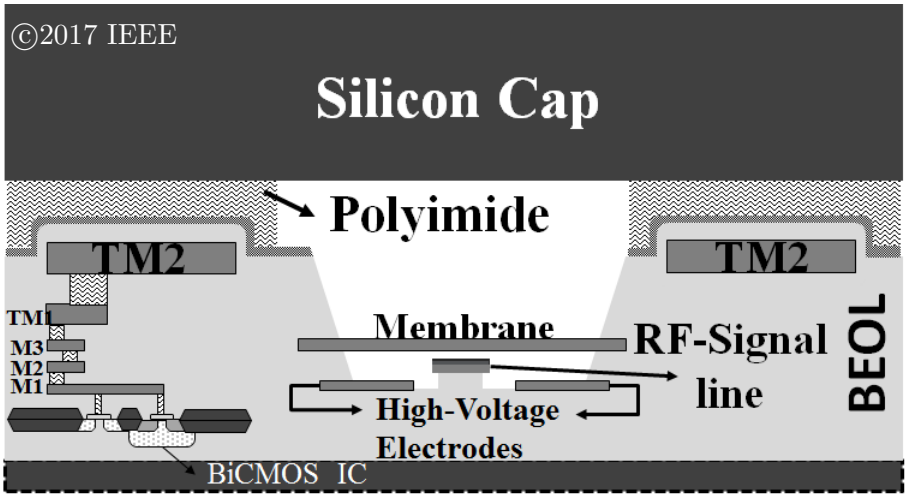

Figure 2.5: The generic cross section of the packaged 0.25 µm SiGe BiCMOS technology RF-MEMS test vehicles [66, 70, 71].

2.2.2 Silicon cap packaging

After the fabrication of the RF-MEMS switches in SG25 BiCMOS, the RF-MEMS cavities are sealed with the Si caps at wafer-level in Fraunhofer IZM, Berlin [69]. The generic view of the packaged 0.25 µm BiCMOS technology RF-MEMS switches is shown in Fig. 2.5. The applied wafer-to-wafer packaging technique is independent from the size of the Si cap; thus the packaging of several RF-MEMS switches can be realized at the same time. The high throughput and flexible size Si caps make it possible to provide BiCMOS embedded RF-MEMS switch technology with a semi-hermetic packaging. The process flow of the Si cap packaging process which is developed and used by Fraunhofer IZM, Berlin is given in Fig. 2.6 [70].

Initially, a glass carrier wafer is bonded to a Si wafer which is coated with an adhesive material. In subsequent process steps, the Si wafer is processed to generate the cap structures. Processes such as back grinding, lithography and Si dry etching are used to form Si cap structures. The structuring of the caps includes the removal of the material in between the particular cap structures by using an additional lithography step and dry etching of the Si. In that case, the adhesive layer acts as an etch stop layer. In the next process steps, the created cap wafer is aligned and bonded to the corresponding 200 mm BiCMOS wafer. The required alignment marks on the cap wafer are created during the cap processing. The caps are structured into a thin Si wafer (50 µm) which is created by back grinding from full thickness (725 µm) after bonding. Each Si cap has an adhesive (polyimide) bonding frame around the rim, with

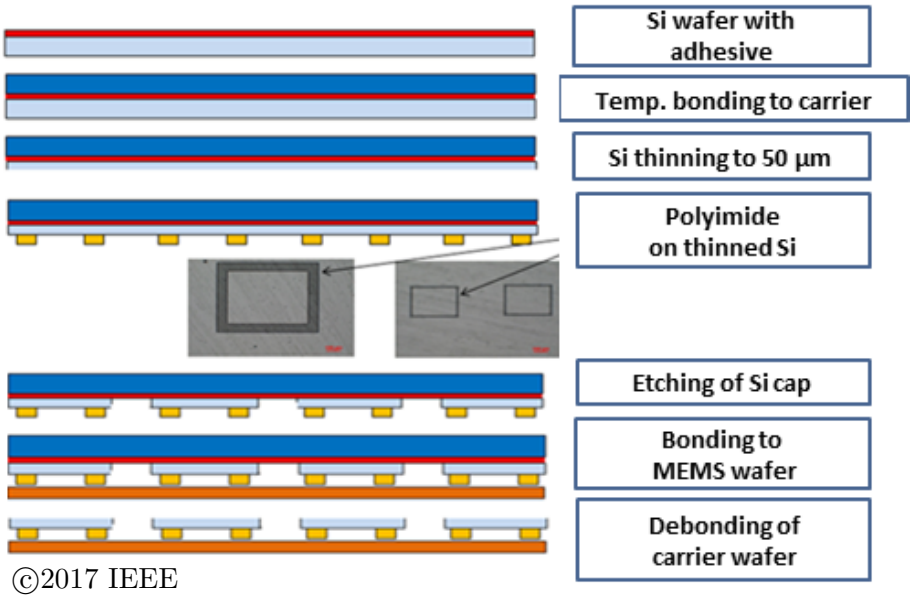

Figure 2.6: The process flow of the wafer-level packaging process for the 0.25 µm SiGe BiCMOS embedded RF-MEMS switch [70].

a height of 5 µm. The bonding frames are structured by lithography and dry etching before the Si caps are structured. The adhesive layer on the carrier wafer around the caps is also removed by dry etching. The Si caps are transferred to the target wafer using a wafer-to-wafer thermo compression bonding process at a temperature of less than 300 °C and with a pressure of 0.1 – 0.2 MPa. After the Si caps are bonded to the BiCMOS wafer, the carrier wafer needs to be removed from the backside of the Si caps. In case the polyimide is only present underneath the caps, a full area laser exposure of the carrier wafer can be performed. The microscope images of the SG25 RF-MEMS switch before and after the wafer-level Si cap packaging are shown in Fig. 2.7.

After the Si cap packaging in Fraunhofer IZM, Berlin; the wafer-level packaged RF-MEMS switches are initially investigated with the FIB analysis in IHP. The FIB analysis shows (Fig. 2.8) the stable polyimide underneath the Si cap even with the TM2 surface topology of the extended RF- SL.

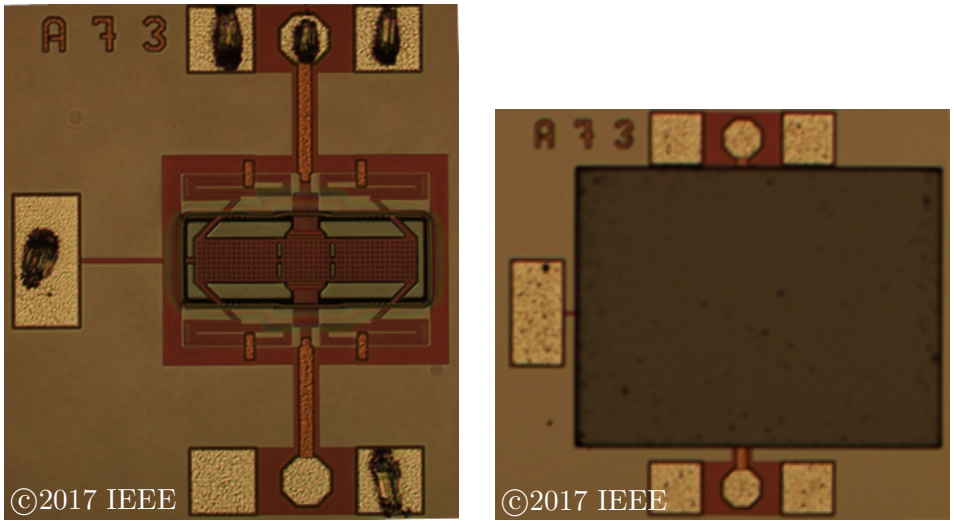

Figure 2.7: The microscope images of RF-MEMS switches (a) before and (b) after wafer-level Si cap packaging [70].

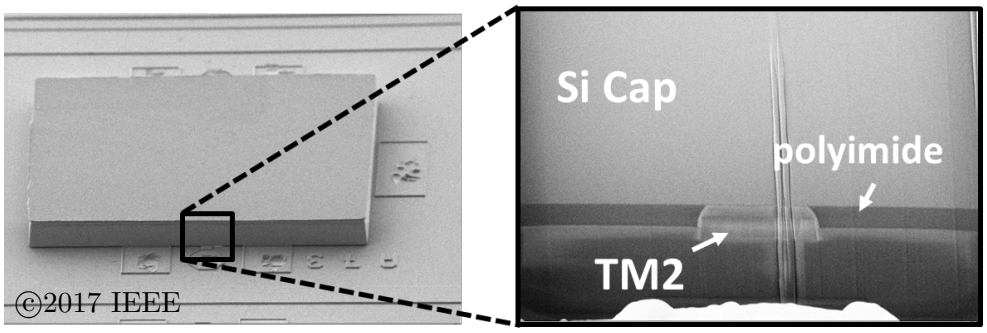

Figure 2.8: The FIB analysis of the Si cap packaged RF-MEMS switch [70].

2.3 Integration of MEMS module in 0.13 µm SiGe BiCMOS Technology

IHP's 0.13 µm node has two BiCMOS technologies; SG13S and SG13G2. SGB13S technology includes two different HBTs with maximum f_{max} of 340 GHz. The highest performance of 0.13 µm IHP technologies is the SG13G2 with the f_{max} values for HBTs up to 500 GHz [24]. The main performance parameters of HBTs for different 0.13 µm technologies [67] are summarized in Table 2.2. In 2016, IHP has demonstrated that SiGe HBTs can go upto f_T/ f_{max} values of 505 GHz/ 720 GHz [13]. With the high performance HBTs and passive elements, IHP's 0.13 µm SiGe BiCMOS technology is a well-fitting technology for the RF and mm-wave applications.

Table 2.2: Main performance parameters of HBTs for different 0.13 µm technologies of IHP [67].

SG13S	npn13p	npn13V
f_{max}	340 GHz	165 GHz
f_T	250 GHz	45 GHz
BV_{CEO}	1.7 V	3.7 V

SG13G2	npn13G2
f_{max}	500 GHz
f_T	300 GHz
BV_{CEO}	1.7 V

The BEOL of the 0.13 µm SiGe BiCMOS offers five thin and two thick AlCu metal layers, and tungsten vias in between. The cross section of the FEOL with the detailed BEOL module is shown in Fig. 2.10. The thin metal layers are named from bottom to top as M1, M2, M3, Metal4 (M4) and Metal5 (M5). The two thick metal layers are TM1 and TM2. Additionally, MIM capacitor is available between M5 and TM1 in order to achieve a high capacitance density of 1.5 fF/µm^2. The passivation on top includes thickness of 1.5 µm SiO_2 and 0.4 µm Si_3N_4.

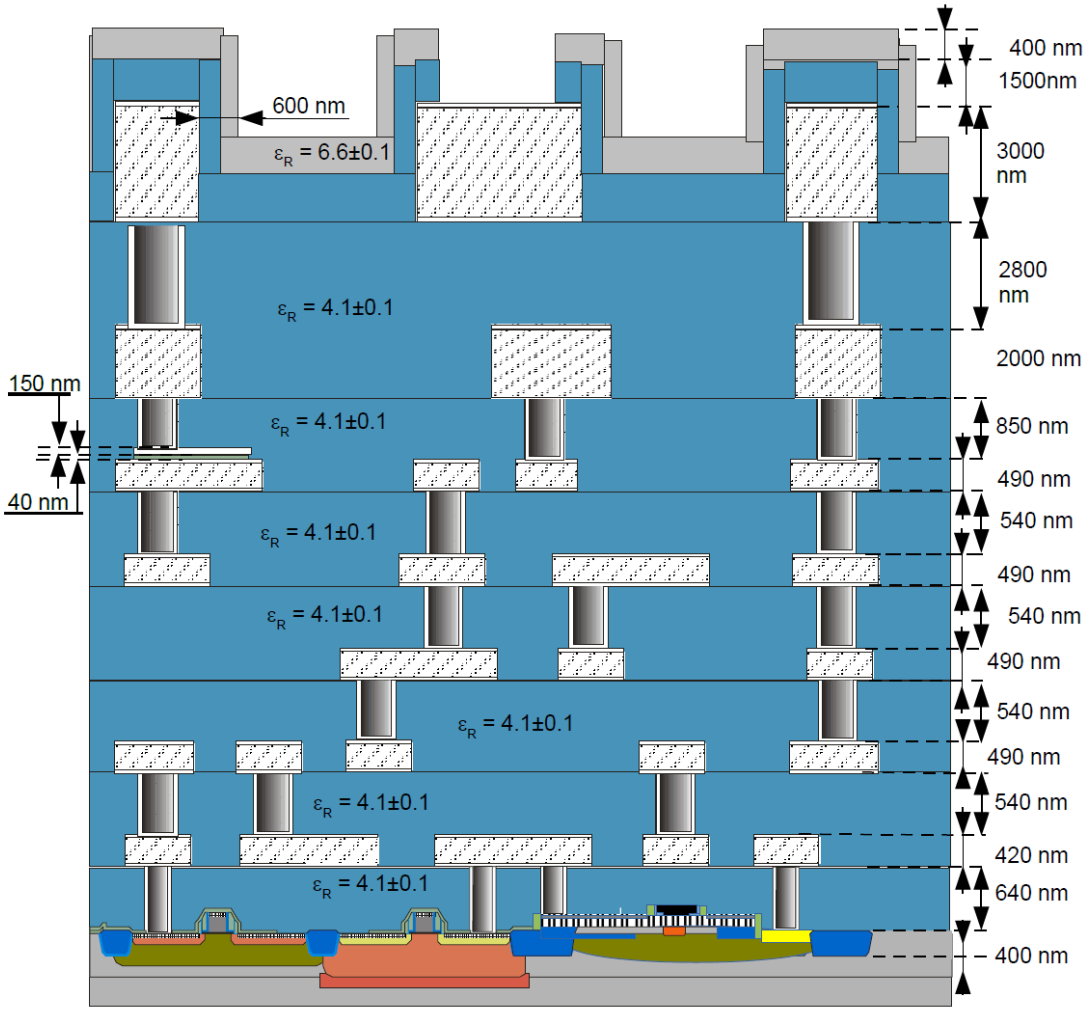

Figure 2.9: The cross section of the SG13S/G2 BEOL [72].

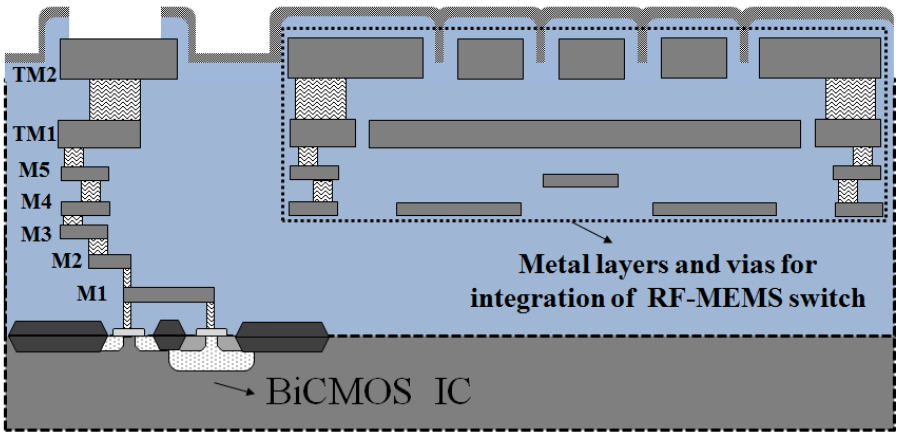

Figure 2.10: The cross section of the SG13 BEOL, including the marked metal layers and vias for the integration of the RF-MEMS switch.

2.3.1 Process integration of MEMS module

BEOL metalization of 0.13 µm BiCMOS technology has seven metal layers instead of five and the distances between the metals are also different compared to 0.25 µm BiCMOS technology. Indeed, it is not possible to easily transfer the 0.25 µm RF-MEMS switch to 0.13 µm BiCMOS technology and some significant effort is necessary in order to develop a switch at targeted bands (D-/J-band). The main changes from 0.25 µm to 0.13 µm technology are the smaller dimensions of the switch to achieve higher frequency of operation, the thicker metal layer of the membrane and the increased distance between the RF- SL to the Si substrate. With the thicker metal layer of the membrane and the reduced size of the switch, mechanical properties like stiffness also changes which results in an increased pull-in voltage. Most importantly, with the increased distance between the RF- SL to the Si substrate, the substrate coupling of the RF-signal to the Si substrate is reduced.

With all the challenges in development of RF-MEMS switch in IHP's 0.13 µm BiCMOS technology, the capacitive RF-MEMS switch is designed between M4 and TM1 of the technology. Similar to the 0.25 µm BiCMOS technology, RF-MEMS switch in 0.13 µm SiGe BiCMOS technology consists of HV electrodes, RF- SL and movable membrane. Fig. 2.10 shows the cross section of the SG13 BEOL, including the RF-MEMS layers that are used during the integration of the RF-MEMS switch.

2.3.2 Wafer-level encapsulation

An huge effort has been spent on RF-MEMS technologies during the last few decades. This effort has brought the RF-MEMS technologies into a point that the first real RF-MEMS products are in the market now. However, it has also been understood that without a good package, an RF-MEMS device cannot be pronounced as a product. It has also been understood that the RF-MEMS device and package development cannot be considered as different processes to find the most optimum solution. This means, the packaging solutions need to be considered and decided during the RF-MEMS device development, not afterwards. In the wafer bonding approaches for the wafer-level packaging (WLP), the cost of at least one lid wafer is added to the total production cost [73]. These additional lid wafers can also add more process steps like wafer grinding or chemical mechanical polishing (CMP). The wafer bonding approach does not only increase the cost but also requires additional area around the MEMS devices to accommodate the cap. Indeed, wafer-level encapsulation [74–76] has advantages over the WLP with wafer bonding approach in terms of cost and area. Predictably, the wafer-level encapsulation approach is also the chosen method for the well-known commercial packaged MEMS devices [60, 77, 78]. Therefore, as part of the integration of the RF-MEMS switch into IHP's 0.13 µm SiGe BiCMOS technology; thin film wafer-level encapsulation is developed [79, 80].

Fig. 2.11 shows the process flow schemes of the embedded RF-MEMS switch in 0.13 µm SiGe BiCMOS technology. The developed switch consists of two M4 HV electrodes, a M5 RF- SL, a TM1 movable membrane, and a TM2 plate with releasing holes. The TM2 plate is placed on top of the switch for the wafer-level encapsulation. Integration of the RF-MEMS switch includes supplementary process developments additional to the standard BEOL flow of the passives which mainly includes lateral and vertical etch stops and the planarized oxide on the TM2 plate. Initially, TM2 layer of the RF and DC pads are reached with the passivation opening (Fig. 2.11 (a)). Afterwards, with an additional mask, the RF-MEMS switches are released through the TM2 plate holes until the M4 HV electrodes by hydrofluoric acid vapor phase etching (HFVPE) (Fig. 2.11 (b)). Fig. 2.12 shows the scanning electron microscopy (SEM) image of the released RF-MEMS switch before the wafer-level encapsulation. The releasing steps are then followed by the 4 µm thick high deposition rate (HDR) oxide deposition on the TM2 plate to fill the holes and have encapsulated switch. Finally, the HDR oxide covered pads are reopened by RIE to provide electrical connections for the measurements (Fig. 2.11 (c)). Fig. 2.13 demonstrates the additional process steps for the integration of RF-MEMS switches into the SG13 BiCMOS technology.

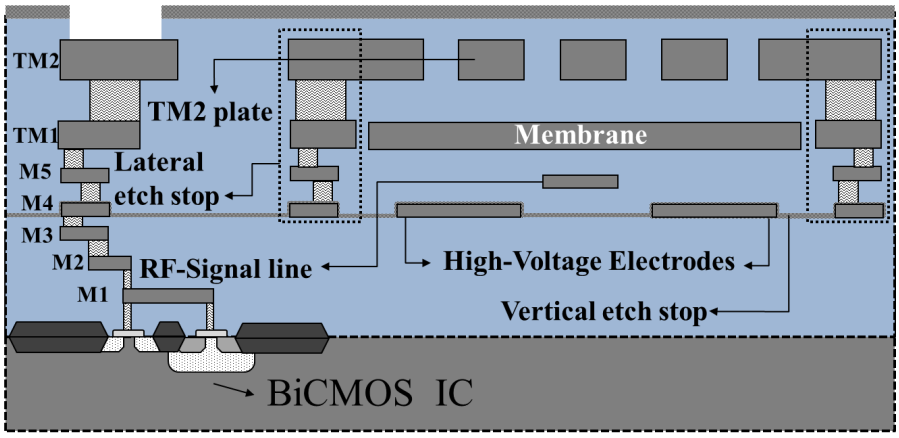

(a)

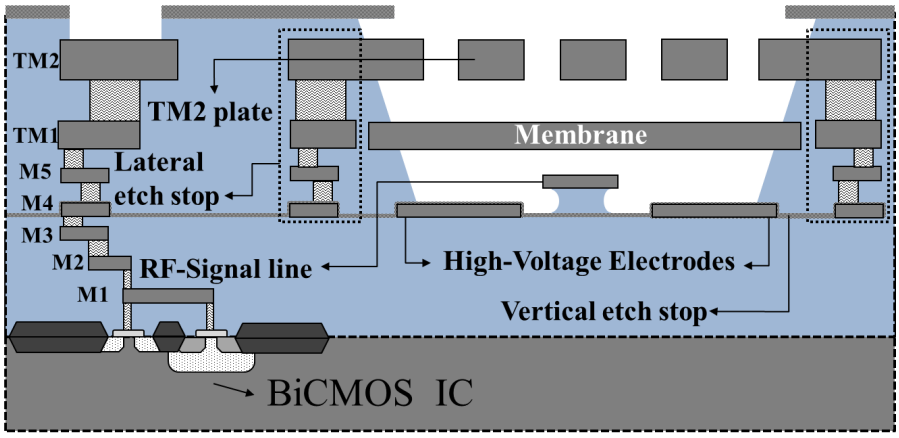

(b)

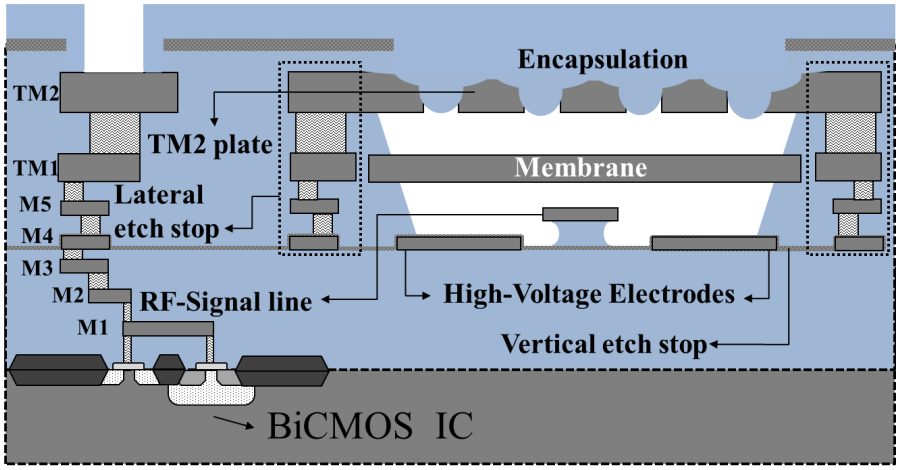

(c)

Figure 2.11: The process flow of the RF-MEMS switch in schematics.

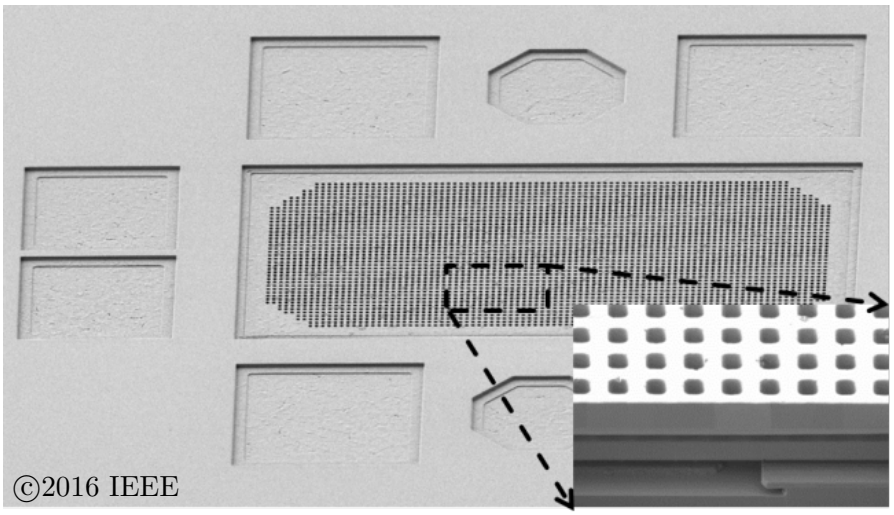

Figure 2.12: The SEM image of the released RF-MEMS switch before the wafer-level encapsulation (including the FIB cross section) [79, 80].

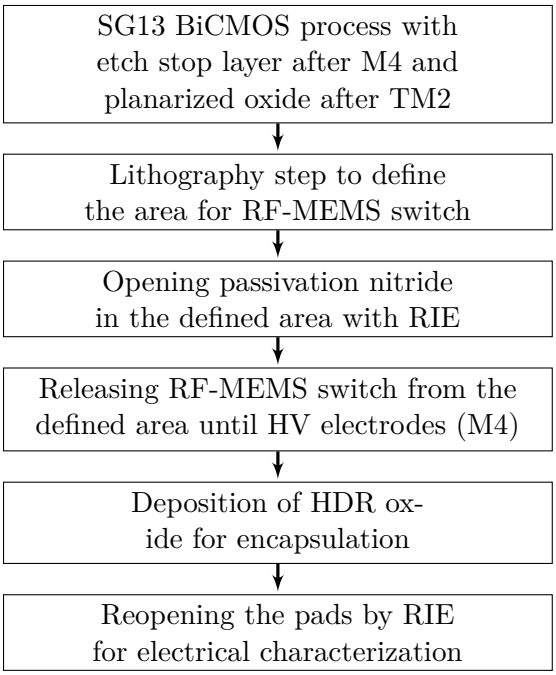

Figure 2.13: Additional process steps for RF-MEMS switch integration into the SG13 BiCMOS process.

For the success of the wafer-level encapsulation, different design modifications are done and process parameters are optimized. In detail, the TM2 plate's hole size was one of the most important design parameter for both the HF vapor phase etching and the wafer-level encapsulation. For the investigation of the hole size impact, the quadratic hole sizes are varied with the side length (a) of 1.25 µm, 1.5 µm, 1.75 µm and 2.0 µm. Considering a TM2 thickness of d= 3 µm results in aspect ratios (ARs) (AR = d/a) from 2.4 down to 1.5.

Beside the hole size, the plasma enhanced chemical vapor deposition (PECVD) process for the HDR oxide deposition is optimized to achieve the required low step coverage. By minimizing the process temperature of the HDR oxide deposition it is also intended to reduce its influence on the active elements of the FEOL and on the mechanical behavior of the RF-MEMS switch. Consequently, a maximum temperature of 200°C for HDR oxide deposition has been developed to achieve closing of the TM2 plate holes.

As a result of the variable TM2 plate hole size investigation, successfully encapsulated RF-MEMS switches are achieved with an AR of 2.4 and 2.0 (Fig. 2.14 (a) and (b)). With an AR of 1.7, a carbon containing material inside the closing holes is determined by energy dispersive X-ray (EDX) spectroscopy which is coming from the spin-coating of the photoresist mask before the RIE opening of the pads (Fig. 2.14 (c)). The photoresist can only enter from the TM2 plate holes in case of a not fully closed TM2 plate holes. Clearly with an AR of 1.5, a fully closed encapsulation also could not be achieved (Fig. 2.14 (d)). Indeed, with AR of 2.4 and 2.0 it became possible to close the TM2 plate holes and prevent the unwanted HDR oxide deposition through the holes into the cavity.

Fig. 2.15 shows the SEM image of the fabricated WLE RF-MEMS switch with its marked region for the FIB cut. FIB analysis shows that RF-MEMS switch is released and encapsulated successfully. The FIB cross section of the WLE RF-MEMS switch is given in Fig. 2.16 and it shows the covered TM2 plate with the HDR oxide, the released TM1 membrane, the M4 HV electrode and the M5 RF- SL in detail.

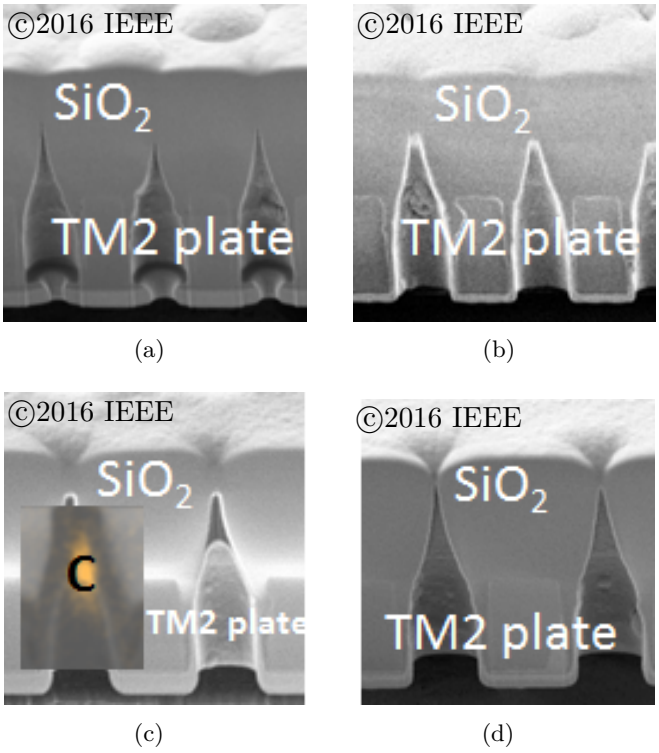

Figure 2.14: The focused ion beam SEM images of the wafer-level encapsulation with varied aspect ratios (a) AR= 2.4, (b) AR= 2.0, (c) AR = 1.7 (with a carbon containing material inside the closing holes which is determined by EDX spectroscopy) and (d) AR= 1.5 [79, 80].

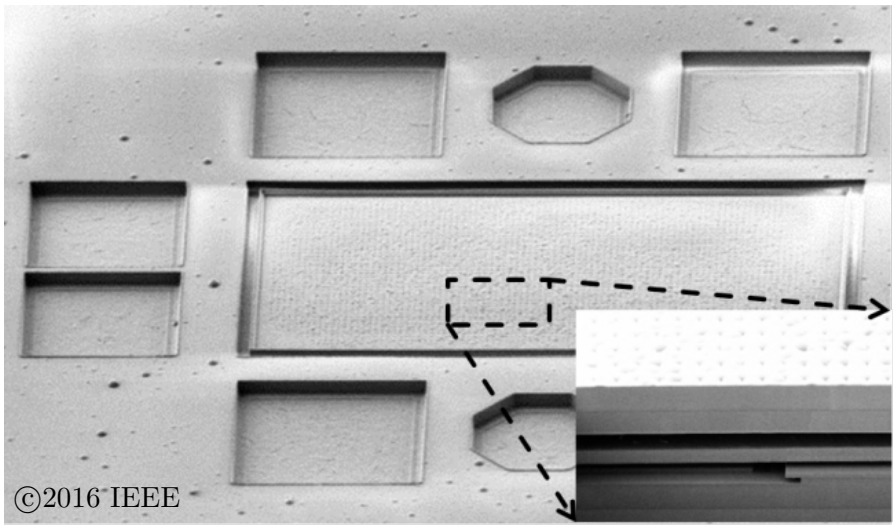

Figure 2.15: The SEM image of the WLE RF-MEMS switch (including the FIB cross section) [66, 79, 80].

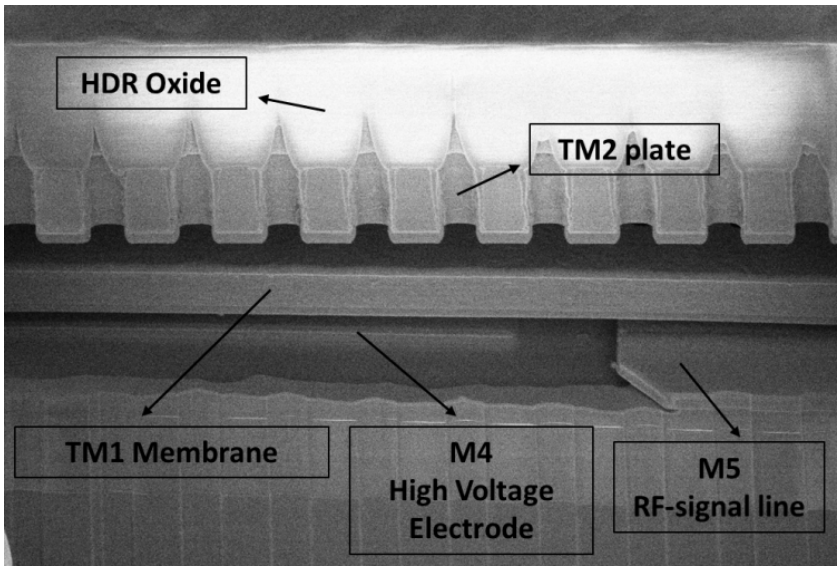

Figure 2.16: The FIB cross section of the WLE RF-MEMS switch, showing the HDR oxide deposited TM2 plate, TM1 membrane, M5 RF-Signal line contact region and one M4 electrode.

2.4 Conclusion

In Chapter 2, the process integration of MEMS modules in 0.25 µm and 0.13 µm SiGe BiCMOS technologies have been presented. Within both technology sections, additional process steps for the MEMS module have been detailed. MEMS modules of 0.25 µm and 0.13 µm SiGe BiCMOS technologies have presented two different packaging approaches (including their process flows); namely wafer-to-wafer bonding Si cap packaging and thin film wafer-level encapsulation. Wafer-to-wafer bonding Si cap packaging technique as presented in Section 2.2 can be used in niche markets for low-volume production. On the other hand, the thin-film wafer-level encapsulation technique that has been presented in Section 2.3 has more advantages in terms of smaller area and has already proven to be used in mass production for mobile applications [48, 58].

3 Modeling of RF-MEMS Switches

3.1 Introduction

Chapter 3 presents two different RF-MEMS switches, that are embedded into IHP's 0.13 µm SiGe BiCMOS process technology. The first switch is developed and optimized for D-band applications and the second switch is developed and optimized for J-band applications. The chapter includes electromagnetic modeling, lumped-element modeling and the experimental results of both switches. The simulation domain in this thesis is the electromagnetic domain where a 3D EM solver is preferred to 2.5D planar EM solvers to develop and optimize the RF-MEMS switches.

To realize an RF-MEMS switch in mm-wave operating frequencies, the first milestone is developing an accurate EM model. In the development of the accurate EM model, selection of the EM solver plays an important role. Between different EM solvers, the 2.5D planar EM solvers are the mostly preferred ones where modeling of passive devices is very convenient and straightforward. However, most of the 2.5D planar EM solvers have the limitation of defining non-uniform dielectric planes in horizontal direction. Nevertheless, this is in contrast with the MEMS devices since the mechanical parts of the MEMS devices are mostly in air but the anchors and routing layers are in a dielectric. To be able to avoid this problem, a modeling solution with 2.5D planar EM solver is demonstrated in [65, 81] for frequencies up to 110 GHz. The authors present accurate simulation results by implementing the measured contact parameters of the RF-MEMS switch as lumped elements with a defined port in the contact region. However, the presented solution do not guarantee the accuracy for the modeling of RF-MEMS switches at above 110 GHz frequencies. Shortly, a more careful modeling strategy is essential for EM simulation of RF-MEMS devices at high frequencies.

In this thesis, accurate 3D EM models for BiCMOS embedded RF-MEMS switches in both 0.25 µm and 0.13 µm technologies are built up in ANSYS HFSS 3D finite-element-method (FEM) solver. The 3D EM solver allows defining the air cavity of the switch and the BEOL oxide simultaneously in the same model, in contrast to 2.5D planar EM solvers. Using the developed model, RF behavior of the MEMS device in

air and the routing layers in oxide can be simulated at the same time which is very important considering the very high operating frequency. Furthermore, the process effects such as bending of the membrane can also be modeled by changing the initial gap in the simulator. The advantages of the 3D EM solver are explained in detail in Section 3.2.1.

After the development of the RF-MEMS switches, the fabricated switches are optically and electrically characterized. For the dynamic behavior of the D-band switch, laser-doppler-vibrometer (LDV) technique is used. For the electrical characterizations of both switches in this chapter, Capacitance-Voltage (C-V) and S-parameter measurements are performed.

3.2 D-band RF-MEMS SPST Switch

Section 3.2.1 begins with the challenges of modeling RF-MEMS switches at mm-wave and the special methods that has been used for accurate EM simulations. EM modeling of the RF-MEMS switch for D-band applications in SG13 BiCMOS technology starts with usage of an inductive loaded design, similar to the SG25 switches. With the wafer-level encapsulation approach in packaging, the design of the inductive loaded switch is changed by removing the inductive loads which are in BEOL oxide and increasing the length of the membrane arms which are in air. Later on, the updated switch design is used in EM models for the optimizations of its important parameters; such as the effect of the TM2 encapsulation plate, the arm width of the membrane, the contact region, the RF- SL width, the membrane hole density and the ground-ring width. Additional to the EM model, a lumped-element model is created (see Section 3.2.2) which represents the behavior of the switch based on RLC elements and can be used in circuits on system-level. Lastly in Section 3.2.3, the RF optimized WLE RF-MEMS switch for D-band applications is characterized by LDV, C-V and S-parameter measurements.

3.2.1 Electromagnetic modeling

The EM simulations of the RF-MEMS devices are commonly performed by the 2.5D planar or 3D FEM solvers with the well-known material properties such as conductivity and dielectric constant. Nevertheless, there are some common limitations of the EM simulators for simulating MEMS devices. Typically, it is not possible to include the bended structure of the suspended layers or the surface roughnesses of the materials.

Therefore, a careful design methodology is necessary to model the RF-MEMS devices specifically for mm-wave applications.

3D vs 2.5D EM case comparisons

The main limitation of the 2.5D planar EM solvers is that all the layers are defined infinite in horizontal directions. Since all the layers are defined infinite in horizontal plane, the RF-devices cannot be simulated with released parts in air cavity and other parts buried in dielectric. For this reason, the RF-MEMS switch can only be simulated with all the anchors and routings in complete air or in complete another dielectric environment. Such a case might have less influence on the results of the EM simulations considering the operating frequencies less than 40 GHz. However, at frequencies especially above 110 GHz, the anchors and the routing layers of the switch which are normally in the BEOL oxide has a significant effect on the overall performance of the RF-MEMS switch, considering the low resistive silicon substrate (50 Ω·cm) below the RF-MEMS switch.

In order to compare the RF performance of the switch in two different environment conditions, RF simulations of the switch are performed as if all parts of the switch, including the parts located in back-end-of-line (BEOL) oxide, are in air. Fig. 3.1 shows the created EM setups for the comparison of 2.5D planar EM solver and 3D EM solver cases. The comparison of the RF performances of the switch for two different environment conditions is shown in Fig. 3.2. The bold red and blue curves show the RF performance of the switch when it‘s all in air and RF performance of the switch when the anchors and the routing layers of the RF-MEMS switch are in the BEOL oxide, respectively. As two environment conditions are compared in EM simulations, in the off-state (up-state) RF-MEMS switches at high frequencies have quite different S_{21} and S_{11} curves when in the on-state (down-state) they have quite similar isolations. In both environment conditions contact region is simulated in air. Similar RF performances in down-state is due to the domination of the on-state contact capacitance, C_{on}, when compared with the other parts of the switch. Different RF behaviors in up-states are because of the domination of the anchors and routings of the switches, as compared to C_{off}, that are simulated in oxide or in air. Comparison of the RF performance of the switches shows that at high frequencies depending on the simulation environment different results in up-state can be obtained. Indeed, an accurate EM model for D-band RF-MEMS switch needs to consider the anchors and the routing layers in BEOL oxide. Therefore, it is mandatory to simulate the mm-wave RF-MEMS devices in 3D EM solvers.

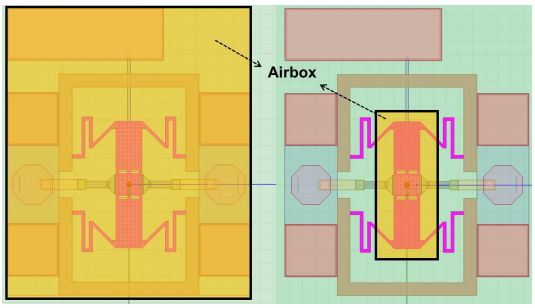

Figure 3.1: Comparison of 2.5D planar EM solver (left) and 3D EM solver cases (right).

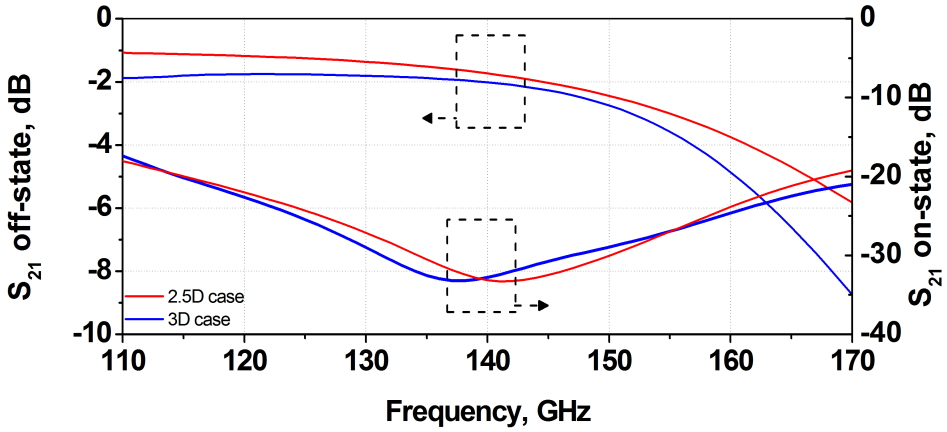

(a)

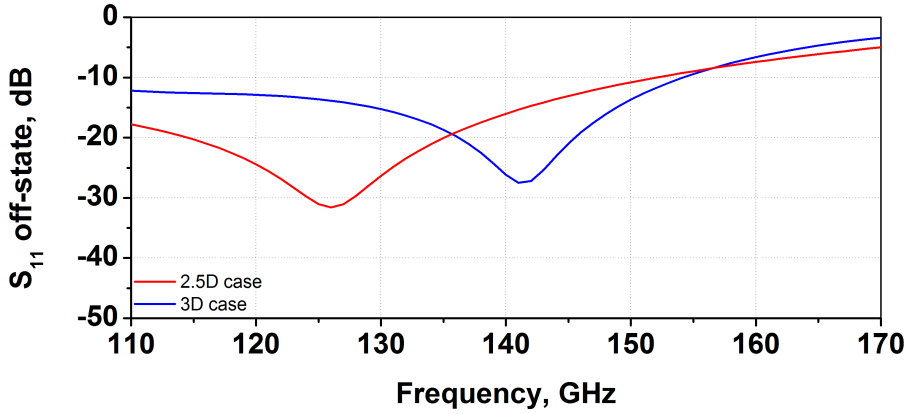

(b)

Figure 3.2: Comparison of the RF performances of the switch for two different environment conditions (2.5D case and 3D case): (a) S_{21} off-state and S_{21} on-state, (b) S_{11} off-state.

Initial approach for the switch

Although the intrinsic part of the RF-MEMS switch can be simulated in air and the rest in oxide with the 3D EM simulations, there is another limitation coming with process variations during fabrication. The contact capacitance of the switch can vary with the membrane bending in both up and down states and also with surface roughness in down state. For an accurate switch model in a 3D FEM solver, the contact air capacitances of the switch in both states needs to be known. Therefore, the contact air capacitances for off (up) and on (down) states, C_{off} and C_{on}, should be extracted from measured C-V data and the appropriate membrane positions should be given into the EM model with respect to the extracted values for each state. The mentioned above contact air capacitances are the capacitances between the membrane and the RF- SL for each states of the RF-MEMS switch. The 3D EM simulation setup, that is created during the development of the D-band BiCMOS embedded RF-MEMS switch considers the air cavity inside the BEOL oxide and is shown in Fig. 3.3. Fig. 3.4 shows the contact region of an RF-MEMS switch in its initial EM model including the inductive loading.

EM simulation results of the inductive loaded RF-MEMS switch for different contact air capacitances that change with different distances in the contact region are shown in Fig. 3.5. Each graph includes S-parameter results with the change of the membrane distance by 50 nm steps over 710 nm initial distance. The bold red and blue curves show the expected up and down state results, respectively. As it can be seen, the electrical resonant frequency of the switch is decreasing with the reduced distance between membrane and MIM layer of the RF- SL. With respect to the EM simulation, IL less than 2 dB and isolation (ISO) higher than 32 dB can be achieved, including the RF measurement pads at 140 GHz. The return loss for up-state is higher than 25 dB at 140 GHz.

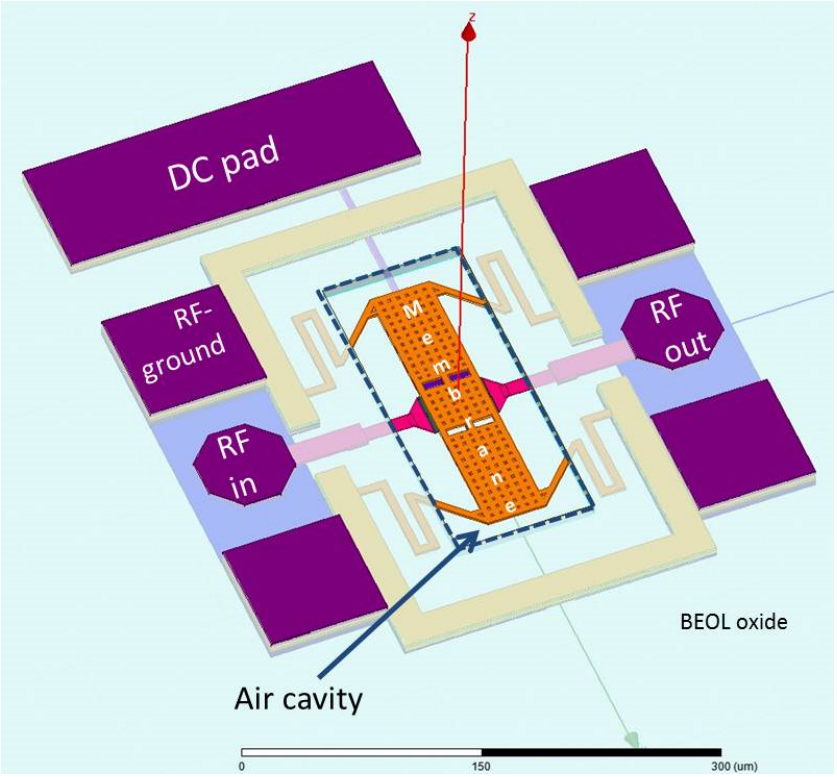

Figure 3.3: Simulation setup in ANSYS HFSS for the initial 140 GHz BiCMOS embedded RF-MEMS switch [82].

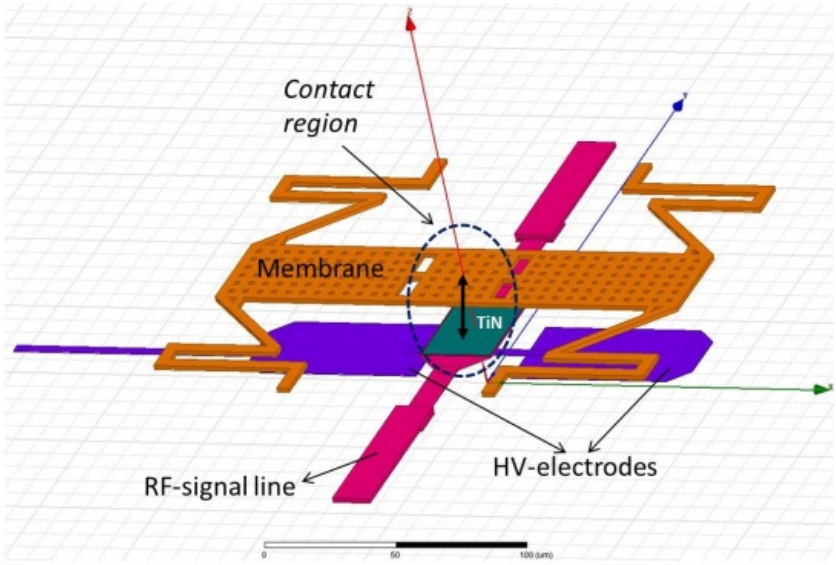

Figure 3.4: Contact region of the initial RF-MEMS switch [82].

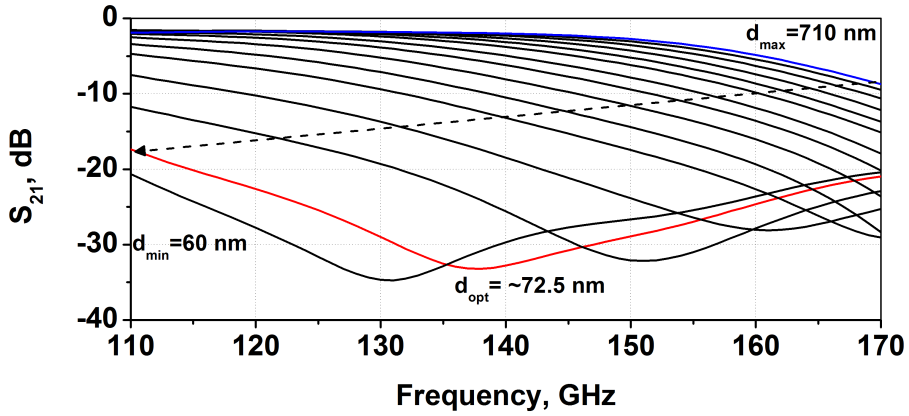

(a)

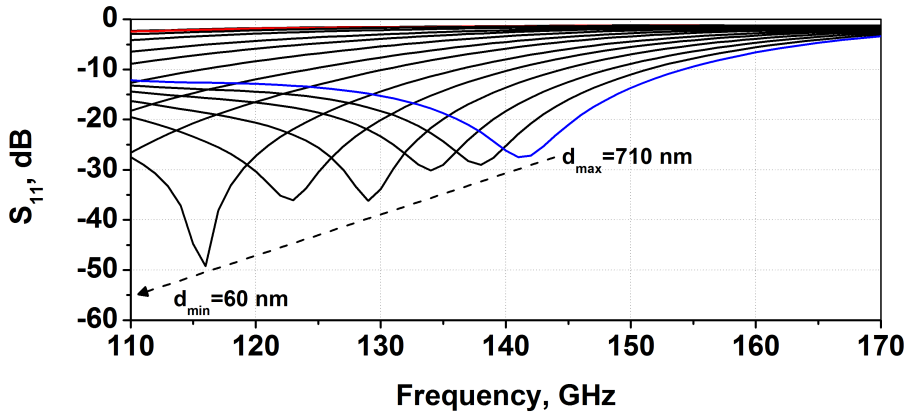

(b)

Figure 3.5: Simulated RF performance of the initial RF-MEMS switch for different contact region distances with the change of 50 nm in each step: (a) S_{21}, (b) S_{11} [82].

New approach in packaging and new switch design

During the initial EM modeling of the D-band switch, packaging possibilities for the device is considered. Two different packaging approaches have already been demonstrated with the SG25 RF-MEMS switches in [83] and [69]. With a new packaging approach, geometrical modifications were necessary on the initial model of the D-band RF-MEMS switch. The new design for D-band RF-MEMS switch is shown in Fig. 3.6 (a) and does no more include the extra inductive loading between the arms and the RF ground-ring.

For an accurate EM model in the 3D FEM solver, the distances between TM1 membrane and M5 RF-SL for both off (d_{off}) and on-states (d_{on}) of the switch are needed to be inserted into the simulator. The mean value of the distance between the TM1 and M5 layers is 900 nm in IHP's 0.13 µm SiGe BiCMOS technology. In order to estimate the possible RF performance differences due to the process variations, parametric EM simulations with different d_{off} and d_{on} are performed (Fig. 3.6 (b, c)). For the insertion loss in the parametric EM simulation the membrane position is swept from 100 nm above the specified TM1 layer until 100 nm below with a step size of 50 nm. The maximum and minimum d_{off} vary the calculated contact air capacitance between 10.6 fF and 13.2 fF. Fig. 3.7 (a) shows the change of the insertion loss curves with different d_{off} values. Varying d_{off} by 200 nm leaded to 0.16 dB change of insertion loss at 170 GHz. Furthermore, the parametric EM simulations are extended with different d_{on} values for the isolation curves. The distance d_{on} is stepwise (10 nm) decreased starting from 100 nm down to 40 nm and the simulation results are shown in Fig. 3.7 (b). The maximum and minimum d_{on} vary the calculated contact air capacitance between 106.24 fF and 265.62 fF.

Decreasing d_{on} by 60 nm caused a resonant frequency shift from the lower end of the D-band to the upper end. Briefly, the varying d_{off} due to process variations did not affect the insertion loss tremendously but the resonant frequency shifted significantly with the varying d_{on}. For this reason, the contact air capacitances are extracted from the C-V measurements of the RF-MEMS switch to have an accurate 3D FEM result of the D-band RF-MEMS switch especially for the on-state. Based on the extracted contact air capacitances (C_{off} and C_{on}) and the known contact area of the switch (A_{cont}), d_{off} and d_{on} can be calculated using the simple parallel plate capacitor equation (equation 3.1) and inserted into the EM model. In equation 3.1, $C_{parallelplate}$ is the capacitance in farads which is constructed by two parallel plates of area, A, in square meters and separated by a distance, d, in meters. ε_r is the relative permittivity of the

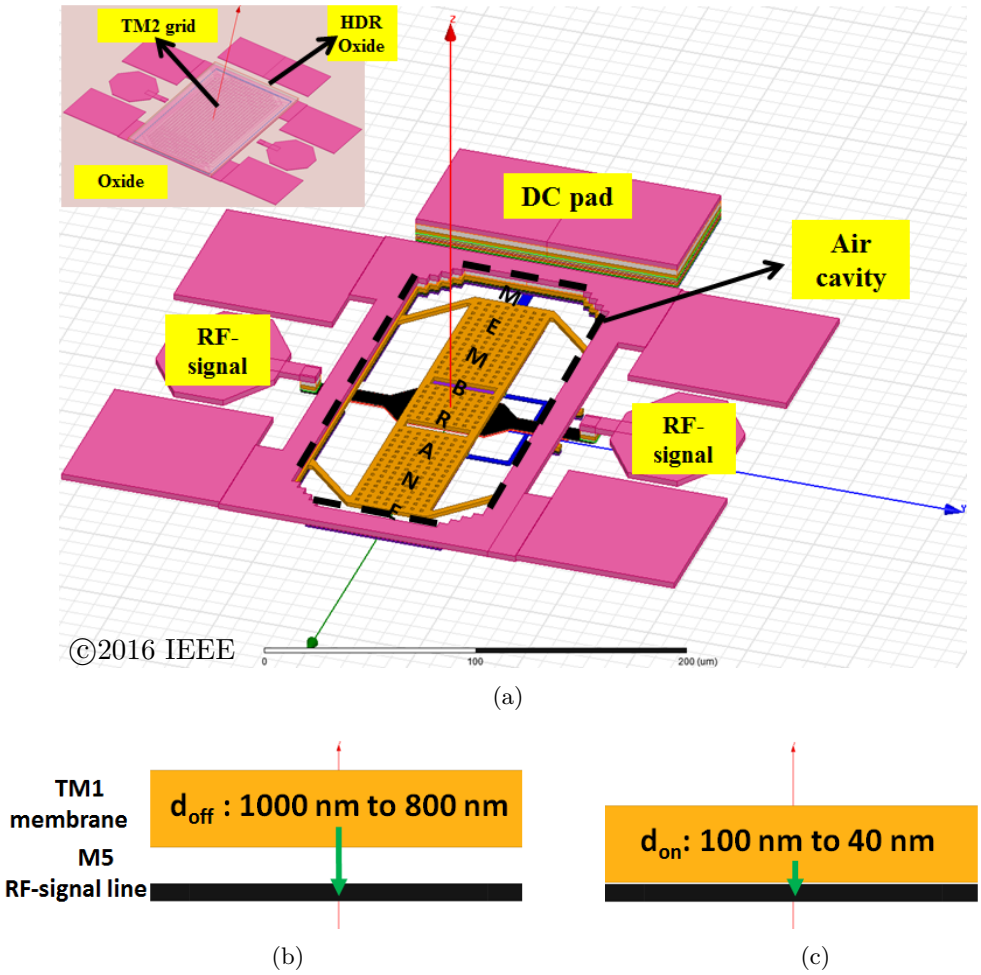

Figure 3.6: EM Simulation model in ANSYS HFSS for D-band BiCMOS embedded WLE RF-MEMS switch (a) with the schematic diagram for the parametric EM simulations (b) for different d_{off} and (c) d_{on} values [79, 80].

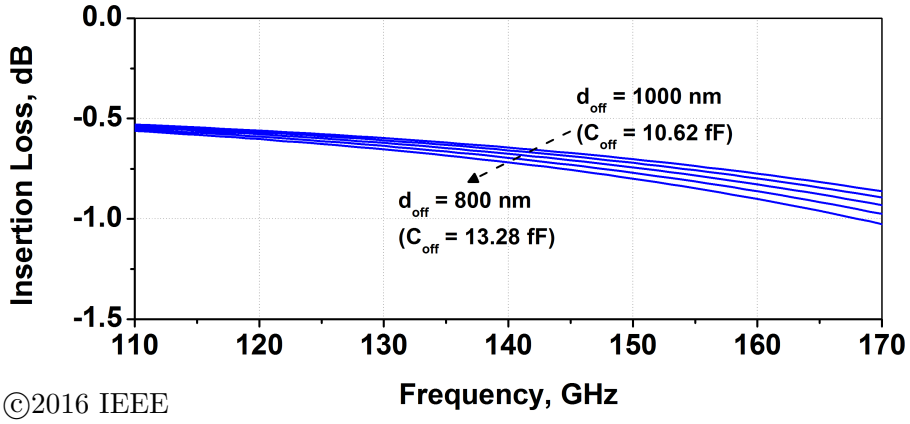

(a)

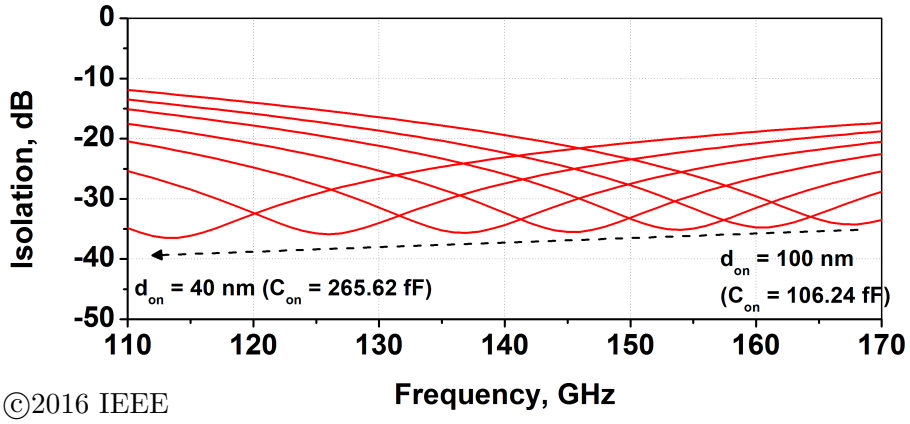

(b)

Figure 3.7: The simulated S-parameters of the WLE RF-MEMS switch with varying TM1 membrane and M5 RF-SL distances due to process variation: (a) insertion loss, (b) isolation [79, 80].

material between the plates and ε_0 is the permittivity of free space, $8.854{\cdot}10^{-12}$ F/m.

$$C_{\text{parallel plate}} = \varepsilon_{\text{r}} \cdot \varepsilon_0 \cdot \frac{A}{d} \tag{3.1}$$

For the EM modeling and optimization, the important parameters of the 140 GHz targeted encapsulated RF-MEMS switch are determined as the effect of the TM2 encapsulation plate, the arm width of the released membrane, the contact region, the RF-SL width, the membrane hole density and the ground-ring width, as given in Fig. 3.8. In the following subsections, the aforementioned critical parameters of the RF-MEMS switch are modeled and optimized in D-band.

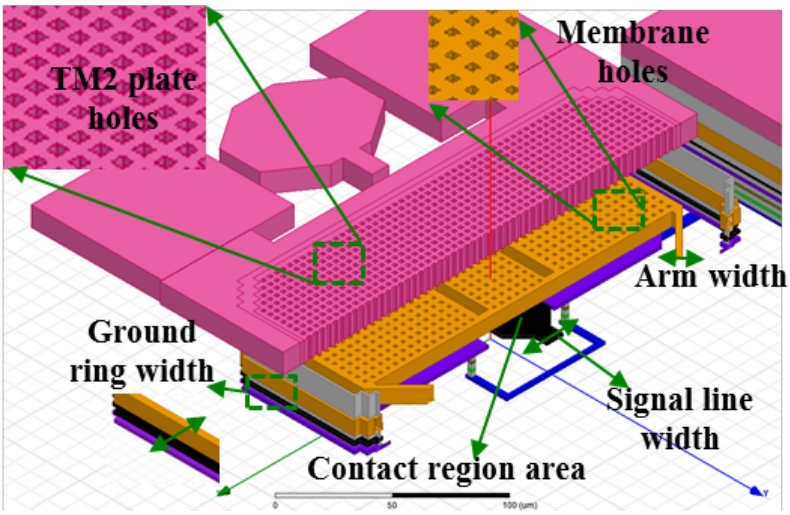

(a)

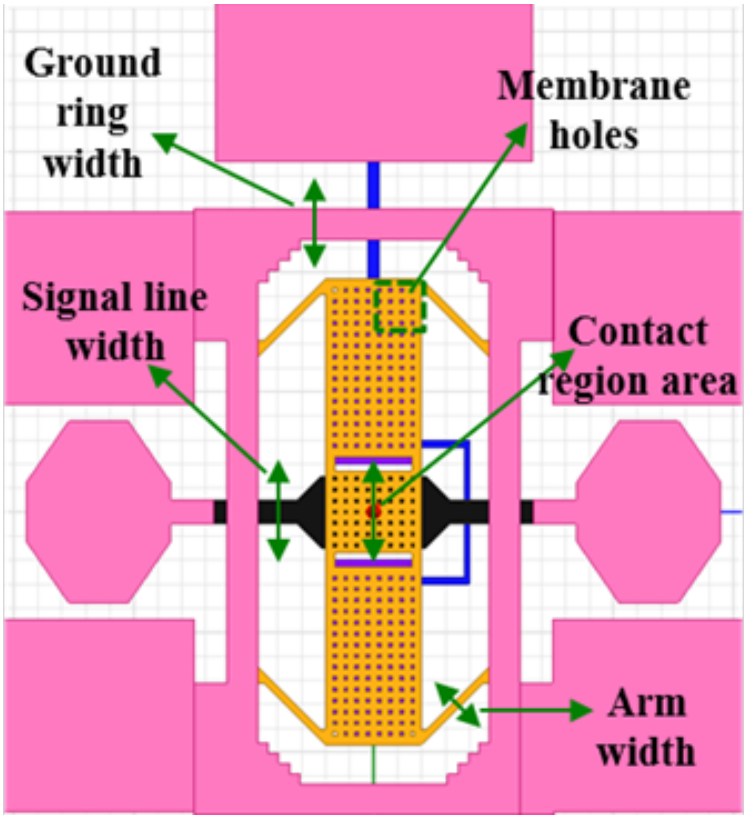

(b)

Figure 3.8: The modeled RF–MEMS switch with its key EM optimization parameters; (a) isometric view with clip plane (b) top view with hidden TM2 plate.

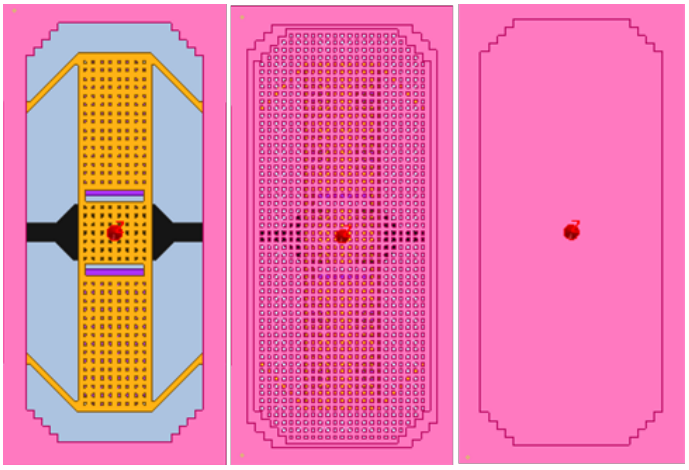

Figure 3.9: Three different EM simulations in order to investigate the effect of the TM2 plate (a) without TM2 plate (b) with TM2 plate, including the releasing holes (c) with TM2 plate, without the releasing holes.

Effect of the TM2 plate

It is crucial to consider the influence of the package from the beginning of the RF-MEMS device development since its influence on the device performance cannot be avoided. Therefore, the RF optimization of the D-band RF-MEMS switch is started with a focus on the TM2 encapsulation plate to investigate the influence of the package.

The initial step to see the effect of the package is in the definition of the EM model. Since the TM2 plate includes many small holes which significantly increases the simulation time, three different EM models are created for the preliminary comparison: the RF-MEMS switch without a TM2 encapsulation plate (Fig. 3.9 (a)), with a TM2 encapsulation plate including small holes (Fig. 3.9 (b)) and with a TM2 encapsulation plate without holes (Fig. 3.9 (c)). The EM simulation comparison (Fig. 3.10) has shown significant differences in S-parameter results if an encapsulation plate is introduced. With the TM2 plate, the off-state performance of the RF-MEMS switch has shown an increased loss in all D-band and the resonant frequency of the on-state has shifted from 153 GHz to 140 GHz. However, the comparison of two models, including the TM2 plates with and without the releasing holes has shown that there is no significant difference in terms of RF performance between the two models. By omitting the TM2 releasing holes, the number of meshed elements and the total simulation time are reduced by half. As a result of this, all the further simulations of this work are done including the TM2 plates but without the releasing holes.

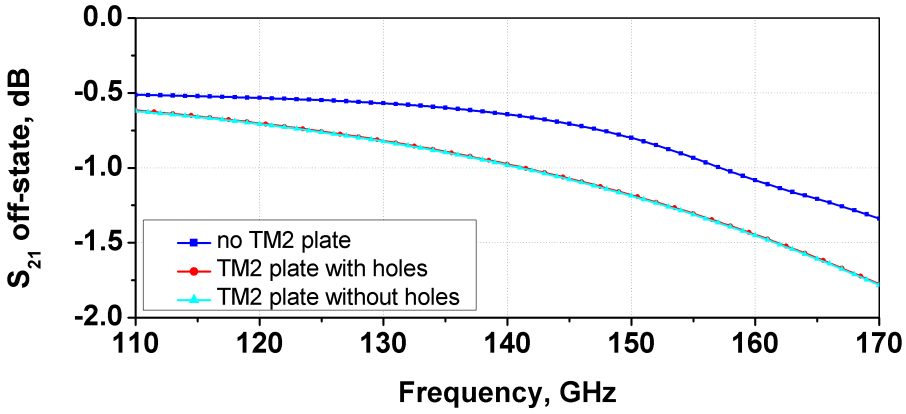

(a)

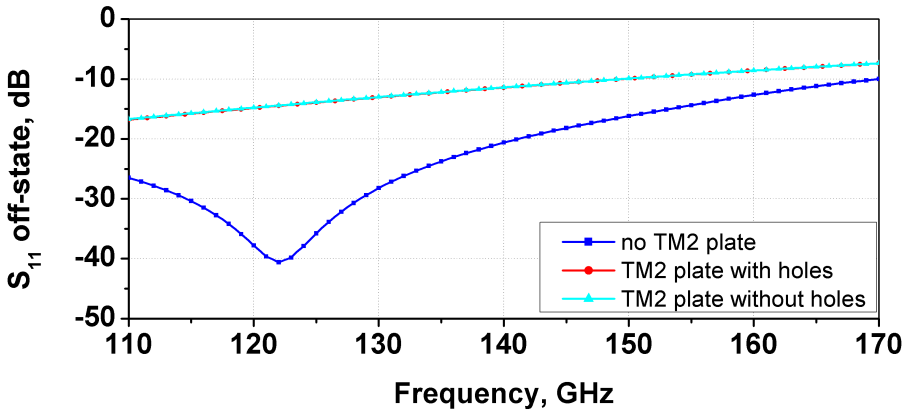

(b)

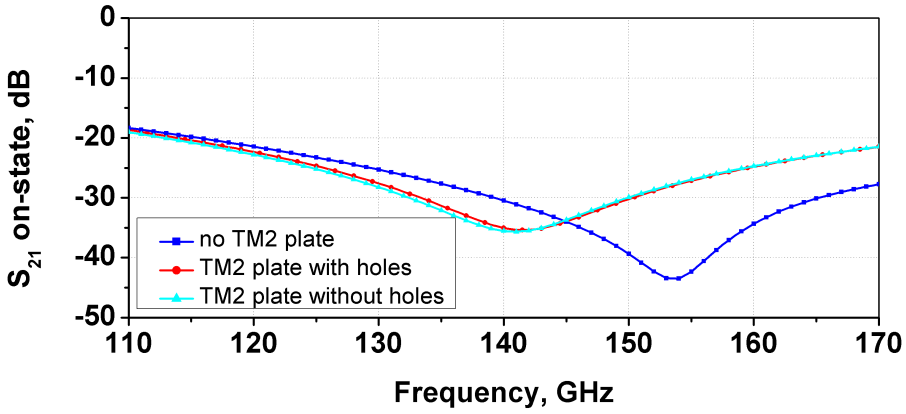

(c)

Figure 3.10: The S-parameter simulation comparison of the RF-MEMS switches for the TM2 plate investigation, (a) S_{21} off-state (b) S_{11} off-state and (c) S_{21} on-state.

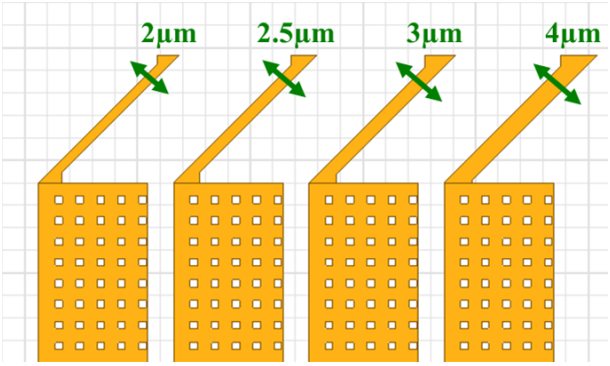

Figure 3.11: The generic view of the varied arm width of the RF-MEMS switches.

Optimization of the arms

After simplification of the EM model by removing the TM2 plate holes, EM simulations are continued with an investigation on the varied arm width of the RF-MEMS switch to show the effect of the arm inductance (L_{arm}) on the RF performance. It is worth to mention that the limits of the process lithography and mechanical constraints are considered during the optimization of the arms for maximizing the RF performance.

By tuning the contact air capacitance or the arm inductance of the RF-MEMS capacitive switches, operation at different frequency bands can be achieved [83]. The main series resonant frequency in on-state is calculated, as follows:

$$f = \frac{1}{2\pi \cdot \sqrt{C_{cont} \cdot L_{total}}} \tag{3.2}$$

In equation 3.2, C_{cont} is the contact air capacitance and L_{arm} is the total inductance coming from the membrane, arms and the ground-ring of the RF-MEMS switch where arms have the most significant contribution. Fig. 3.11 shows the generic view of the varied RF-MEMS arm width between 2 µm to 4 µm. It should be noted that the d_{off} and d_{on} are kept identical during the simulations with different arm widths.

The off-state S_{21} curves in Fig. 3.12 (a) and S_{11} curves in Fig. 3.12 (b) have shown no significant differences with the varied arm width as expected. On the other hand, the on-state S_{21} curves in Fig. 3.12 (c) have shown a shift in the resonance frequency as a result of the varied inductances of the RF-MEMS switch with different arm widths The resonance frequency of the RF-MEMS switch is shifted from 132 GHz to 136 GHz, 141 GHz and 143 GHz with the increased arm widths from 2 µm to 2.5 µm, 3 µm, and 4 µm, respectively. For the optimized RF-MEMS switch, 3 µm arm width is chosen due to the targeted operating frequency of 140 GHz.

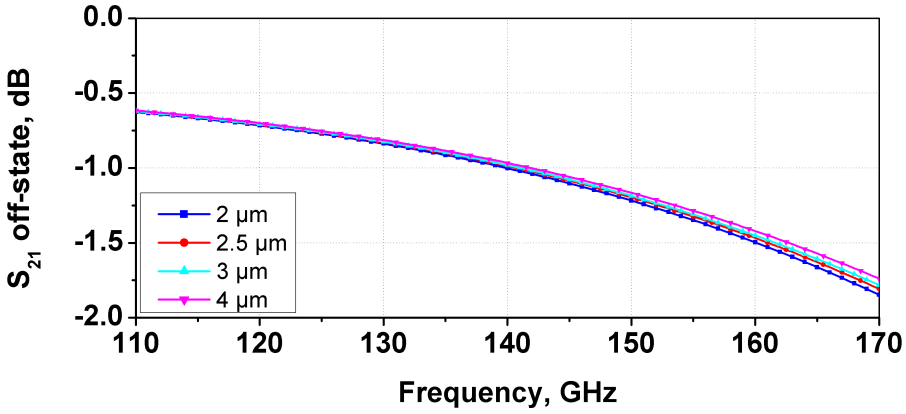

(a)

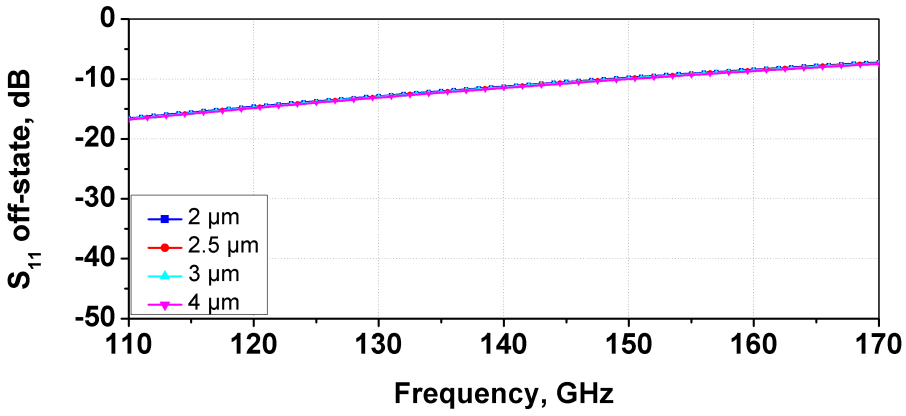

(b)

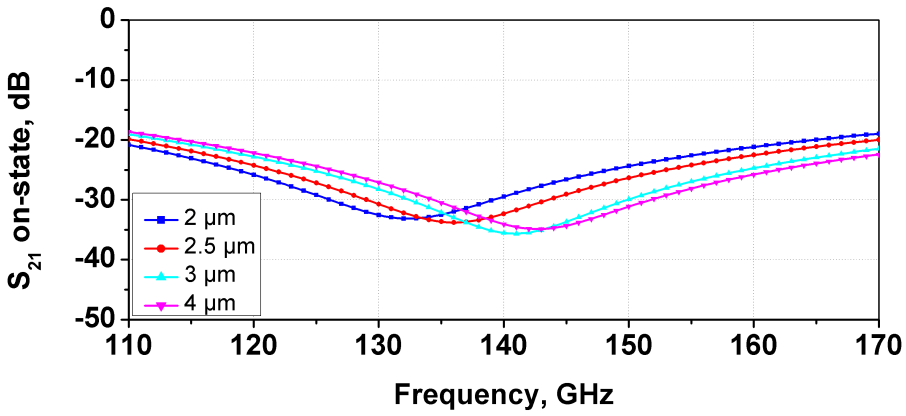

(c)

Figure 3.12: The S-parameter simulation comparison of the RF-MEMS switches for the varied arm width, (a) S_{21} off-state (b) S_{11} off-state and (c) S_{21} on-state.

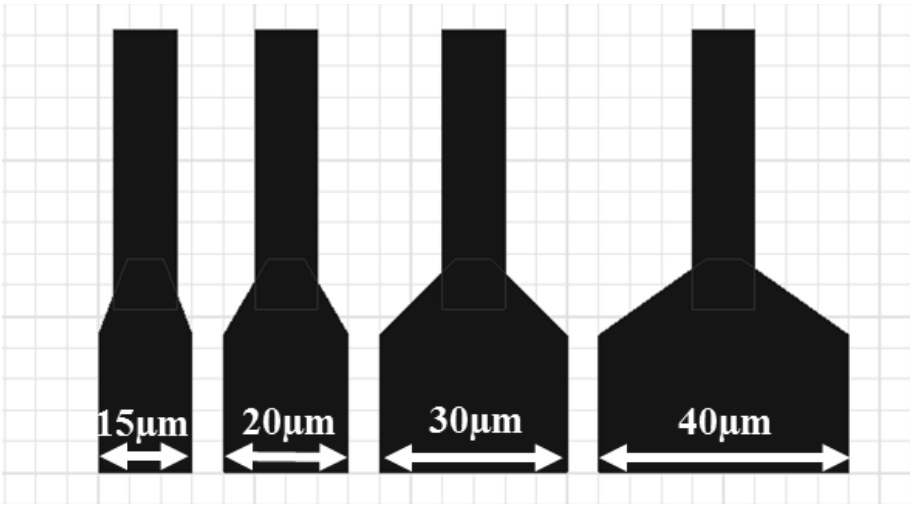

Figure 3.13: The generic view of the varied contact region width of the RF-MEMS switches (a) 15 µm (b) 20 µm (c) 30 µm (d) 40 µm.

Optimization of the RF-signal line contact region

An RF- SL defines the RF characteristics of an RF-MEMS switch, in terms of insertion loss, return loss and isolation. The central part of the SL, directly underneath the membrane, is named as the contact region. The area of the contact region determines the contact capacitance, C_{cont}, of the switch and the resonance frequency together with the inductance of the RF-MEMS switch (L_{total}). In the EM simulations, the contact region width of the RF-MEMS switch is varied between 15 µm to 40 µm with a fixed SL width of 10 µm. It should be noted that the contact region optimization is performed before the SL width optimization because the main resonance at down-state of the RF-MEMS switch is defined by the contact region capacitance. Fig. 3.13 shows the generic view of the varied contact region of the RF-MEMS switch. With the increased width of the contact region, the loss increases (Fig. 3.14 (a)) in off-state which can be correlated with the increased mismatch of the switch (Fig. 3.14 (b)). On the other hand, the S_{21} on-state curves in (Fig. 3.14 (c)) show the shift of the resonance frequency to the lower frequencies with the increased contact region widths, as expected. In summary, the S-parameter simulation results show a trade-off between the minimum loss and the maximum isolation at 140 GHz. Therefore for the next optimizations, 30 µm contact region width is chosen to obtain desired isolation values of more than 30 dB at 140 GHz.

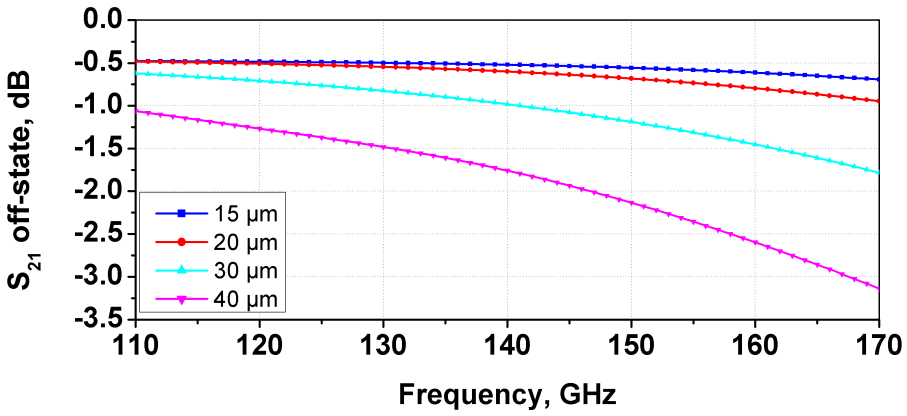

(a)

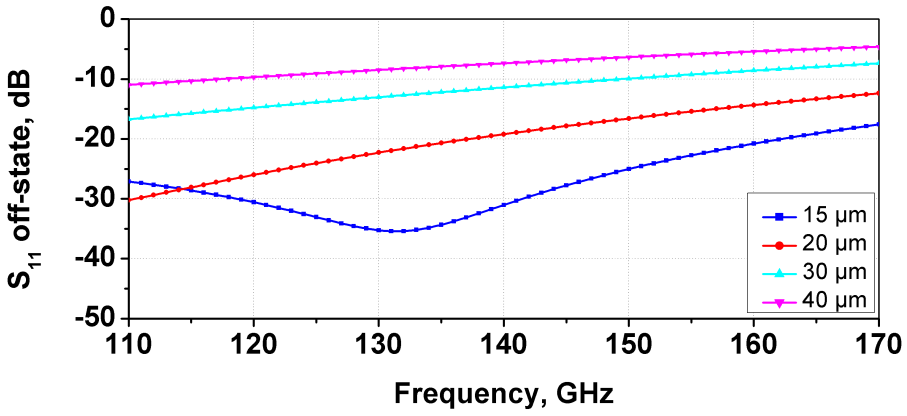

(b)

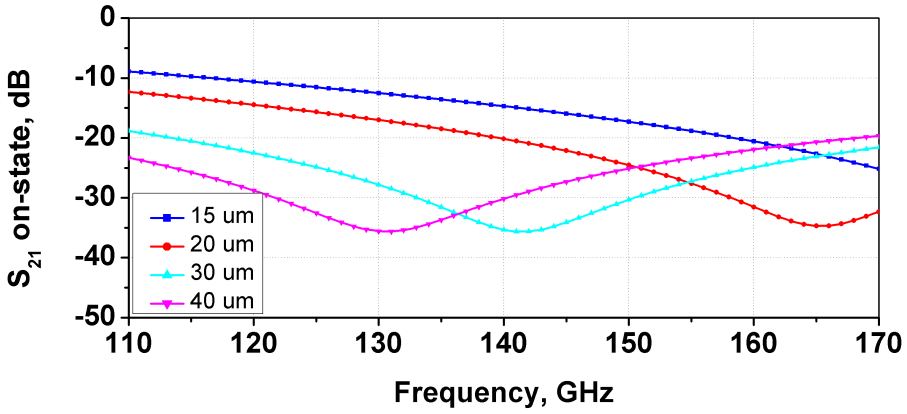

(c)

Figure 3.14: The S-parameter simulation comparison of the RF-MEMS switches for the varied contact region width, (a) S_{21} off-state (b) S_{11} off-state and (c) S_{21} on-state.

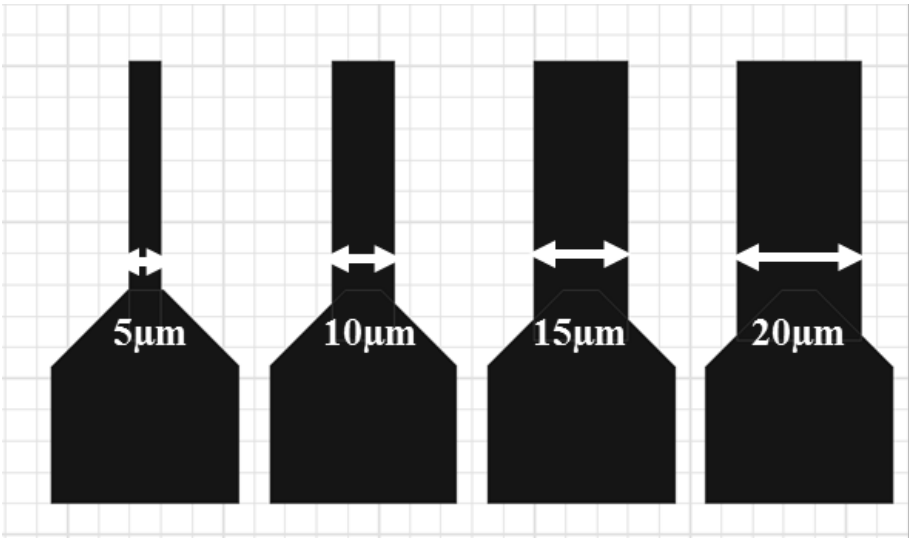

Figure 3.15: The generic view of the varied RF-signal line width of the RF-MEMS switches (a) 5 µm (b) 10 µm (c) 15 µm (d) 20 µm.

Optimization of the RF-signal line width

The designed SL consists of M5 layer in the contact region and continues in each side until the RF pads. During the simulations with the varying SL width, the contact region width is kept at 30 µm to provide a constant contact capacitance which ensures the desired isolation at 140 GHz of operation. Four different signal line widths (5 µm, 10 µm, 15 µm and 20 µm) are chosen for the comparison of the RF performances. Fig. 3.15 shows the generic view of the varied RF- SL width of the RF-MEMS switches. The corresponding S_{21} and S_{11} curves are given in Fig. 3.16. The S-parameter simulations have shown 0.48 dB variation in loss at 140 GHz between the switches with a 5 µm and a 20 µm signal line widths. The minimum loss (Fig. 3.16 (a)) and the best matching (Fig. 3.16 (b)) are achieved with the 5 µm width SL in the complete D-band. In on-state, the isolation curves (Fig. 3.16 (c)) of the switches have shown no shift in the resonance frequency. Despite the fact that the 5 µm width SL has shown the best performance in off-state, 10 µm width SL is selected for the optimized RF-MEMS switch for a small IL increase penalty to have a better stability of the process against the under etch of the SL during the releasing process. Here, the decision is taken considering both RF performance and process stability.

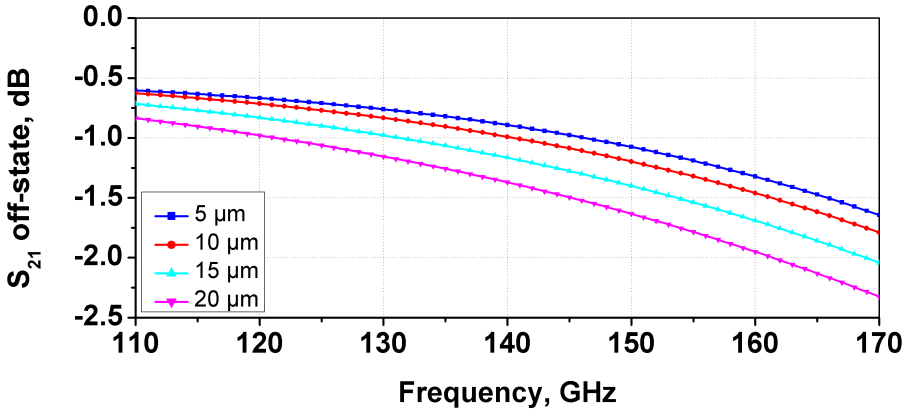

(a)

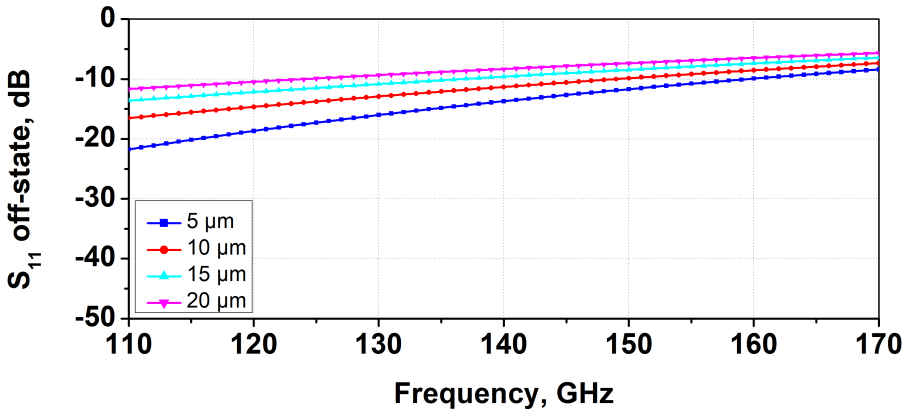

(b)

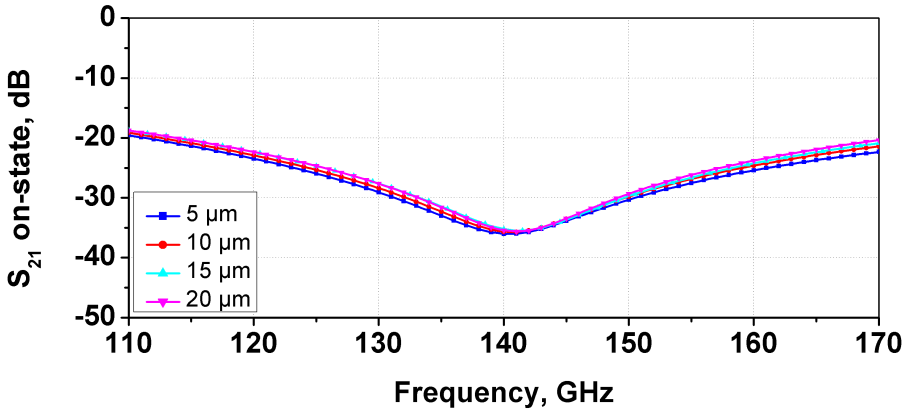

(c)

Figure 3.16: The S-parameter simulation comparison of the RF-MEMS switches for the varied RF-signal line width, (a) S_{21} off-state (b) S_{11} off-states and (c) S_{21} on-state.

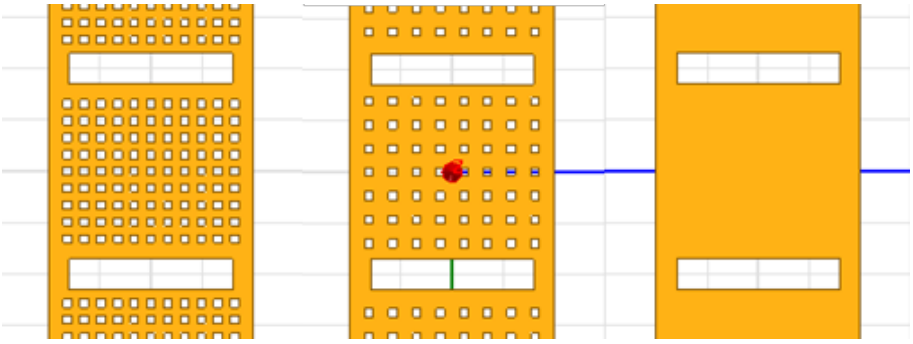

Figure 3.17: The generic view of TM1 membranes with (a) high, (b) low hole densities and (c) no holes.

Effect and optimization of the membrane hole density

The RF-MEMS switches are released through the holes of the membrane. In order to investigate the influence of the hole densities of membrane on the RF performance, three cases are compared with the EM simulations: 19.6 % hole density (Fig. 3.17 (a)), 11.1 % hole density (Fig. 3.17 (b)) and without holes (Fig. 3.17 (c)). Although the RF-MEMS switch without the releasing holes is not suitable for the releasing of the device, it is simulated to investigate the maximum achievable contact capacitance and corresponding RF performance without any holes. The S-parameter simulations have shown that there are no significant differences between the three cases in the S_{21} and S_{11} curves for the off-state (Fig. 3.18 (a), (b)) but shift in the resonance frequency for the on-state with the increased contact capacitances ($C_{contact}$) due to the lower hole densities on the membrane (Fig. 3.18 (c)). With the results of the hole effect, 11.1 % hole density membrane with the resonance frequency at 140 GHz is taken to be used during the next optimization steps.

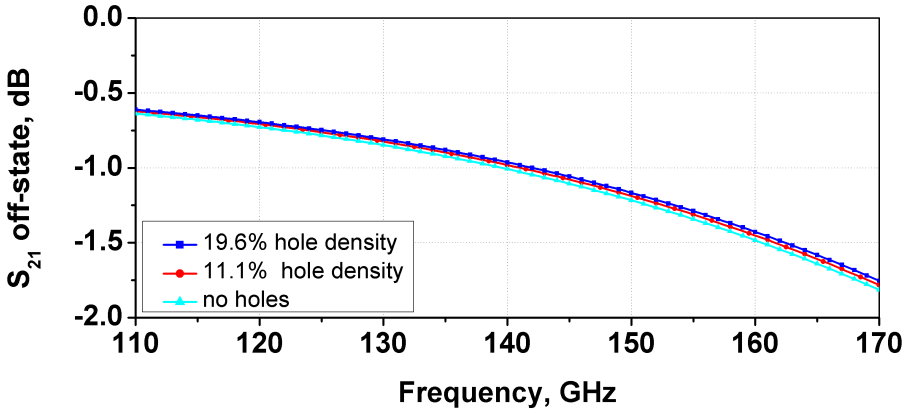

(a)

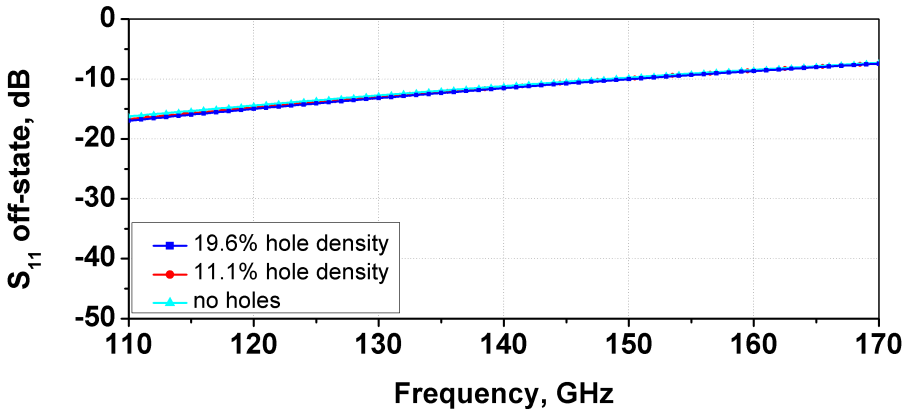

(b)

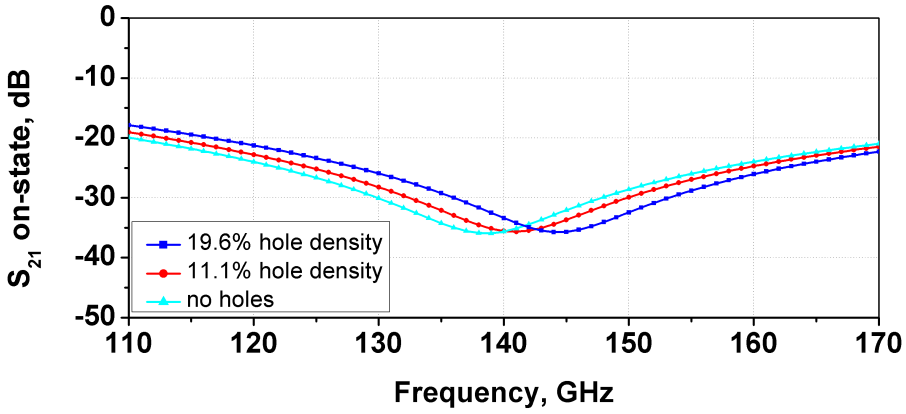

(c)

Figure 3.18: The S-parameter simulation comparison of the RF-MEMS switches for the varied TM1 membrane hole density, (a) S_{21} off-state (b) S_{11} off-state and (c) S_{21} on-state.

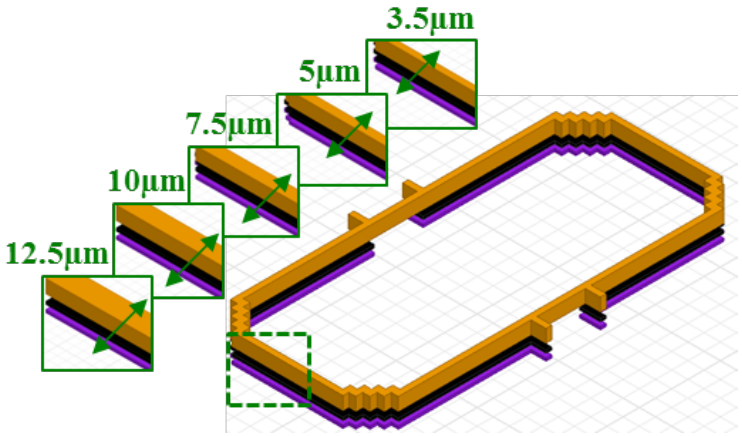

Figure 3.19: The generic view of the varied ground-ring width of the RF-MEMS switches (a) 3.5 µm (b) 5 µm (c) 7.5 µm (d) 10 µm and (e) 12.5 µm.

Optimization of the ground-ring width

The RF-MEMS switch needs a well-defined RF ground similar as in an mm-wave circuit to operate properly. Such effect can be ignored for lower frequency operations but especially for mm-wave RF-MEMS devices, the performance is significantly affected by the ground connections. Additionally, the RF ground should be connected to the membrane through the four arms and enclose the structure. However, the designed ring for RF ground has comparable size with the RF-MEMS switch and presumably introduces RF coupling of the SL and influences the RF performance of the switch. For these reasons, an investigation on the influence of the ground-ring width is essential. Fig. 3.19 shows the generic view of the designed RF ground-ring with the variation of the width from 3.5 to 12.5 µm by keeping the inner radius of the ring constant. The performed EM simulations have shown an increase of the loss in off-state (Fig. 3.20 (a)) with wider RF ground-ring which can be correlated with the increased RF signal coupling from the M5 SL to the TM1 of the ground-ring. The loss at 140 GHz is increased from 0.98 dB to 1 dB, 1.12 dB, 1.27 dB and 1.43 dB with respect to the increased ground-ring widths. The S_{11} curves of the off-state (Fig. 3.20 (b)) show the variation of the matching due to the varying ground-ring width. The return loss at 140 GHz varies between 8.2 dB and 11.3 dB. On the other hand, the ground-ring width has a very small effect on isolation in on-state (Fig. 3.20 (c)), since the RF signal is shorted to the ground. The RF ground-ring width value is chosen as 3.5 µm for the EM optimized RF-MEMS switch as it has given the minimum loss.

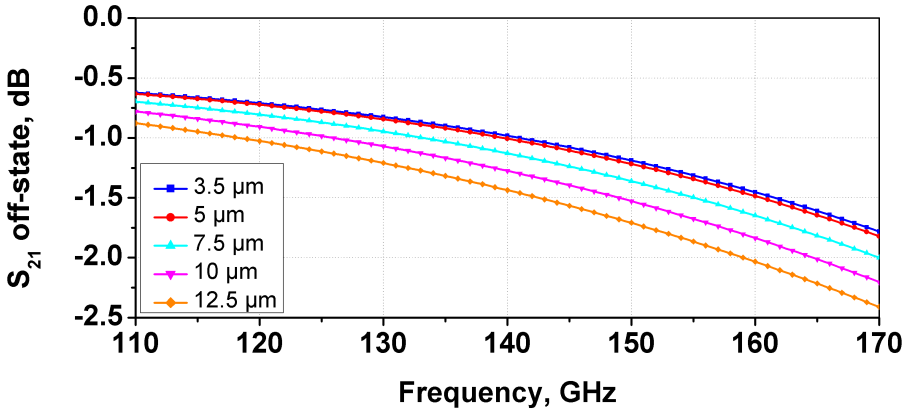

(a)

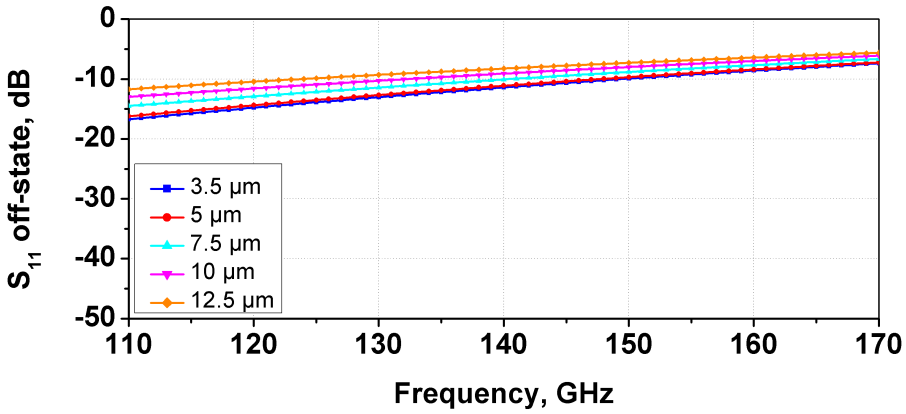

(b)

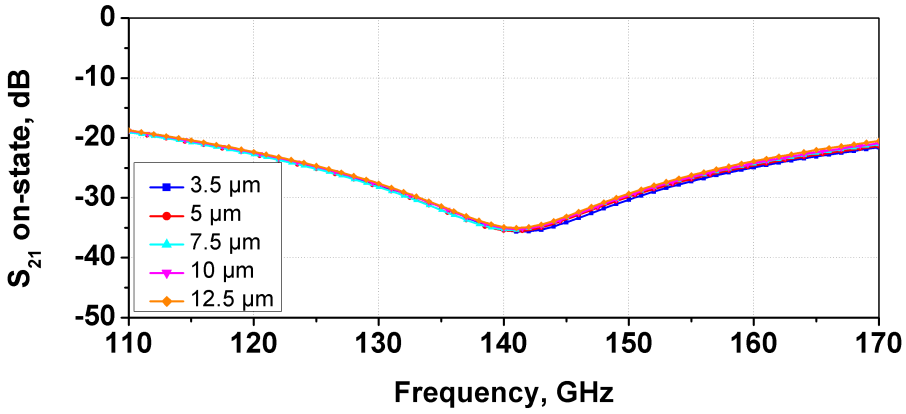

(c)

Figure 3.20: The S-parameter simulation comparison of the RF-MEMS switches for the varied ground-ring width, (a) S_{21} off-state (b) S_{11} off-state and (c) S_{21} on-state.

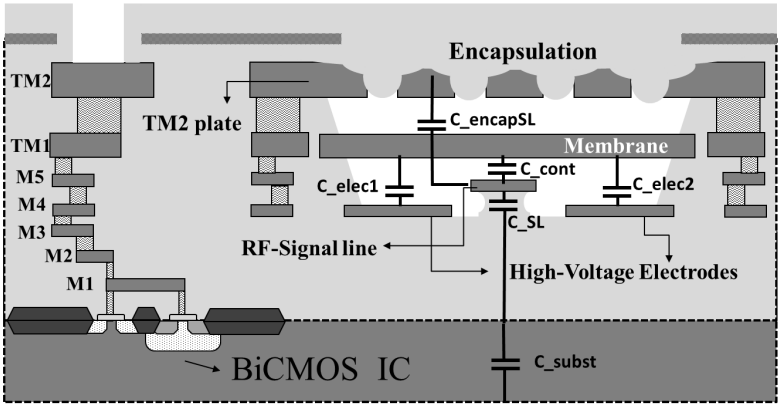

Figure 3.21: The cross section of WLE switch with lumped-element capacitances [80]. ©Cambridge University Press and the European Microwave Association 2017

3.2.2 Lumped-element modeling

Although the 3D FEM solvers provide accurate EM simulation results with the calculated d_{off} and d_{on} values from the extracted contact air capacitances (C_{off} and C_{on}), lumped-element models give faster simulation results. In [84], an accurate lumped-element model of RF-MEMS switches has been presented up to 110 GHz and has shown good matching with the S-parameter measurement results. Furthermore, a lumped model of an RF-MEMS switch extends the usage of the devices since with the help of a lumped-model, RF-MEMS switches can be simulated using a spice simulator in various circuits on system-level.

The main capacitances for the lumped-element model of the WLE RF-MEMS switch are shown on the process cross section in Fig. 3.21 [80]. Similar to the EM model, extracted contact parameters of the switch are necessary for the lumped element model of the RF-MEMS switch especially in on-state. Fig. 3.22 shows the lumped-element model of the WLE RF-MEMS switch. The extracted contact air capacitances (C_{cont}), C_{off} of 13.4 fF and C_{on} of 149 fF are used to model the contact region. The details of the C-V measurements are given in Section 3.2.3. Furthermore in the on-state model, the contact resistance of 5 kΩ is also considered.

For the S-parameter simulations with the lumped-element model, both ports of the device are terminated with 50 ohm. The M5 RF- SL is modeled using RLC elements between the ports and the arms of the membrane are modeled as inductors (L_{arm1}, L_{arm2}) with series resistors (R_{arm1}, R_{arm2}). C_{elec1} and C_{elec2} are the parasitic capa-

Table 3.1: Small-signal component values of the WLE RF-MEMS switch [80]. ©Cambridge University Press and the European Microwave Association 2017

Component	Value
L_{encap1}, L_{encap2}, L_{encap3}, L_{encap4}, L_{encap5}	70 pH
R_{encap1}, R_{encap2}, R_{encap3}, R_{encap4}, R_{encap5}, R_{arm1}, R_{arm2}, R_{SL1}, R_{SL2}, R_{SL3}, R_{SL4}, R_{SL5}, R_{SL6}	0.5 Ω
$C_{encapSL1}$, $C_{encapSL4}$	2 fF
$C_{encapSL2}$, $C_{encapSL3}$, C_{SL1}, C_{SL5}	3 fF
L_{arm1}, L_{arm2}	15 pH
C_{pad1}, C_{pad2}	11 fF
L_{SL1}, L_{SL6}	42 pH
L_{SL2}, L_{SL5}	3 pH
L_{SL3}, L_{SL4}	1 pH
C_{SL2},C_{SL4}	1.65 fF
C_{SL3}	10 fF
C_{subst}	170 fF
R_{subst}	400 Ω

Table 3.2: Small-signal component values of the WLE RF-MEMS switch, varied due to states [80]. ©Cambridge University Press and the European Microwave Association 2017

States	C_{elec1}, C_{elec2}	C_{cont}	R_{cont}
Off-state	10 fF	13.4 fF	(∞)
On-state	12 fF	149 fF	5 kΩ

citances between the TM1 membrane and the M4 HV electrodes. The values of the RLC elements of the lumped model for both states of the switch are given in Table 3.1 below. Due to the down bending of the TM1 membrane in on-state, C_{elec1} and C_{elec2} values are modeled slightly larger than the off-state values. Table 3.2 shows the varied C_{elec1}, C_{elec2} and C_{cont} values with respect to the states of the WLE RF-MEMS switch.

Both the 3D EM model and the lumped-element model consider the wafer-level encapsulation of the RF-MEMS switch. To include the WLE in the lumped model, TM2 plate is modeled with series inductances (L_{encap1}, L_{encap2}, L_{encap3}, L_{encap4}, L_{encap5}) and resistances (R_{encap1}, R_{encap2}, R_{encap3}, R_{encap4}, R_{encap5}). Additionally for its effect on the RF-MEMS switch, the coupling capacitances ($C_{encapSL1}$, $C_{encapSL2}$, $C_{encapSL3}$, $C_{encapSL4}$) between the TM2 plate and the M5 RF- SL is also inserted into the lumped-

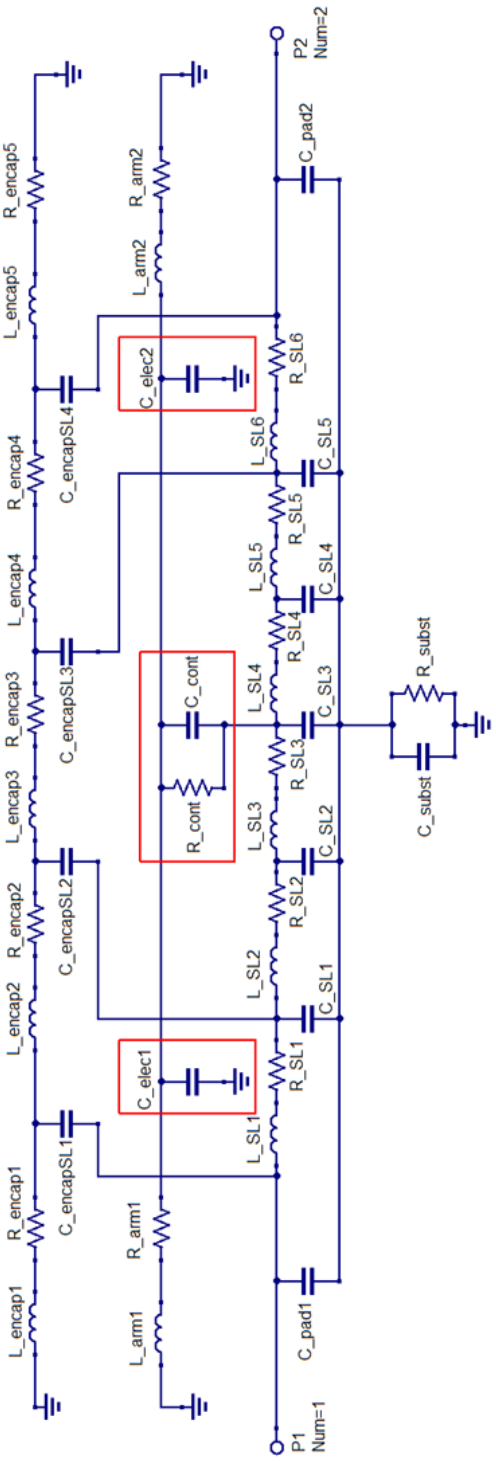

Figure 3.22: The lumped-element model of the WLE RF-MEMS switch. Red marked components have varied values with respect to the state of the switch [80]. ©Cambridge University Press and the European Microwave Association 2017

model. Lastly, the substrate effect is considered in the model and inserted as parallel capacitance (C_{subst}) and resistance (R_{subst}) between ground and the RF- SL. The comparison of the measured S-parameters of the fabricated WLE RF-MEMS switch with simulation results of the EM and lumped-element models are given in Section 3.2.3.

3.2.3 Experimental results

This section presents the different characterization methods and their results for the fabricated RF-MEMS switch. For the characterization of the D-band RF-MEMS switch, dynamic measurements are done by LDV and the electrical characterizations are done with C-V and S-parameter measurements.

Dynamic Measurements using Laser-Doppler-Vibrometer

A LDV (MSA-500, Polytec) [85] is used to characterize the dynamic behavior of the RF-MEMS switch. It provides the total displacement of the moving parts, switch-on time (t_{on}) and switch-off (t_{off}) time using optical methods. Therefore, the measurements can only be done on RF-MEMS switches without the deposition of HDR oxide for encapsulation. Despite the fact that the TM2 plate of the RF-MEMS switch makes the optical observation of the membrane displacement difficult, a careful study using the LDV is performed through the releasing holes to extract the displacement versus time curve. The generic view of the LDV setup is given in Fig. 3.23. The displacement versus time curve of the switch with the 60 V actuation voltage by the LDV measurement is shown in Fig. 3.24. From the figure, a displacement of 0.9 µm, t_{on} and t_{off} of less than 10 µs can be seen.

C-V Measurements

After the LDV measurements with the not-encapsulated RF-MEMS switch, the characterizations are continued with the encapsulated RF-MEMS switch for the extraction of the contact capacitances. The WLE RF-MEMS switch is initially characterized by C-V measurements.

For the C-V measurements, the high frequency impedance analyzer Agilent E4991 is used and the capacitance values are taken at 3 GHz. An Open/Short/Load calibration on an impedance standard substrate (ISS) from Cascade Microtech is applied to remove the parasitics of the measurement setup. The capacitance values are measured for the actuation voltages between -80 V and +80 V with 5 V steps. Fig. 3.25 shows the measured C-V graph of the WLE RF-MEMS switch and the extracted C_{cont} versus

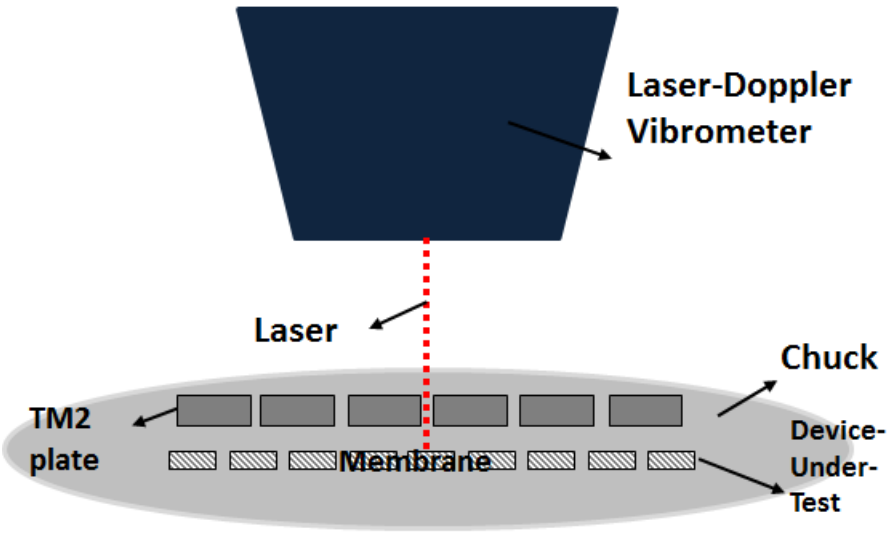

Figure 3.23: The generic schematics of the LDV setup [86].

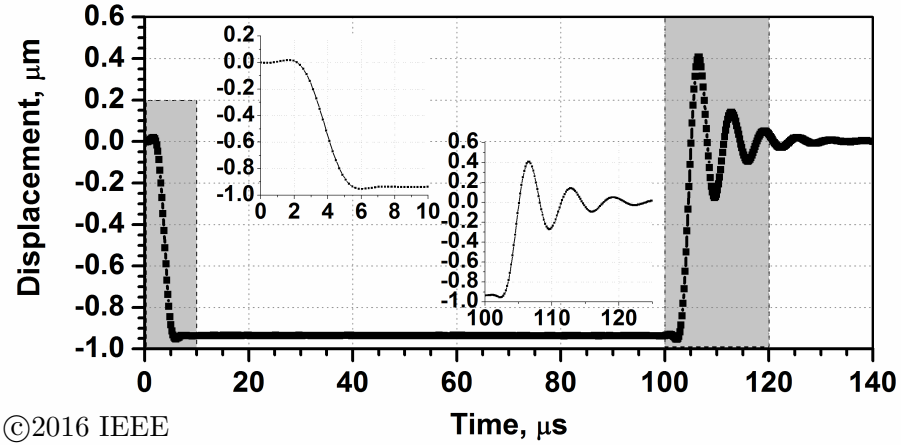

Figure 3.24: The displacement vs time curve of the not encapsulated RF-MEMS switch [86]. The displacement is ∼0.9 µm, the switch -on and -off times are of less than 10 µs.

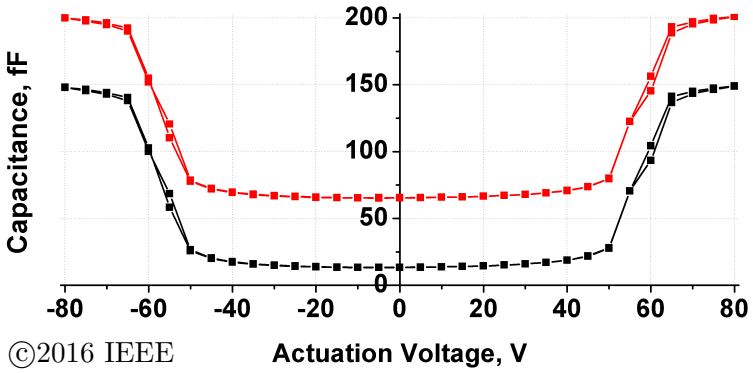

Figure 3.25: The measured C-V graph of the WLE RF-MEMS switch (red) and the extracted contact air capacitance vs voltage graph (black) [79, 80].

actuation voltage graph. The developed switch does not show any hysteresis, since the RF- SL distance to membrane is less than the 2/3 of the distance between the electrodes to membrane.

Extraction of the C_{cont}s is done with the help of an additional test structure that contains an RF- SL without membrane and TM2 encapsulation plate. With the test structure, the coupling capacitance (52 fF) from the signal line to ground ring and the Si substrate is measured and the C_{cont}s are extracted by its subtraction. The C_{cont}s are extracted as 13.4 fF C_{off} and 149 fF C_{on} with a C_{on}/C_{off} ratio of 11.1. Moreover it is observed that the pull-in occurs after 50 V and the C_{on} is stable after 65 V of actuation.

S-Parameter Measurements

Two port on-wafer S-parameter measurements of the WLE RF-MEMS switch are performed from 110 GHz to 170 GHz on semi-automated wafer probe station. The S-parameter measurements are performed with a setup from Rohde & Schwarz, consisting of a 4 port ZVA24 as vector network analyzer (VNA) / system controller and two ZVA170 Millimeter-Wave Converters. The Cascade 75 µm pitch infinity(R) ground signal ground (GSG) waveguide probes were connected via the WR6 waveguide s-bend with the millimeter-wave modules. For the calibration, the ISS 138–356 was placed together with an RF absorber on an auxiliary ceramic chuck and a full two port Thru-Reflect-Reflect-Match (LRRM) calibration was performed. To actuate the membrane of the RF-MEMS switch, Agilent Source Measurement Module E5281B was used.

Fig. 3.26 shows the comparison between the measured S-parameters of the fabricated

WLE RF-MEMS switch with simulation results of the EM and the lumped-element models. With the developed RF-MEMS switch, better than 0.67 dB insertion loss and more than 16 dB isolation in all D-band is achieved. The measured S_{21} curve in off-state (Fig. 3.26 (a)) shows a loss of 1.07 dB and the measured S_{11} curve in off-state (Fig. 3.26 (b)) is 9.13 dB at 140 GHz. For the insertion loss curves (Fig. 3.26 (c)), the signal reflection due to mismatch [87] is considered by equation 3.3. In the end of the EM optimization steps, the measured S-parameter results of the RF-MEMS switch give 0.6 dB insertion loss (Fig. 3.26 (c)) and 33.8 dB isolation (Fig. 3.26 (d)) at 140 GHz. Both EM model and lumped-element model simulation results are in good agreement with the measured S-parameter results in the D-band. The small differences between the measurement and simulation curves can be explained with the difficulty of calibration in frequencies above 100 GHz.

$$IL = 10 \cdot log \frac{|S_{21}|^2}{1 - |S_{11}|^2} \tag{3.3}$$

Lastly, Fig. 3.27 shows the S_{21} and S_{11} curves of the WLE RF-MEMS switch with the varied actuation voltages from 0 V to 80 V with 5 V steps. From the figure it can be observed that the switch is in off-state until 50 V, in transition in 55 and 60 V and in on-state from 65 to 80 V, which is also verified by the C-V measurements (Fig. 3.25).

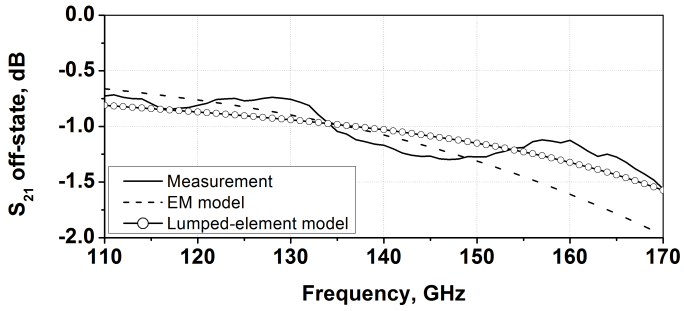

(a)

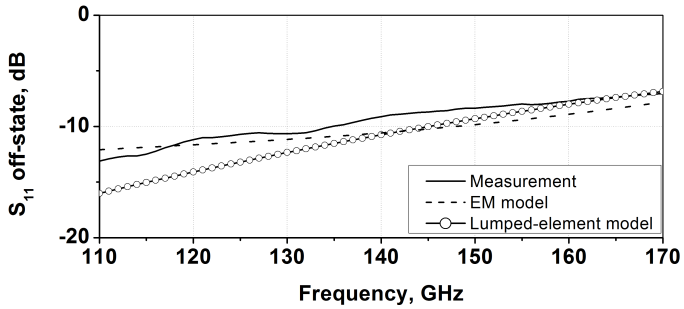

(b)

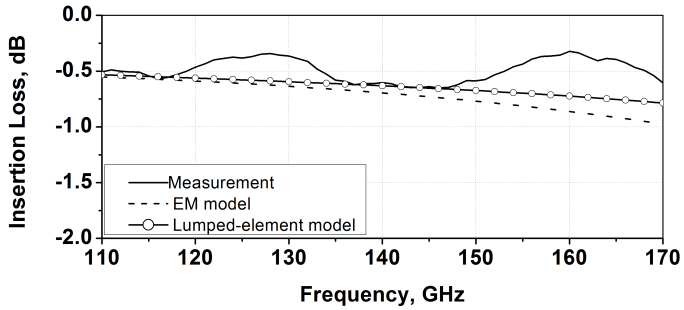

(c)

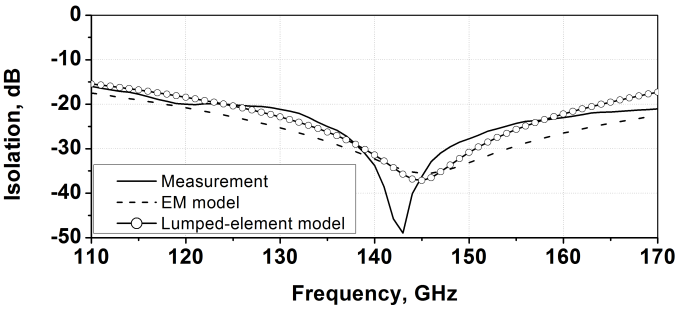

(d)

Figure 3.26: The comparison of the measured, electromagnetic modeled and small-signal modeled S-parameters for (a) off-state S_{21}, (b) off-state S_{11}, (c) off-state insertion loss and (d) on-state isolation of the WLE RF-MEMS switch.

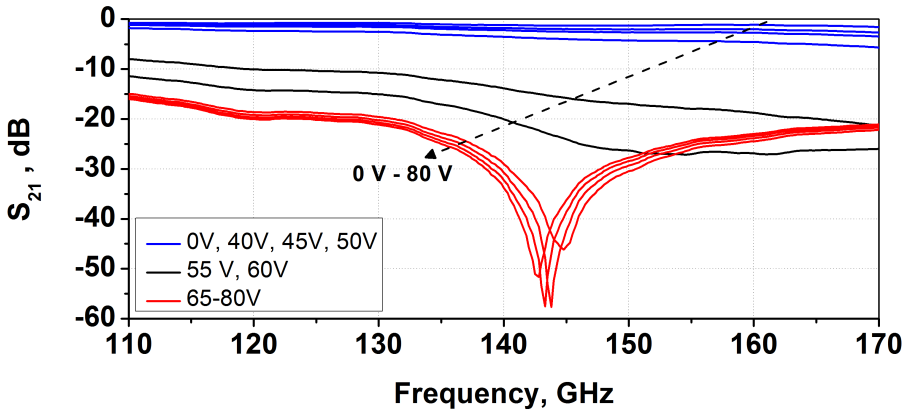

(a)

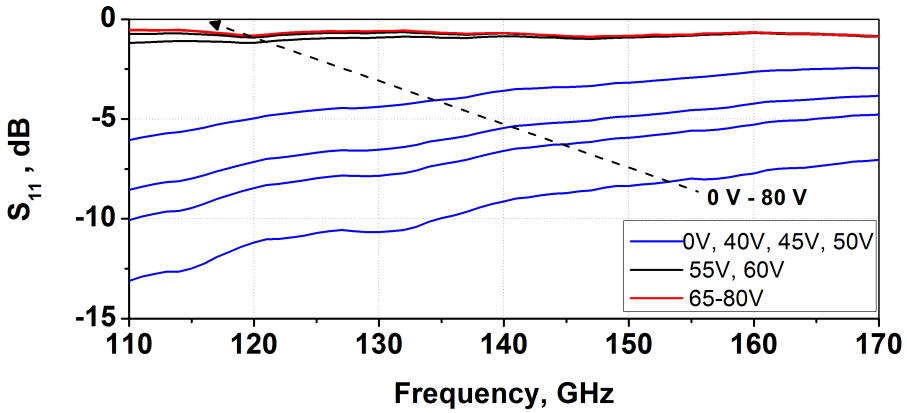

(b)

Figure 3.27: The measured S-parameters of the WLE RFMEMS switch for (a) S_{21} and (b) S_{11} with actuation voltages from 0 V to 80 V (with 5 V steps).

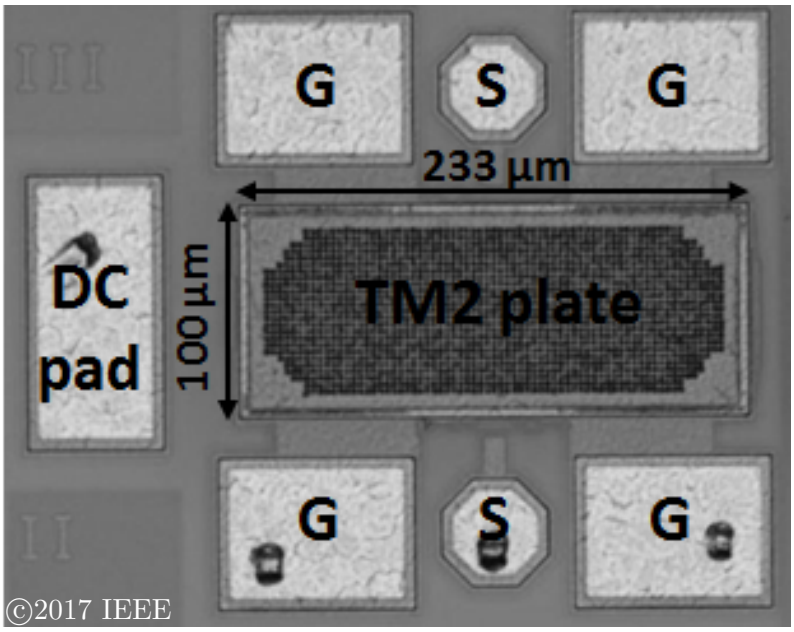

Figure 3.28: The fabricated J-band SPST RF-MEMS switch with the TM2 plate [21].

3.3 J-band RF-MEMS SPST Switch

This section presents the EM modeling, lumped-element modeling and experimental results of an RF-MEMS switch for J-band applications that is fabricated in a 0.13 µm SiGe BiCMOS process technology. Fig. 3.28 shows the microscope image of the fabricated J-band RF-MEMS switch in 0.13 µm SiGe BiCMOS process technology.

3.3.1 Electromagnetic modeling

For the development of an 240 GHz targetted J-band RF-MEMS switch, an EM model is built up in ANSYS HFSS 3D FEM solver (Fig. 3.29 (a)). IHP's 0.13 µm SiGe BiCMOS technology has a mean value of 900 nm as the distance between the TM1 and the M5 layer, which forms the distance between the membrane and the RF-SL of the designed switch. However, the C_{off} and C_{on} of the RF-MEMS switch can vary with the process variations across the wafer such as different surface roughness, metal and oxide thicknesses or stress behavior of the suspended TM1 membrane. As a result of the variable contact air capacitances, it is essential to estimate the possible RF performance variation of the RF-MEMS switch before the fabrication.

For the RF performance estimations, parametric EM simulations are performed with different d_{off} and d_{on} distances which simulate the aforementioned contact air

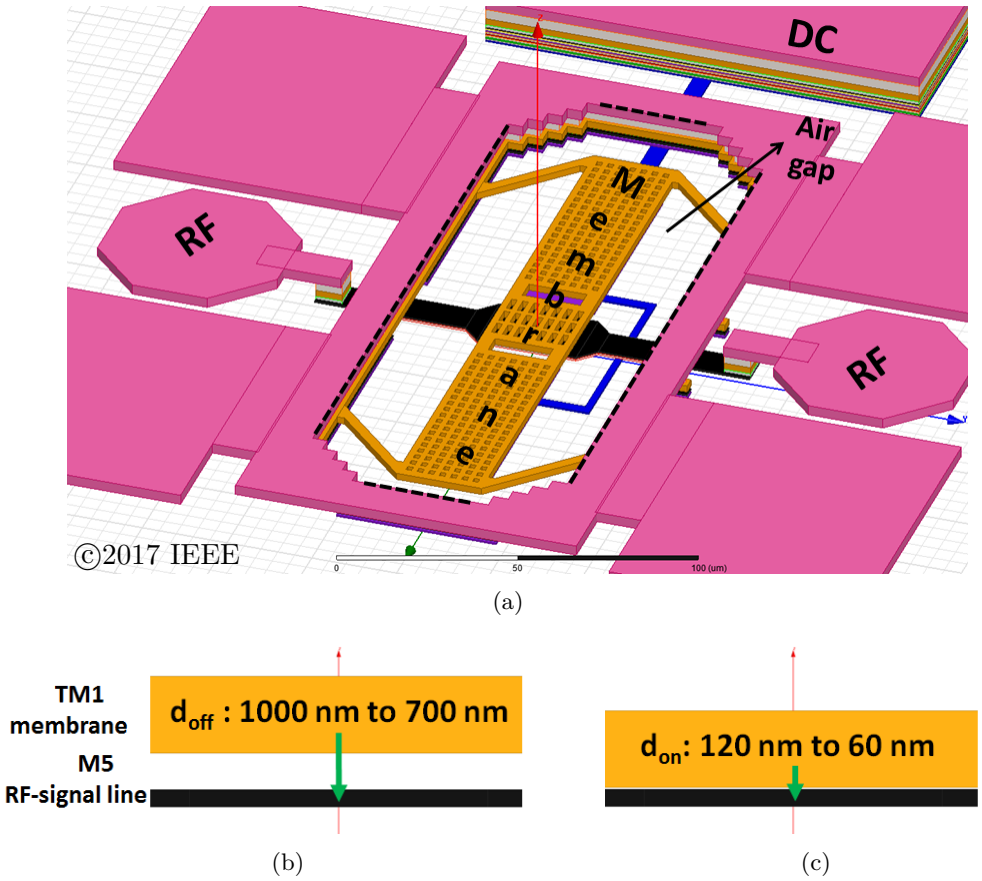

Figure 3.29: (a) EM simulation model of the J-band BiCMOS embedded RF-MEMS switch (with the hidden TM2 plate) in ANSYS HFSS , (b) parametric swept d_{off} values, (c) parametric swept d_{on} values [21].

capacitance variations (Fig. 3.29(b), (c)). For the off-state EM simulation, the membrane position is swept from 100 nm above the specified TM1 layer until 200 nm below with a step size of 50 nm. The calculated maximum and minimum C_{cont} vary between 4.45 fF and 6.36 fF. The change of the insertion loss with different d_{off} values is shown in Fig. 3.30. Varying the d_{off} by 300 nm leads to only 0.06 dB change of the insertion loss at 240 GHz but 0.48 dB change at 325 GHz. For the on-state, the parametric EM simulations are extended with different d_{on} values for the isolation. The simulation results are shown in Fig. 3.30 for the decreased d_{on}, starting from 120 nm down to 60 nm with 10 nm steps. The maximum and minimum d_{on} vary the calculated contact air capacitance between 37.1 fF and 74.2 fF. Such small gaps (d_{on}) between the moving membrane and the RF- SL are crucial to model the down-state, resulting due to the process variations. Decreasing the d_{on} by 60 nm causes the shift of the resonance frequency from 276 GHz to below 220 GHz. Shortly, this method is useful for preliminary simulations to estimate the possible range of the resonance frequency. However, the extraction of the C_{off} and C_{on} from the C-V measurements of the RF-MEMS switches is essential to have accurate EM simulation results for the 220 – 325 GHz frequency band. The values of d_{off} and d_{on} can be calculated by using the simple parallel plate capacitor equation with the extracted contact air capacitances and inserted into the EM simulation model.

3.3.2 Lumped-element modeling

Since lumped-element models give faster simulation results and the RF-MEMS switch can be simulated in various circuits, a lumped-model is also created for the J-band RF-MEMS switch. The main capacitances considered in the lumped-element model of the J-band RF-MEMS switch are similar compared to the lumped-element model of the WLE D-band switch which are shown on the process cross section in Fig. 3.21 [80]. Thus, the same detailed lumped-element model of the D-band RF-MEMS switch can be used for the J-band RF-MEMS switch which is given in Fig. 3.22. The extracted contact air capacitances, C_{off} of 6.07 fF and C_{on} of 53.3 fF are used to model the contact region. Furthermore in the on-state model, the contact resistance of 5 kΩ is also considered.

For the S-parameter simulation with the lumped-element model, Port1 and Port2 are terminated with 50 ohm. The M5 RF- SL is modeled using RLC elements between the two ports and the arms of the membrane are modeled as inductors (L_{arm1}, L_{arm2}) with series resistors (R_{arm1}, R_{arm2}). C_{elec1} and C_{elec2} are the parasitic capacitances between the TM1 membrane and the M4 HV electrodes. The values of the RLC elements of the

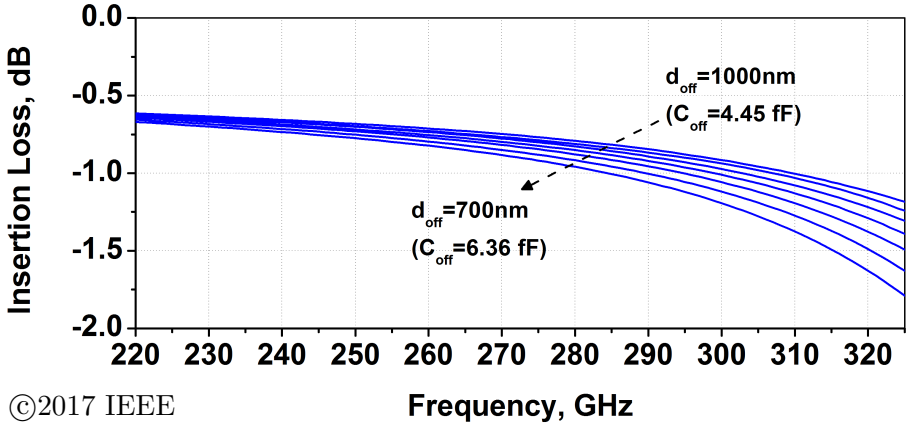

(a)

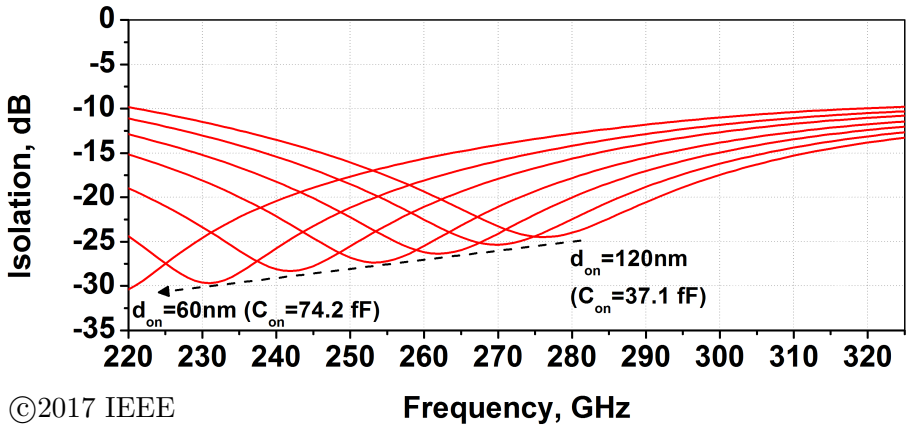

(b)

Figure 3.30: The simulated S-parameters of the RF-MEMS switch with varying TM1 membrane to M5 RF- SL distance due to process variation: (a) insertion loss, (b) isolation [21].

Table 3.3: Small-signal component values of the J-band RF-MEMS switch.

Component	Value
L_{encap1}, L_{encap2}, L_{encap3}, L_{encap4}, L_{encap5}	70 pH
R_{encap1}, R_{encap2}, R_{encap3}, R_{encap4}, R_{encap5}, R_{arm1}, R_{arm2}, R_{SL1}, R_{SL2}, R_{SL3}, R_{SL4}, R_{SL5}, R_{SL6}	0.5 Ω
$C_{encapSL1}$, $C_{encapSL4}$	0.7 fF
$C_{encapSL2}$, $C_{encapSL3}$	1.1 fF
C_{SL1}, C_{SL5}	2 fF
L_{arm1}, L_{arm2}	12.5 pH
C_{pad1}, C_{pad2}	7 fF
L_{SL1}, L_{SL6}	27.5 pH
L_{SL2}, L_{SL5}	2 pH
L_{SL3}, L_{SL4}	0.66 pH
C_{SL2},C_{SL4}	1 fF
C_{SL3}	4.8 fF
C_{subst}	170 fF
R_{subst}	400 Ω

Table 3.4: Small-signal component values of the J-band RF-MEMS switch, varied due to states.

States	C_{elec1}, C_{elec2}	C_{cont}	R_{cont}
Off-state	6.5 fF	6.07 fF	(∞)
On-state	7.8 fF	53.3 fF	5 kΩ

lumped model for both states of the J-band switch are given in Table 3.3 below. Due to the down bending of the TM1 membrane in on-state, C_{elec1} and C_{elec2} values are modeled slightly larger compared to the off-state values. Table 3.4 shows the varied C_{elec1}, C_{elec2} and C_{cont} values with respect to the states of the J-band RF-MEMS switch.

Both the 3D FEM model and the lumped-element model consider the effect of the TM2 plate on the RF-MEMS switch. The TM2 plate is modeled with series inductances (L_{encap1}, L_{encap2}, L_{encap3}, L_{encap4}, L_{encap5}) and resistances (R_{encap1}, R_{encap2}, R_{encap3}, R_{encap4}, R_{encap5}). Additionally for its effect on the RF-MEMS switch, the coupling capacitances ($C_{encapSL1}$, $C_{encapSL2}$, $C_{encapSL3}$, $C_{encapSL4}$) between the TM2 plate and the M5 RF- SL is also inserted into the lumped-model. Lastly, the substrate effect is considered in the model and inserted as parallel capacitance (C_{subst}) and

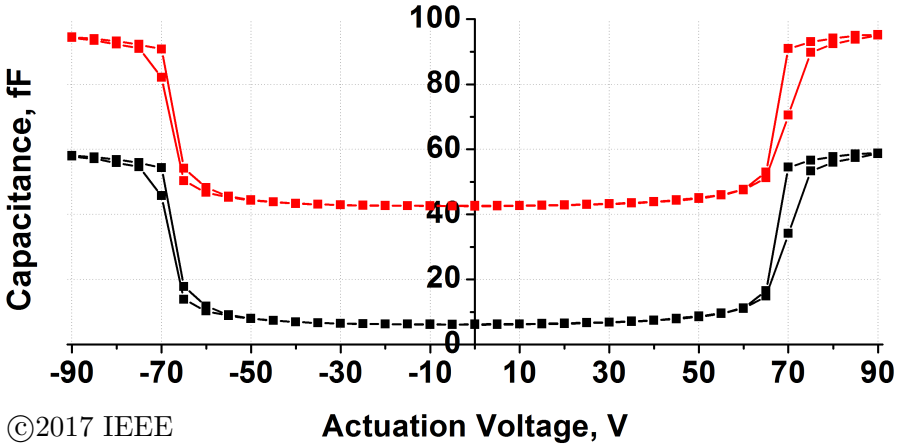

Figure 3.31: The measured C-V characteristic of the J-band RF-MEMS switch (red) and the extracted contact air capacitance vs. voltage graph (black) [21].

resistance (R_{subst}) between ground and the RF- SL. The comparison of the measured S-parameters of the fabricated J-band RF-MEMS switch with simulation results of the EM and the lumped-element models will be given in the next section, Section 3.3.3.

3.3.3 Experimental Results

C-V Measurements

The fabricated RF-MEMS switch is initially characterized by C-V measurements. The capacitances are measured for the actuation voltages between -90 V and +90 V with 5 V steps. Fig. 3.31 shows the measured C-V characteristic and the extracted contact air capacitance versus actuation voltage graph of the RF-MEMS switch. Extraction of the contact air capacitances is done with the help of an additional test structure that consists of an RF- SL without a membrane and a TM2 plate. With the test structure, the coupling capacitance of 36.4 fF from the RF- SL to the silicon substrate is measured and the contact air capacitances are extracted by its subtraction. The contact air capacitances are extracted as 6.07 fF C_{off} and 53.3 fF C_{on} (at 75 V) with a C_{on}/C_{off} ration of 8.78. Based on the measured C_{on} and C_{off} capacitances (Fig. 3.31) and the considered ∼500 µm^2 contact area, d_{off} is calculated as ∼750 nm and d_{on} as ∼80 nm. Furthermore, it is observed from the figure that the pull-in occurs after 65 V and C_{on} is stable after 70 V.

S-Parameter Measurements

After the C-V analysis of the RF-MEMS switch, two port on-wafer S-parameter measurements of the device are performed from 220 to 325 GHz at room temperature on the semi-automated probe station. For the S-parameter measurements, a setup from Rhode & Schwarz, consisting of a 4 port ZVA24 as VNA / system controller and two ZVA325 Millimeter-Wave Converters, are used. The 50 µm pitch GSG waveguide probes from Picoprobe are connected via a WR3 waveguide s-bend with the millimeter-wave modules. For calibration, the ISS, CS-15, is placed together with an RF absorber on an auxiliary ceramic chuck and a full two port Thru-Reflect-Match plus (LRM+) calibration is performed. To actuate the membrane of the RF-MEMS switch a 100 V Agilent Source Measurement Module E5281B is used.

The comparison of the measured and simulated S-parameter results of the RF-MEMS switch is given in Fig. 3.32. The switch shows maximum isolation of 24.67 dB at 238 GHz with the insertion loss of 0.49 dB. The return loss is better than 9.6 dB over the J-band. The calculated d_{off} and d_{on} values from the C-V measurements are then inserted into the EM model for the comparison with the S-parameter measurements. The 3D FEM simulation and lumped-element model results are in good agreement with the measured S-parameters in the 220 – 325 GHz frequency band. It should be noted that the differences between the measurement and simulation curves can be explained by the calibration challenges in these high frequencies.

Lastly, Fig. 3.33 shows the S_{21} and S_{11} curves of the RF-MEMS switch with the varied actuation voltages between 0 V and 90 V with 5 V steps. It can be observed from the measured data that the switch is in off-state until 55 V, in transition at 60 V and 65 V and in on-state between 70 V to 90 V of actuation.

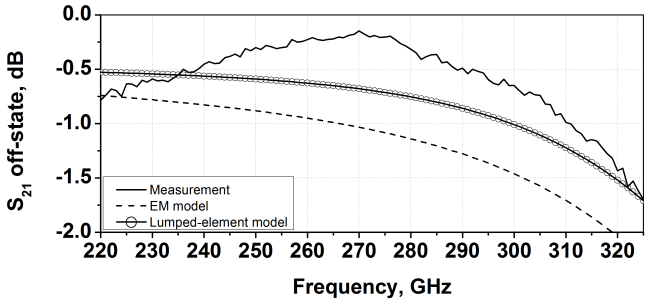

(a)

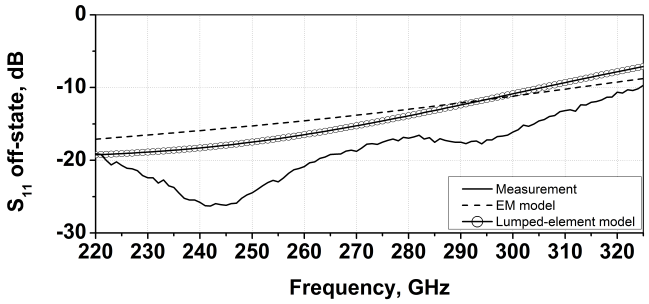

(b)

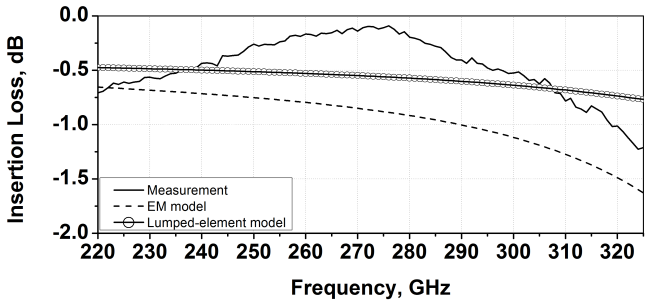

(c)

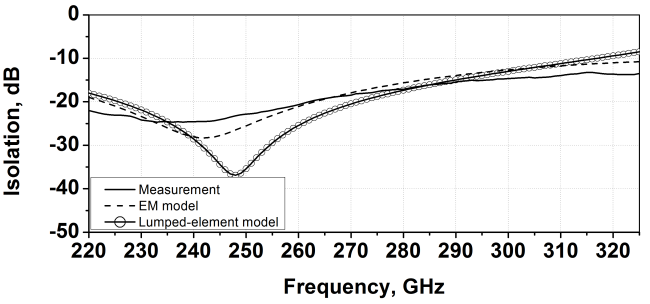

(d)

Figure 3.32: The comparison of the measured, electromagnetic modeled and small-signal modeled S-parameters for (a) up-state S_{21}, (b) up-state S_{11}, (c) up-state insertion loss and (d) down-state isolation of the J-band RF-MEMS switch.

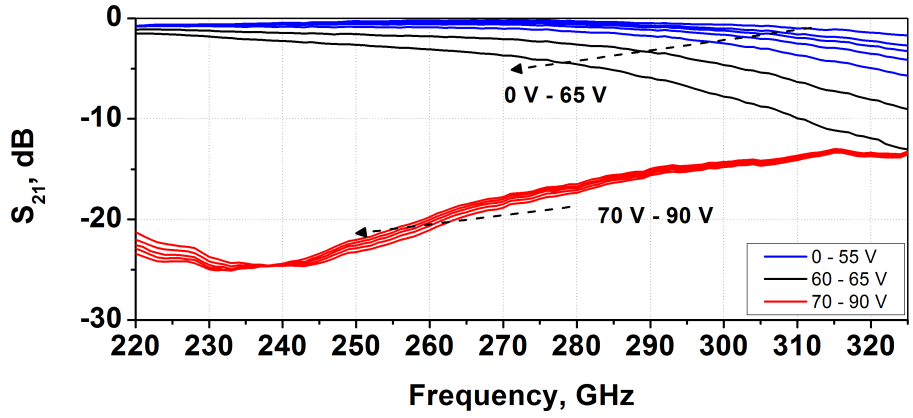

(a)

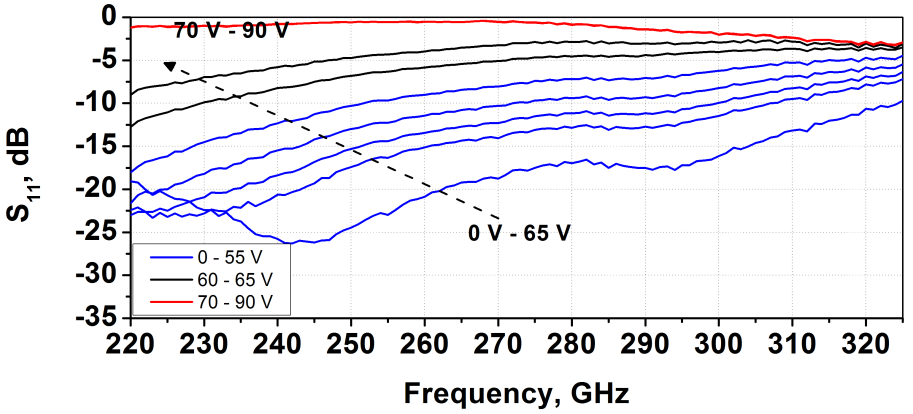

(b)

Figure 3.33: The measured S-parameters of the J-band RF-MEMS switch with the actuation voltages from 0 V to 90 V (with 5 V steps): (a) S_{21}, (b) S_{11}.

3.4 Conclusion

With 3D FEM solvers, it is possible to estimate the RF performances of RF-MEMS switches. However accurate EM models need a careful modeling approach as one of the key elements, the contact air capacitances, in both on and off-states of the switches are not known precisely before their fabrication. With the known contact areas of the switches and the measured contact air capacitances, the distances between the RF- SL and the released membrane can be calculated by the simple parallel plate capacitance formula. Afterwards the calculated distances can be given into the EM models for the accurate EM simulations.

Beside the accurate EM models, lumped-element models of the RF-MEMS switches are also necessary especially for the circuit designers to predict the RF-behavior of the designed circuits using the switches. The lumped-element models of the RF-MEMS switches increase the simulation speed remarkably compared to the EM models and give the possibility to simulate the switches with various circuits in a system level.

Section 3.2 has presented the EM modeling, EM optimizations, lumped-element modeling and the electrical characterizations of a WLE RF-MEMS switch embedded in a 0.13 µm SiGe BiCMOS process technology for D-band applications. A 140 GHz targeted operating frequency WLE RF-MEMS switch with its measured 0.6 dB of insertion loss and 33.8 dB of isolation at 140 GHz, has been successfully demonstrated. To the best of my knowledge, the 0.13 µm BiCMOS embedded thin film wafer-level encapsulated RF-MEMS switch is the first RF-MEMS switch in literature which operates with state of the art RF performances in D-band. The results of the both EM model and lumped-element model of the switch are in good agreement with the S-parameter measurements in D-band [80] which proves the efficiency of the models.

Section 3.3 has presented a J-band RF-MEMS switch embedded in a 0.13 µm SiGe BiCMOS process technology. To the best of my knowledge, the demonstrated SPST switch is the first RF-MEMS switch presented in the complete J-band. This work shows that the BiCMOS embedded RF-MEMS switches can provide low insertion loss and high isolation at sub-THz frequencies [21].

Table 3.5 shows the measured performance of the designed D-band [80] and J-band [21] SPST switches in comparison to the other published and above 110 GHz SPST switches in the literature, based on the indium phosphide (InP)-double hetero bipolar transistor (DHBT), SOI-CMOS and BiCMOS technologies. In comparison with the published SPST performances in literature, it is clearly shown that the presented D-band and J-band RF-MEMS SPST switches have the minimum insertion losses.

Table 3.5: Measured Performance Comparison of mm-wave SPST Switches.

	This work: D-band switch [80]	[88]	[89]	This work: J-band switch [21]
Technology	0.13 µm SiGe BiCMOS	45 nm CMOS SOI	250 nm InP DHBT	0.13 µm SiGe BiCMOS
Topology	RF-MEMS	Double Shunt FET	Double-shunt transistor	RF-MEMS
Frequency (GHz)	110 – 170	140 – 220	220 – 320	220 – 325
IL (dB)	0.6 @ 140 GHz	<1.5	1.2 – 2.9	0.44* – 1.7
ISO (dB)	33.8 @ 140 GHz	15 – 20	13.1 – 15.7	13.24 – 25.1
IP_{1dB} (dBm)	—	7 – 8 @ 50 – 65 GHz	16 @ 300 GHz (simulated)	—
Chip Area (mm^2)	—	0.2	0.12	0.1

* at 240 GHz

4 RF-MEMS Design Examples

4.1 Introduction

In this chapter, RF-MEMS design examples in both 0.13 µm and 0.25 µm SiGe BiCMOS technologies are described. In Section 4.2, firstly a D-band SPST switch in SG13 BiCMOS technology is presented which is used as a key element to design a D-band SPDT switch in the same technology. The developed D-band RF-MEMS based SPDT switch is presented with its EM modeling and S-parameter measurement results. In the next section, Section 4.3, Si cap packaged K-band RF-MEMS test vehicles for space applications are presented in SG25 BiCMOS technology. Firstly the C-V and S-parameter measurement results of the two test vehicles; RF-MEMS based SPST and SPDT switches are presented for both before and after Si cap packaging cases. Later on, the yield analyses of all the test vehicles; RF-MEMS based SPST, SPDT switches and a on-chip CP integrated with the RF-MEMS based SPST switch are given. Lastly, the effect of Si cap packaging is studied in more detail with 3D EM simulations in HFSS which shows the RF performance differences with different resistivity values of the Si caps.

4.2 D-Band RF-MEMS SPDT Switch

SPDT switches are essential components for many different RF and mm-wave system applications; such as in 94 GHz passive imaging systems as Dicke SPDT switch [90, 91] and in 120 – 140 GHz radar and sensor transceivers as transmit/receive (T/R) switch. In most of these applications, SPDT is the component coming right after the antenna; thus adding its noise figure on top of the overall noise figure of the system. Therefore, a very low loss is required by the SPDTs in order to achieve a high overall system performance.

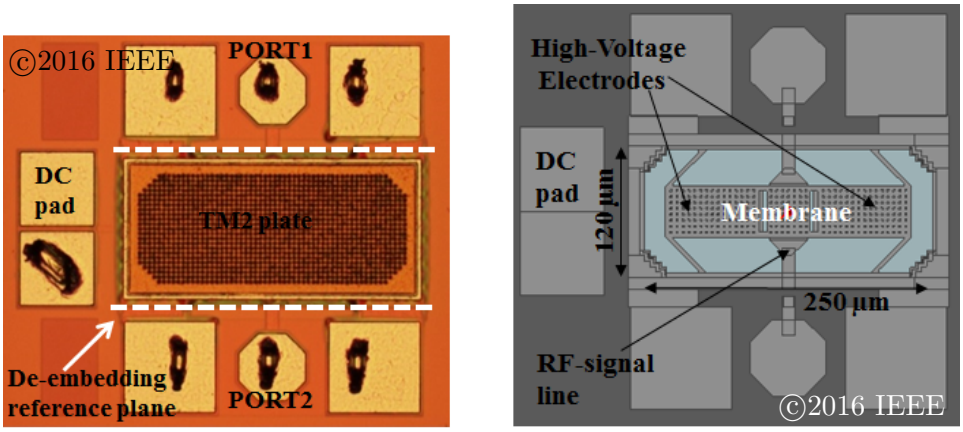

(a) (b)

Figure 4.1: Fabricated D-band RF-MEMS SPST switch with the TM2 plate and its top generic view with hidden TM2 plate [86].

Key element of the RF-MEMS SPDT Switch: RF-MEMS SPST Switch

A D-band RF-MEMS SPST switch is used as the key element of the RF-MEMS SPDT switch. The main differences between this key element RF-MEMS SPST switch and the developed switch in Section 3.2 are the design of the RF pads and the encapsulation. Similar to the key-element RF-MEMS SPST switch, the designed RF-MEMS SPDT switch is also fabricated as shown in Section 2.3. Both switches are not encapsulated but include the TM2 plate on top for their protection. Additionally, both of the switches include different RF pads compared to the RF pads of the presented WLE switch in Section 3.2. Fig. 2.11 (b) shows the process integration scheme of the RF-MEMS SPST and SPDT switches in the 0.13 µm SiGe BiCMOS technology without WLE and the micrograph of the fabricated RF-MEMS SPST switch is shown in Fig. 4.1 (a). The top view of the embedded RF-MEMS SPST switch with hidden TM2 plate is shown in Fig. 4.1 (b).

The two port S-parameter measurements of the fabricated RF-MEMS SPST switch are performed from 110 to 170 GHz with the measurement setup explained in Section 3.2.3. Although the fabricated RF-MEMS SPST switch has pull-in after 45 V; 60 V is applied for down-state to obtain a stable down-state capacitance. The measured and simulated S-parameter results of the SPST switch are given in Fig. 4.2, both for the up and down states. The results are in very good agreement in the 110 – 170 GHz frequency band with respect to the EM simulations, performed by the 3D FEM solver. After the S-parameter measurements of the RF-MEMS switch, the pad capacitances

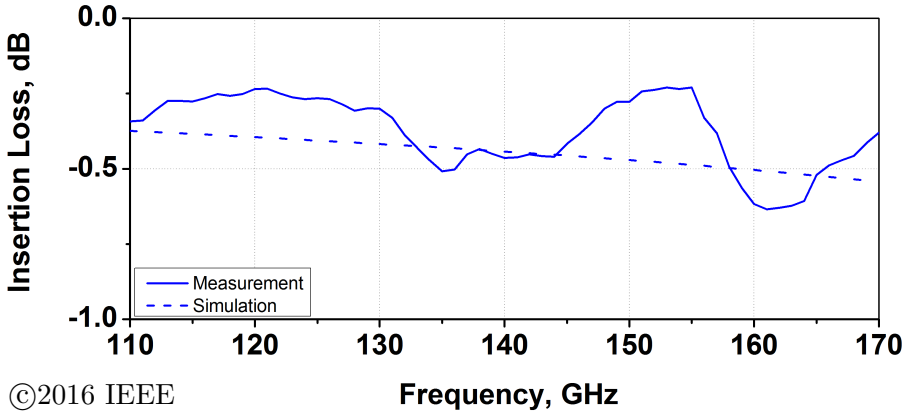

(a)

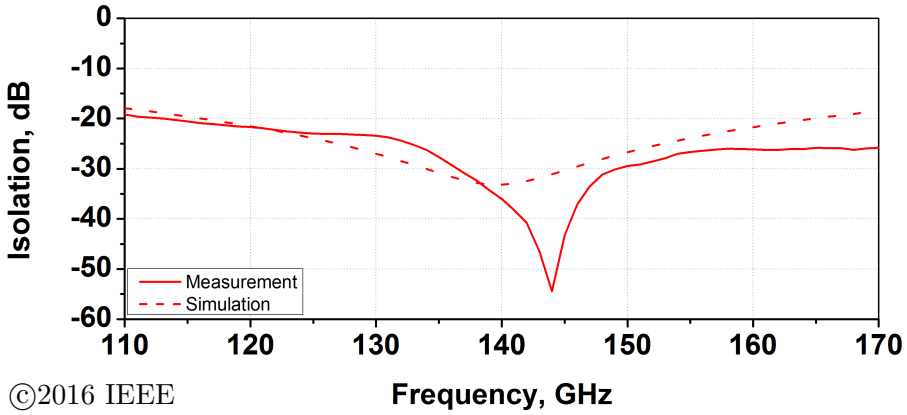

(b)

Figure 4.2: Comparison of the measured open-deembedded S-parameters with the EM simulation results for the insertion loss in the up-state (a) and the isolation in the down-state (b) of the D-band RF-MEMS SPST switch [86].

are removed by the open-deembedding and an insertion loss of 0.46 dB and an isolation of 36 dB at 140 GHz are extracted.

RF-MEMS switches can be used in different mm-wave circuits under different RF and DC bias conditions. During the design phase of the circuits, the bias conditions should already be considered as RF-MEMS switch has connections to the other components of the circuit. Due to non-accurate bias conditions on the RF-MEMS switch two different failures can occur; namely the self-actuation and latching.

Self actuation: Self actuation occurs in a high DC or RF level difference applied between the RF- SL and membrane of the RF-MEMS switch. The applied bias difference generate a force to pull the membrane down without any additional voltage applied to the electrodes. The self-actuation voltage of the D-band is measured as 21 V. This bias difference between the RF- SL and membrane is quite high as its compared to the typical biasing conditions of mm-wave circuits. It should be also noted that typical RF power levels in mm-wave circuits are also much less than the power values which can cause the self-actuation. Indeed, self-actuation does not create a significant problem for the circuits that include the presented D-band RF-MEMS switch.

Latching: Latching also occurs in a high DC or RF level difference applied between the RF- SL and membrane of the RF-MEMS switch which generates a force to keep the membrane in down state. To investigate the latching of the D-band RF-MEMS switch, the switch is actuated by applying 60 V to the electrodes and the voltage applied to the RF- SL is increased simultaneously to catch the latching voltage. The latching voltage of the D-band switch is measured as 3.9 V when 60 V is applied to the electrodes. Shortly, the DC potential difference between RF- SL and the membrane should be below 3.9 V for the safe operation in mm-wave circuits.

4.2.1 EM modeling

By using the above presented RF-MEMS SPST switch, a 140 GHz center frequency D-band SPDT switch design is targeted. The RF-MEMS based SPDT switch is designed with a tee junction that is connected to the two RF-MEMS SPST switches with each side $\lambda/4$ microstrip lines. The schematic of the designed SPDT switch and its EM model in HFSS are shown in Fig. 4.3 and Fig. 4.4, respectively.

The designed SPDT switch behaves like a thru between Port1 and Port2 (transmission mode) when the switch-1 (SW#1) is open (up-state) and the switch-2 (SW#2) shorted (down-state). The SW#2 together with the transmission line (T-line) in the right side branch provide an open circuit since the $\lambda/4$ T-lines is capacitively shorted to ground by the SW#2. Although the right side branch is supposed to provide open circuit, due to the non-optimized T-line lengths, a specific loss always occurs in this branch. In the second state, the switch has a high attenuation between Port1 and Port2 (isolation mode) when the SW#1 is in short (down-state) and the SW#2 is in open (up-state). In this state, the Port1 and the Port2 are isolated by the help of $\lambda/4$ T-lines and the SW#1 in the left side branch.

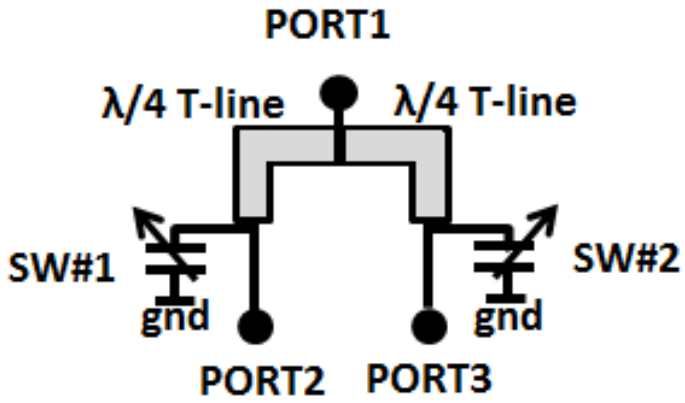

Figure 4.3: Schematic of the SPDT switch in shunt configuration [86].

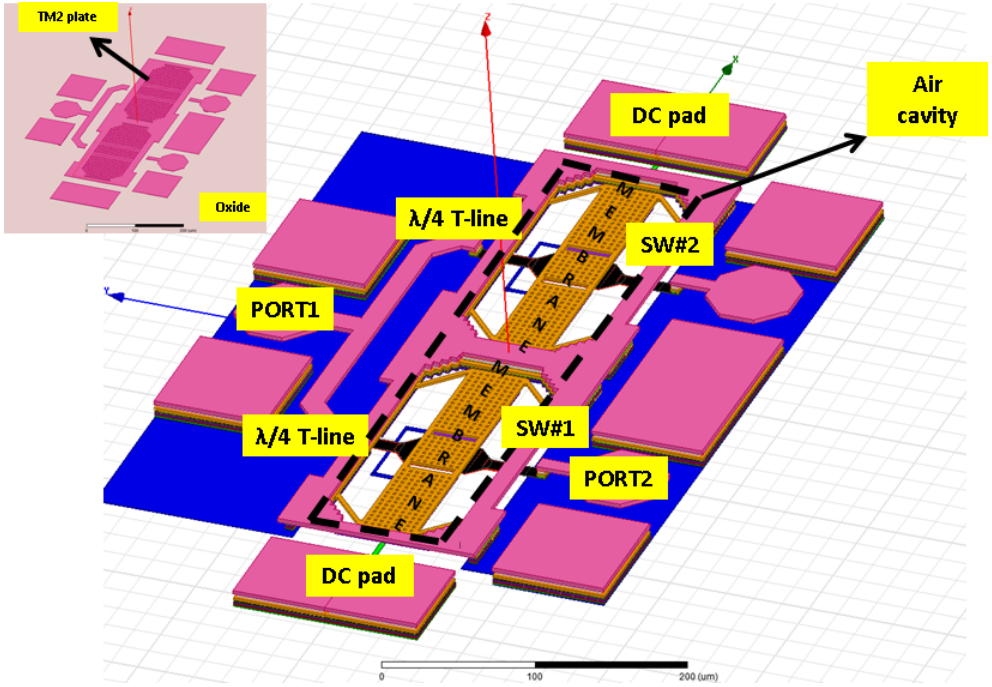

Figure 4.4: EM Simulation model in ANSYS HFSS for both states of the D-band RF-MEMS SPDT Switch.

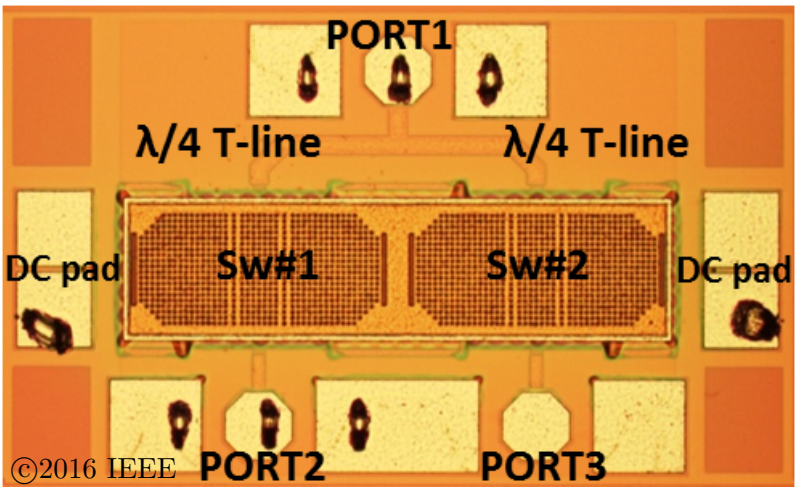

Figure 4.5: Micrograph of the D-band RF-MEMS based SPDT switch [86].

Since the comparison of the S-parameter measurements and the EM simulations of the RF-MEMS SPST switch has given a very good match, same distances in SPST switch's EM model are also given to the SPDT switch's EM model between the TM1 membrane and M5 RF- SL. For the EM simulations of the insertion loss between Port1 and Port2 of the SPDT switch, the SW#1 SPST switch's TM1 membrane is kept in up-state position while SW#2 SPST switch's TM1 membrane is shifted into the down-state position. On the other hand for the EM simulations of the isolation between Port1 and Port2 of the SPDT switch, the SW#1 SPST switch's TM1 membrane is shifted into the down-state position while SW#2 SPST switch's TM1 membrane is kept in up-state position. During the development of the RF-MEMS based SPDT switch, the tee junction is fine tuned with comparing different simulation results to provide the minimum insertion loss and maximum isolation at 140 GHz targetted frequency. After the RF optimizations of the RF-MEMS based SPDT switch in HFSS, the developed SPDT switch is fabricated in IHP's SG13 BEOL, excluding the WLE process. Fig. 4.5 shows the micrograph of the fabricated D-band RF-MEMS based SPDT switch.

4.2.2 Experimental results

The RF measurements of the fabricated RF-MEMS based SPDT switch were done by only two port S-parameter measurements because of the lack of ground signal ground signal ground (GSGSG) probes in 110 – 170 GHz frequency band. With the actuation of the SW#2 membrane (Fig. 4.5) with 60 V while SW#1 was in off-state (no voltage at the electrode), the measurement results have shown an insertion loss of 1.42 dB at

140 GHz. In the case of an actuated SW#1 (60 V actuation voltage) while SW#2 is in off-state (no voltage at the electrode) an isolation of 54.5 dB is measured at 140 GHz. Fig. 4.6 shows the performance of the RF-MEMS based SPDT switch for the measured and the EM simulated cases. For the 2-port simulations, the non-contacted third port is also left as open circuit, like in the case of the measurements. To check the effect of the not connected third port, an additional setup is created where all the three ports are terminated with 50 Ω. The 3-port EM simulations show that the insertion loss and the isolation do not change significantly in the interested frequency band (Fig. 4.6). Additional to the D-band simulations, Fig. 4.7 shows the comparison of the 2-port and 3-port EM simulation results in a wider frequency band - from DC to 170 GHz. This comparison has shown that 3-port EM simulations give similar results with 2-port simulation in D-band for insertion loss and isolation graphs, however show differences below 110 GHz in insertion loss and isolation. Since the length of the $\lambda/4$ T-lines is optimized for the targetted 140 GHz, for higher or lower frequencies the length of the T-lines differs from $\lambda/4$. This causes differences in below 110 GHz frequencies due to the traveling of the RF-signal to both of the T-lines.

In literature, although there are no RF-MEMS based SPDT switches beyond 110 GHz, there are many studies on transistor based SPDT switches. Unlike the transistor based SPDTs, the RF-MEMS based SPDTs have much lower power consumption, can handle higher RF power and provide excellent linearity. Table 4.1 shows the measured performance of the designed RF-MEMS based SPDT switch in comparison to the other published millimeter-wave SPDT switches, based on the BiCMOS and SOI-CMOS based technologies. With a state of the art 0.13 µm SiGe BiCMOS technology, the designed SiGe HBT based SPDT in [92] has an insertion loss of 2.6 – 3 dB and a maximum isolation of 29 dB between 96 – 163 GHz. In [93], a single-shunt SPDT switch based on a 32 nm SOI CMOS technology with an insertion loss of 2.6 – 4 dB and an isolation of 22 dB in 110 – 170 GHz frequency band is published. Another doubled-shunt SPDT switch is demonstrated based on 45 nm SOI CMOS technology with insertion loss of 3 – 4.5 dB and isolation of 20 – 30 dB in 140 – 220 GHz frequency band. To the best of my knowledge, the results achieved in this study are the lowest insertion loss and the highest isolation of a SPDT reported in D-band [86].

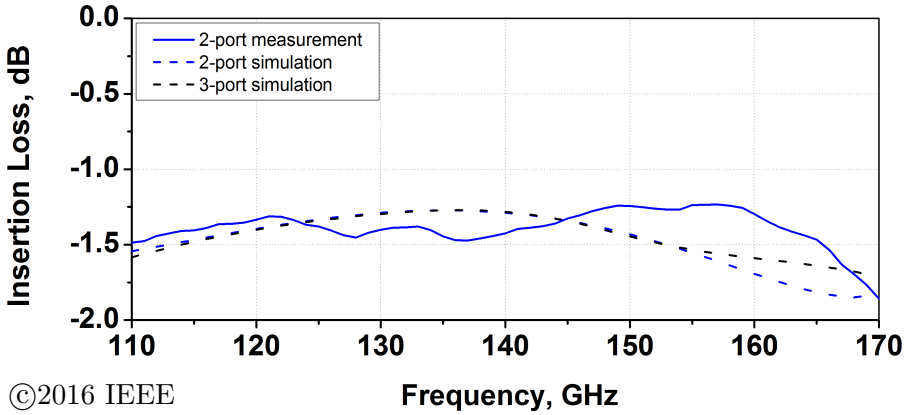

(a)

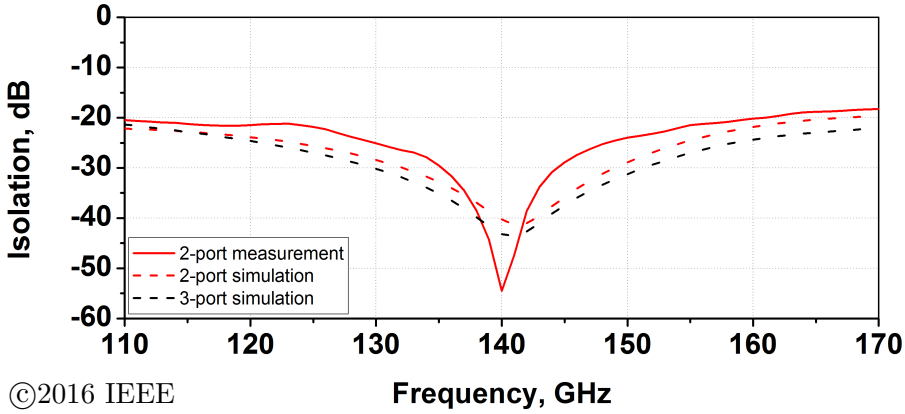

(b)

Figure 4.6: Comparison of the measured 2-port S-parameters of the SPDT between Port2 and Port1 with the EM simulation results: (a) insertion loss (SW#1 up-state, SW#2 down-state) and (b) isolation (SW#1 down-state, SW#2 up-state) [86].

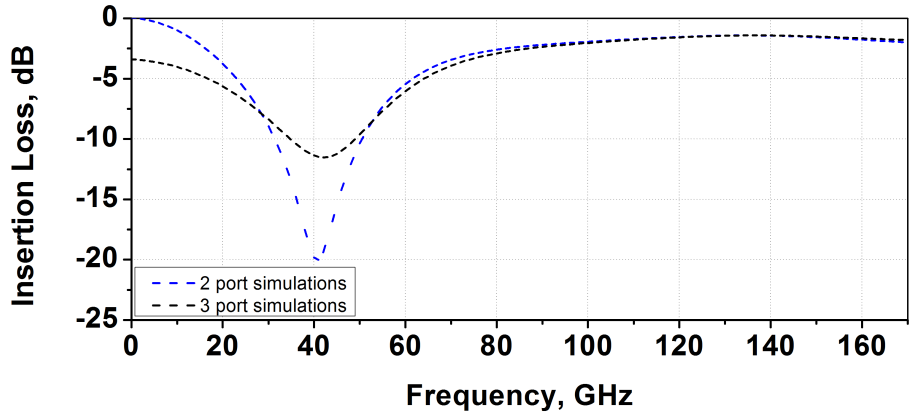

(a)

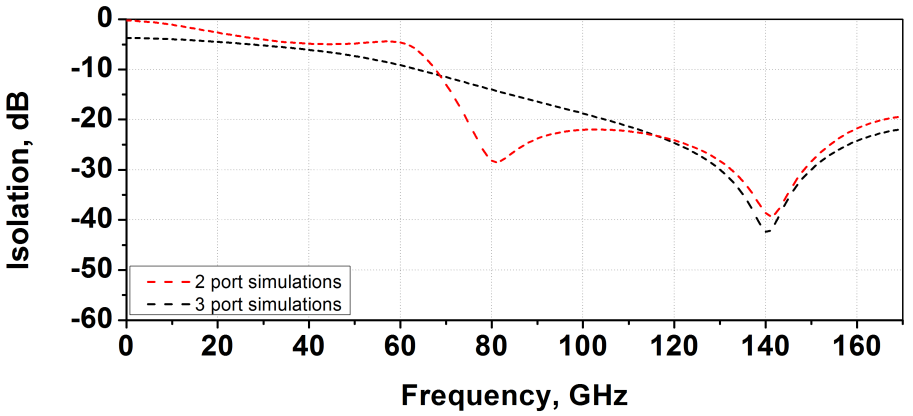

(b)

Figure 4.7: Comparison of the simulated 2–port and 3-port S–parameters of the SPDT between Port2 and Port1: (a) insertion loss (SW#1 up–state, SW#2 down–state) and (b) isolation (SW#1 down–state, SW#2 up–state).

Table 4.1: Measured Performance Comparison of mm-wave SPDT Switches [86].

	[92]	[93]	[88]	**This Work [86]**
Technology	0.13 µm SiGe BiCMOS	32 nm CMOS SOI	45 nm CMOS SOI	**0.13 µm SiGe BiCMOS**
Topology	Double Shunt Sat. HBT	Double Shunt FET	Double Shunt FET	**RF-MEMS**
Frequency (GHz)	96 – 163	110 – 170	140 – 220	**110 – 170**
IL (dB)	2.6 – 3	2.6 – 4	3 – 4.5	**1.23* – 1.86**
ISO (dB)	23.5 – 29	22	20 – 30	**18.25 – 54.5**
Switching Time	0.4 ns (simulated)	—	—	**<10 µs**

* at 157 GHz

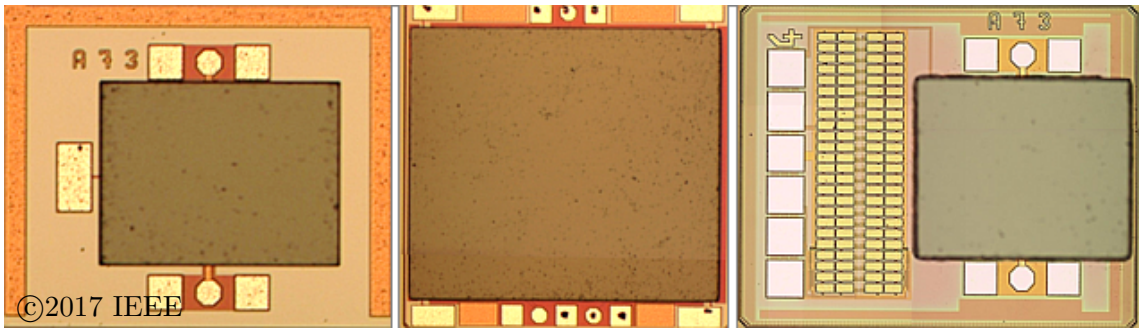

Figure 4.8: The microscope images of a designed, fabricated and packaged TCV (left), DEC (middle) and RIC (right) [71].

4.3 K-band RF-MEMS Test Vehicles for space applications

In the previous chapters, it has already been pointed to the importance of packaging for commercialization. In this section, RF-MEMS test vehicles for K-band space applications are demonstrated. The demonstrated test vehicles are embedded in IHP's 0.25 µm SiGe BiCMOS process and packaged with Si cap wafer-level packaging in Fraunhofer IZM, Berlin [69–71]. As required by the European Space Components Coordination (ESCC) specification (n° 2269010), three RF-MEMS test vehicles for space applications have been designed, fabricated and packaged (Fig. 4.8); namely the technology characterization vehicle (TCV), the dynamic evaluation circuit (DEC) and the representative integrated circuit (RIC).

- TCV is an RF-MEMS SPST switch.
- DEC is an RF-MEMS SPDT switch including the standard building block, TCV.
- RIC is an RF-MEMS SPST switch integrated together with an on-chip high-voltage CP.

All the fabricated RF-MEMS test vehicles are packaged by the Si cap wafer-to-wafer packaging technique explained in Section 2.2.2.

4.3.1 Experimental results

The designed and fabricated TCV, DEC and RIC are electrically characterized before and after the WLP to investigate the effect of the packages and the packaging processes on the RF performances and the mechanical behaviors (pull-in voltages). Since the performance of the RIC is identical to the TCV, the electrical characterization of the RIC only focuses on the DC measurements of the integrated CP.

For the capacitance measurements [79] of the TCV and DEC, the RF-MEMS switches are actuated between -45 V to +45 V with 5 V steps and the contact capacitances are extracted using the high frequency impedance analyzer (Agilent E4991). The two port S-parameters of the TCV and DEC are measured on wafer-level from DC to 67 GHz. For the measurement, a 67 GHz Agilent PNA E8361A is used. For the calibration, the impedance standard substrate is placed on an auxiliary chuck and a full two port short open load thru (SOLT) calibration is performed. A 200 V Agilent Source Measurement Module 41420A is used to actuate the membrane of the RF-MEMS test vehicles.

Technology Characterization Vehicle (TCV: an RF-MEMS SPST switch)

Microscope images of the TCV before packaging are shown in Fig. 2.7. After the comparison of the C-V curves of the TCV before and after packaging (Fig. 4.9), approximately 35 fF increase in the capacitance values is observed which is correlated with the additional parasitic capacitance between the RF- SL and the Si cap. It is worth to mention that the pull-in voltage is stable and not influenced by the packaging process of the TCVs proving the mechanical stability of the membrane.

The comparison result of the measured S-parameters of a TCV before and after the packaging process is shown in Fig. 4.10. The S-parameter measurements have shown that the loss of the TCV has slightly increased after the packaging. The packaged TCVs have shown an $\sim$0.2 dB increase of the insertion loss in off-state until 30 GHz and a 1 dB decrease of the isolation in the resonance frequency in on-state after packaging. On the other hand, the matching (S_{11}) is still better than 10 dB up to 67 GHz. The reason for the increase of the loss is the capacitive coupling of the RF-signal to the package. It should be noted that all the given results are the not de-embedded results which include the additional loss due to the RF-pads, considering the real use scenario with bond-wires.

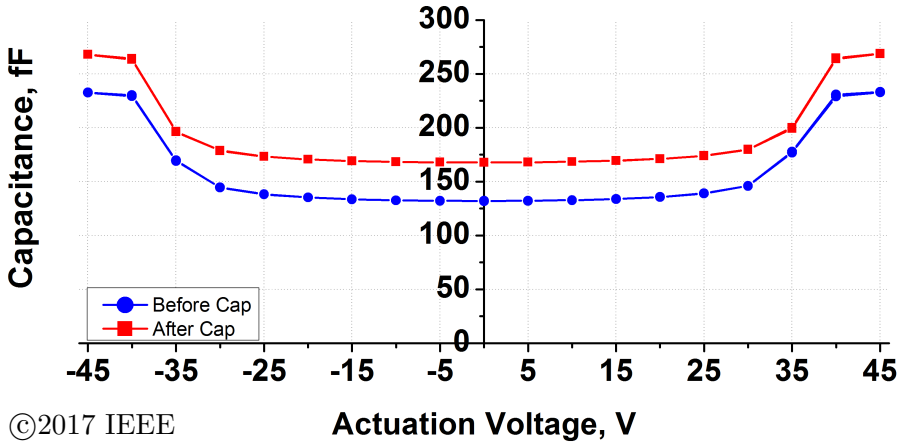

Figure 4.9: The measured C-V graphs of a TCV before (blue) and after (red) the packaging [70, 71].

Dynamic Evaluation Circuit (DEC: an RF-MEMS SPDT switch)

As expected from the TCV, the capacitance values of the DEC show a significant increase after the packaging process (Fig. 4.11). The reason of the ∼300 fF capacitance increase is again the parasitic capacitance between the RF- SL and the Si cap. Microscope image of the DEC before packaging is shown in Fig. 4.12. Since the RIC includes significantly longer RF- SLs compared to the TCV, the coupling to the Si cap is much stronger. The pull-in voltage of the DEC is stable as in the TCV and the mechanical behavior of the membrane is not influenced by the packaging process.

In Fig. 4.13, the comparison results of the measured S-parameter results of a DEC before and after the packaging process are shown. The comparison shows clearly the effect of the package on the measured DEC with an increase of ∼1.5 dB loss in the up-state and a 1.5 dB decrease of isolation in the down-state at 23 GHz.

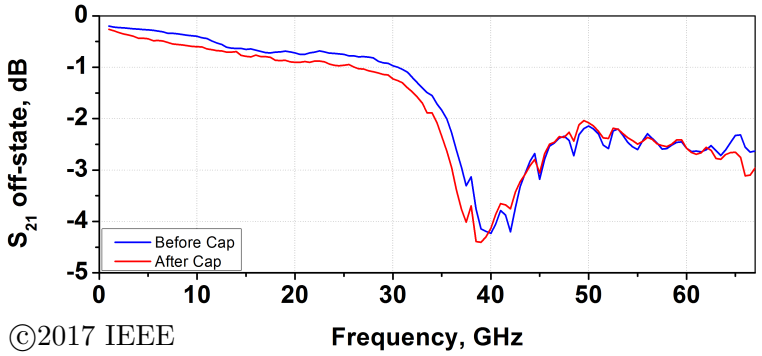

(a)

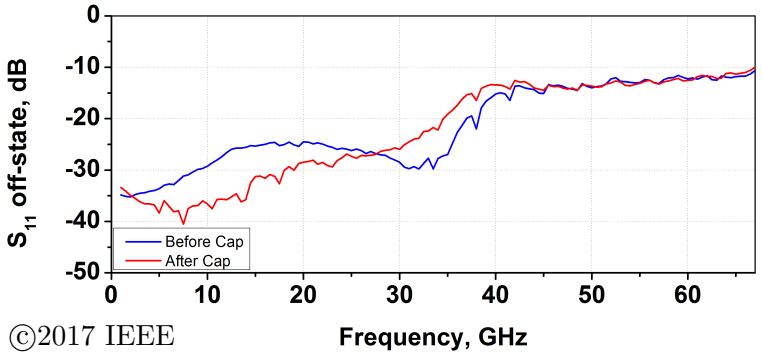

(b)

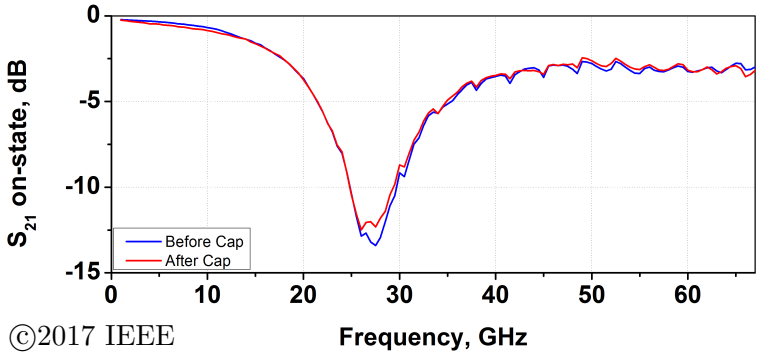

(c)

Figure 4.10: The measured S-parameters of a TCV for both states, before (blue) and after (red) the packaging: (a) S_{21} off-state, (b) S_{11} off-state, (c) S_{21} on-state [71].

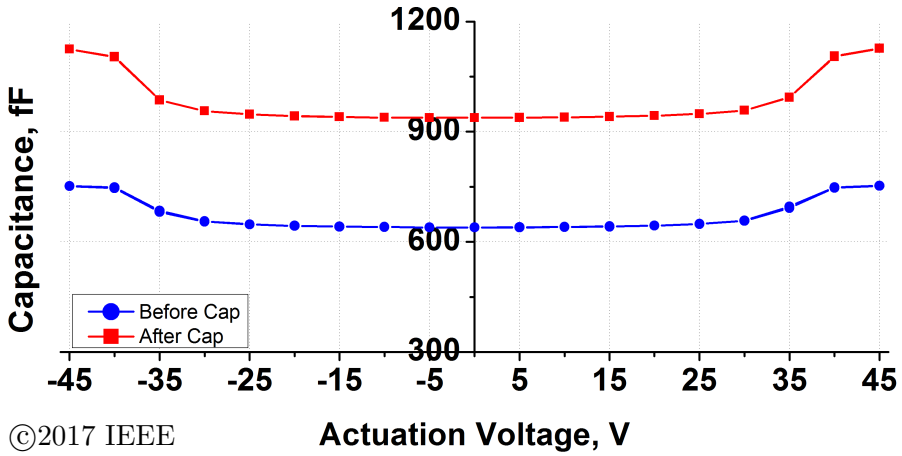

Figure 4.11: The measured C-V graphs of a DEC before (blue) and after (red) the packaging [71].

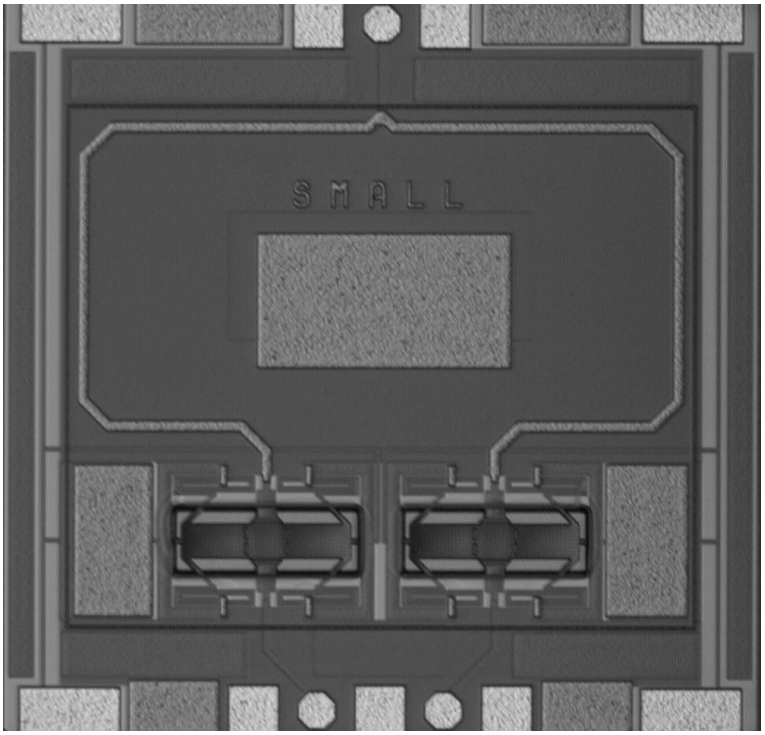

Figure 4.12: Microscope image of a DEC before Si cap packaging.

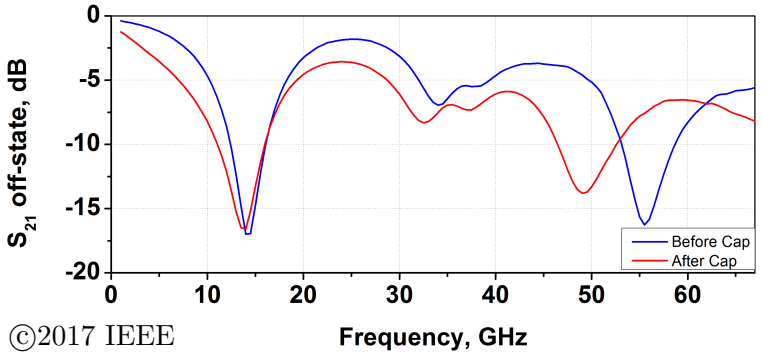

(a)

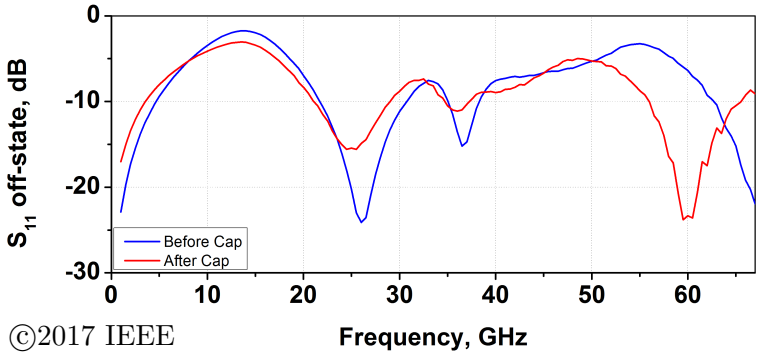

(b)

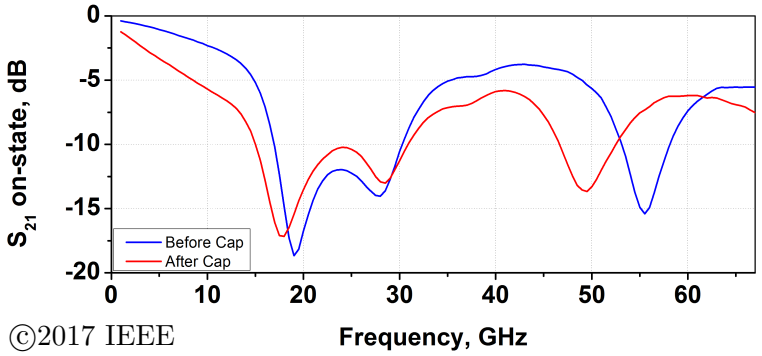

(c)

Figure 4.13: The measured S-parameters of a DEC for both states, before (blue) and after (red) the packaging: (a) S_{21} off-state, (b) S_{11} off-state, (c) S_{21} on-state [71].

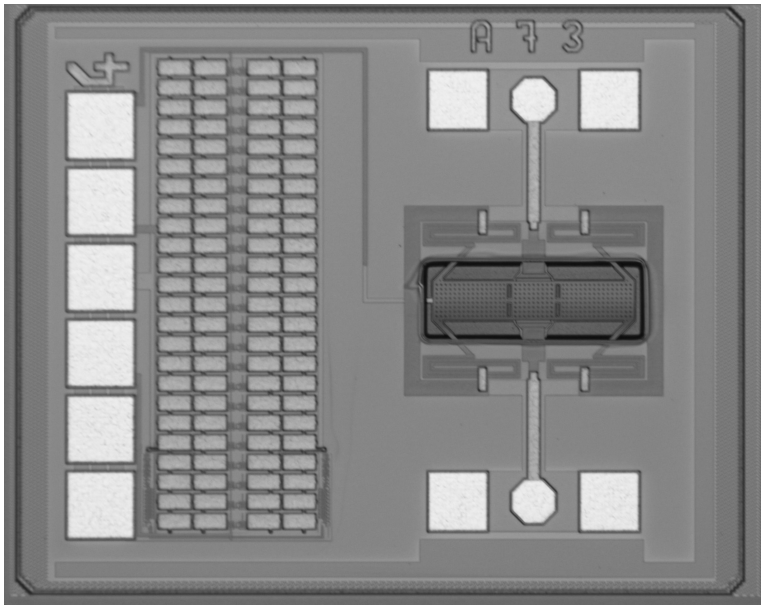

Figure 4.14: Microscope image of a RIC before the Si cap packaging.

Representative Integrated Circuit (RIC: an RF-MEMS SPST switch integrated with an on-chip high-voltage CP)

The RIC includes an RF-MEMS SPST switch integrated with an on-chip high-voltage CP in the 0.25 µm SiGe BiCMOS technology. The necessary actuation voltage for the RICs SPST RF-MEMS switch is generated by the on-chip CP. A CP is designed in IHP's 0.13 µm SiGe BiCMOS technology [94], using stacked BEOL capacitors to overcome the output voltage limitations of charge pumps with standard MIM capacitors.

Microscope image of the RIC including the RF-MEMS SPST switch integrated with the on-chip high-voltage CP is shown in Fig. 4.14, before the Si cap packaging of the RF-MEMS SPST switch. Fig. 4.15 shows the microscope image of the RICs during electrical characterization after the Si cap packaging of the RF-MEMS SPST switch. Electrical characterization of the CP has shown that the necessary high voltage (45 V) for the actuation of the RF-MEMS SPST can be successfully generated on-chip. In order to understand the effect of the control voltage (V_{ctrl}) on the output voltage (V_{out}), V_{ctrl} is swept between 0 to 1.1 V. Fig. 4.16 shows the V_{ctrl} versus V_{out} graph of the CP when the supply voltage (V_{dd}) is fixed at 3 V and input voltage for first CP stage (V_{in}) is fixed at 0 V. It shows that 45 V V_{out} is possible with minimum 1.1 V V_{ctrl}.

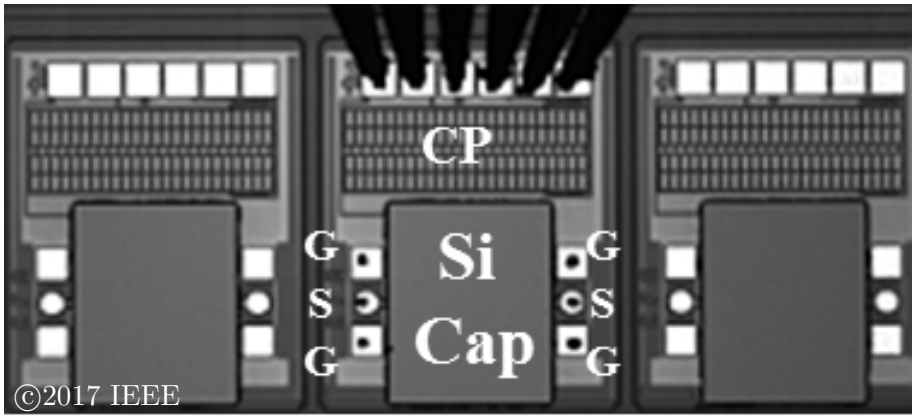

Figure 4.15: The microscope image of the RICs during electrical characterization [71].

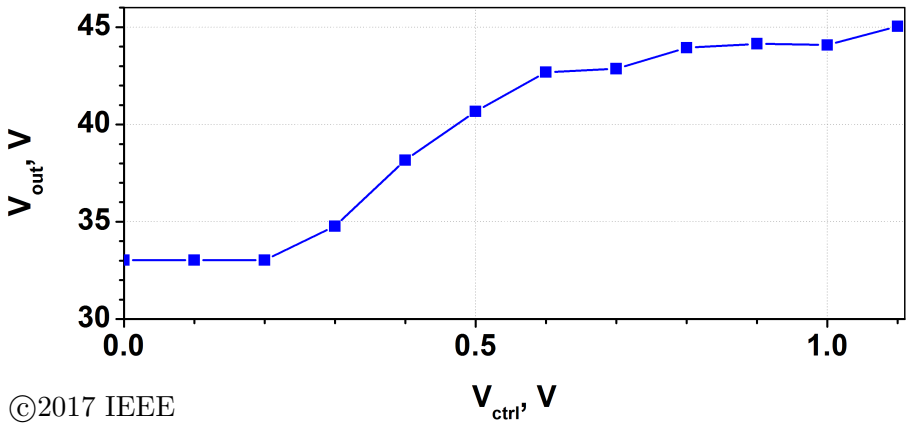

Figure 4.16: V_{ctrl} vs. V_{out} curve of the charge pump with V_{dd} of 3 V and V_{in} of 0 V [71].

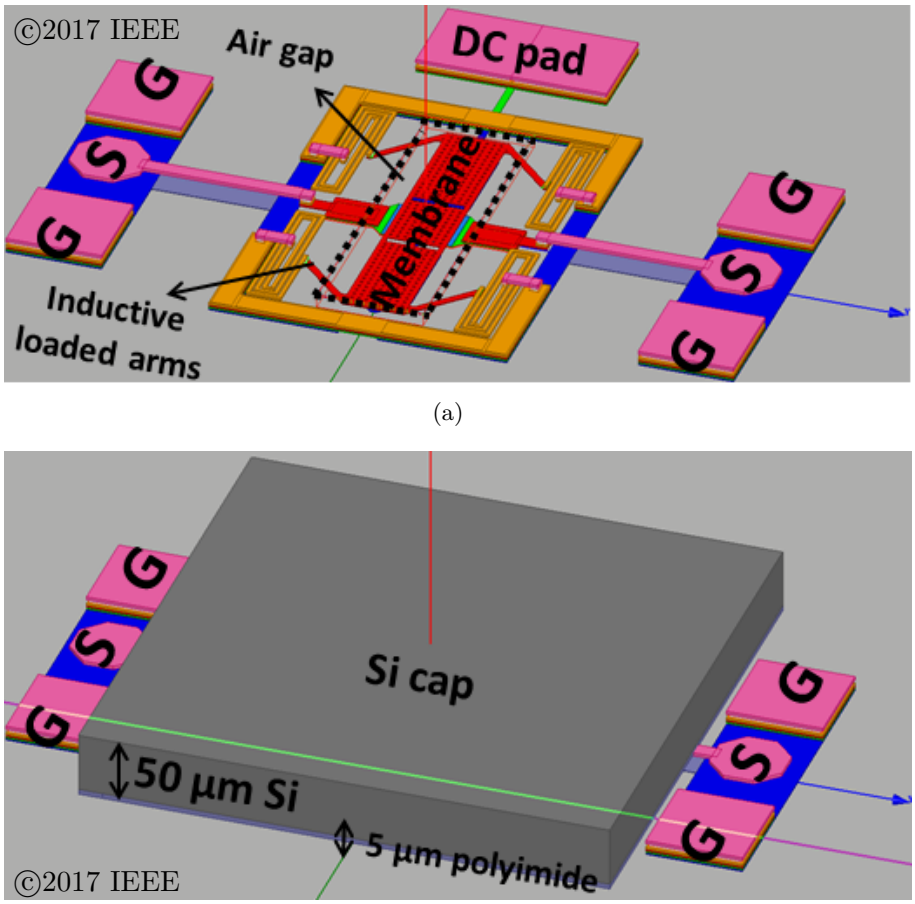

(a)

(b)

Figure 4.17: The 3D EM simulation model of the inductive loaded M3 membrane RF-MEMS switch, (a) without Si cap and (b) with Si cap [70].

4.3.2 Effect of silicon cap packaging

In this section, the effect of Si cap packaging on the SG25 BiCMOS embedded RF-MEMS switch performance is studied [70]. To show the effect of the Si caps on the RF performance of the RF-MEMS switches, two EM models are built up in ANSYS HFSS and shown in Fig. 4.17.

The first model of the RF-MEMS switch is created without the Si cap; instead the second model is created with the Si cap. The model including the Si cap is simulated with a parametric sweep for different Si resistivity values: 10 kΩ·cm (0.01 s/m), 50 Ω·cm (2 s/m) and 1 Ω·cm (100 s/m). Fig. 4.18 shows the EM simulated insertion loss results of the RF-MEMS switch without the Si cap and with the different resisti-

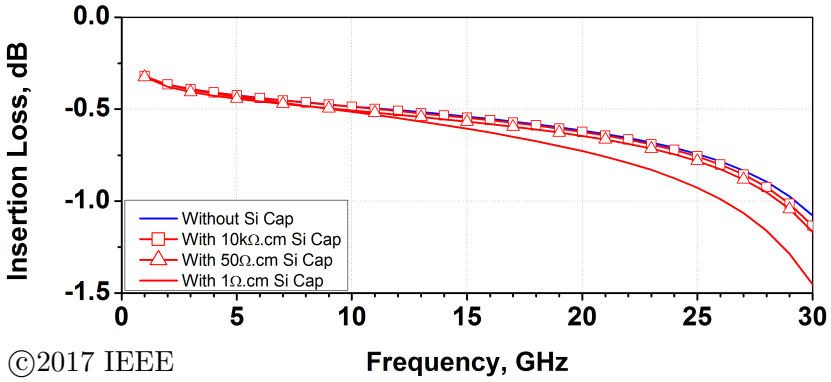

Figure 4.18: The extracted insertion loss results of the EM simulated RF-MEMS switch without Si cap and with Si caps of different resistivity values (10 kΩ·cm, 50 Ω·cm, and 1 Ω·cm) [70].

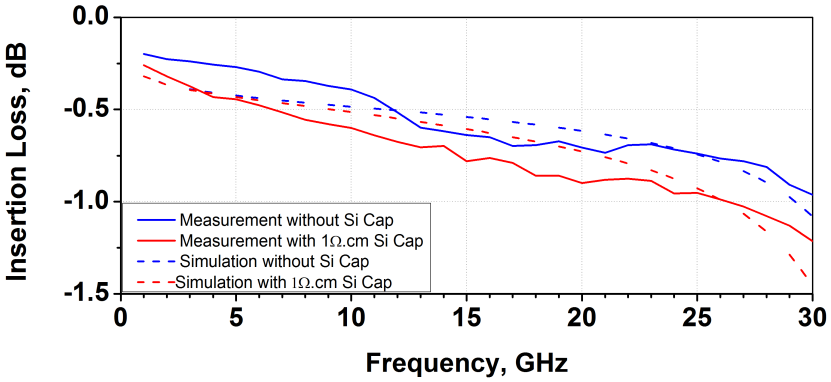

Figure 4.19: The extracted insertion loss comparison of the measured and simulated RF-MEMS switches in off-state without Si cap and with 1 Ω·cm resistivity Si cap.

vity Si caps. The IL curves are similar in case of without the Si cap and with the Si caps of 10 kΩ·cm and 50 Ω·cm resistivity. However, the IL degrades with the usage of a 1 Ω·cm resistivity Si cap.

The insertion loss comparison of the RF-MEMS switch before and after Si cap; and the EM simulations without and with the 1 Ω·cm Si cap shows very good agreement (Fig. 4.19). Indeed, the EM simulations clearly show that the ∼0.2 dB increase of the loss occurs due to the low resistive Si cap (1 Ω·cm). It is worth taking into consideration that the RF performance degradation can be minimized with a medium resistive Si cap (50 Ω·cm) which makes the packaging cost-effective compared to the high resistive Si substrates.

4.3.3 Yield analysis

In recent years, numerous outstanding RF performance results [95–97] have been achieved with RF-MEMS switches. However, the repeatability and the yield of the RF-MEMS processes are still in the main challenges before their commercialization.

With respect to the C-V measurement results of the TCVs and DECs, three different regions are defined on wafer-level to show the process uniformity. The divisions into regions are done with respect to the mechanical functionalities and the pull-in voltages of the test vehicles over the 8-inch wafer. Additionally, the CPoutput voltage of the RIC over an 8-inch wafer is also given.

Technology Characterization Vehicle (TCV: an RF-MEMS SPST switch)

Although 83.5 % of the measured TCVs are functional on wafer-level (Fig. 4.20), the functional TCVs are also divided into two different regions with respect to their pull-in voltages. The TCVs, for the further reliability tests, are selected from the safe operation region because of their higher pull-in voltages (stiffer membrane) [98]. The three wafer regions for the TCVs (Fig. 4.21) are decided as the following: (1) not functional region with less than 230 fF on-state capacitance (C_{on}), (2) the safe operation region between 230 and 320 fF C_{on}, (3) the low pull-in voltage region with more than 320 fF C_{on} at 45 V. The yield of the TCVs is distributed into these three wafer regions as 63.5 % functional from the safe operation region, 20 % functional but with low pull-in voltage and 16.5 % not functional region. The different performances of the TCVs are due to the non-uniform deposition and etching processes over the wafer during their fabrication.

Dynamic Evaluation Circuit (DEC: an RF-MEMS SPDT switch)

The 68 % of the measured DECs are functional on wafer-level (Fig. 4.22). Similar as in the TCV case, the functional DECs are divided into two different regions with respect to their pull-in voltages. The selected DECs, for the further reliability tests, are also taken from the safe operation region with the higher pull-in voltages (stiffer membrane). The three wafer regions for the DECs (Fig. 4.23) are defined as the following: (1) the not functional region with less than 1010 fF C_{on}, (2) the safe operation region between 1010 and 1100 fF C_{on}, (3) the low pull-in voltage region with more than 1100 fF C_{on} at 45 V. The yield of the DECs is distributed into these three wafer regions as 46 % functional from the safe operation region, 22 % functional but with low pull-in voltage and 32 % not functional region.

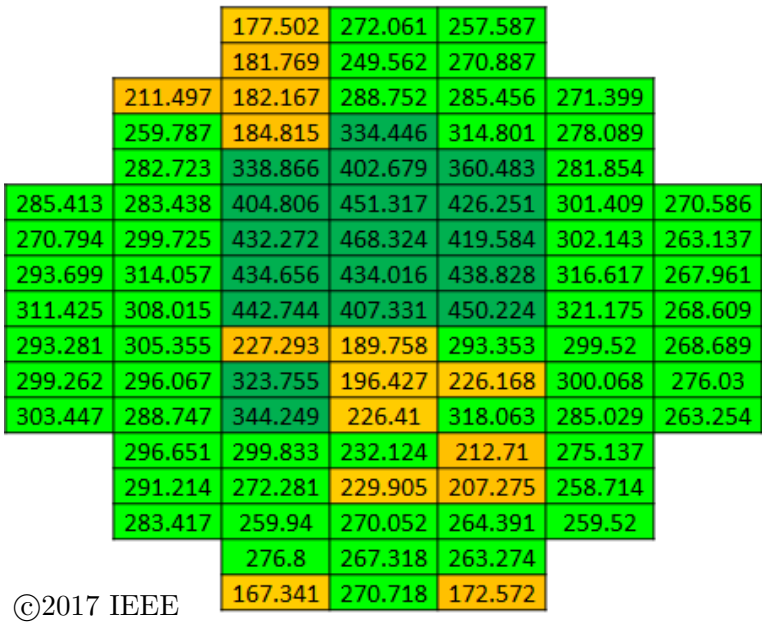

Figure 4.20: The wafer-level C_{on} values of TCVs, showing the yield and uniformity of the BiCMOS MEMS process [71].

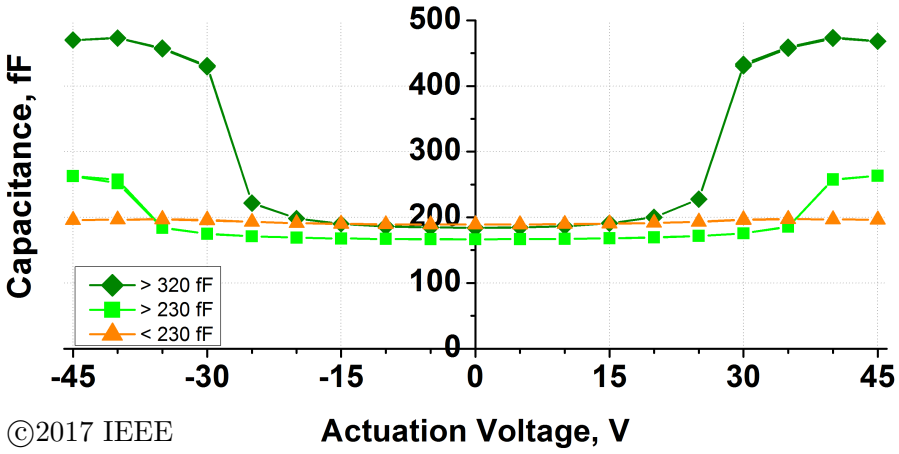

Figure 4.21: The C-V behaviors of the TCVs on different regions of the wafer [71].

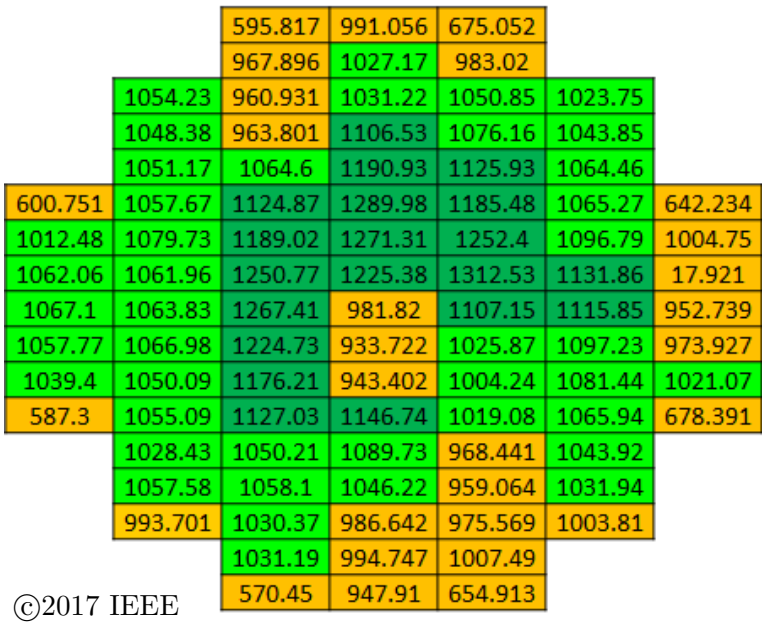

Figure 4.22: The wafer-level C_{on} values of DECs, showing the yield and uniformity of the BiCMOS MEMS process [71].

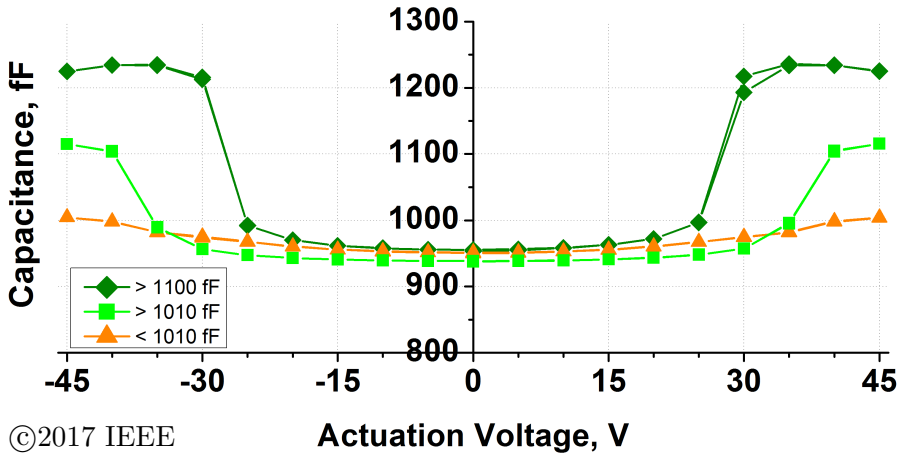

Figure 4.23: The C-V behaviors of the DECs on different regions of the wafer [71].

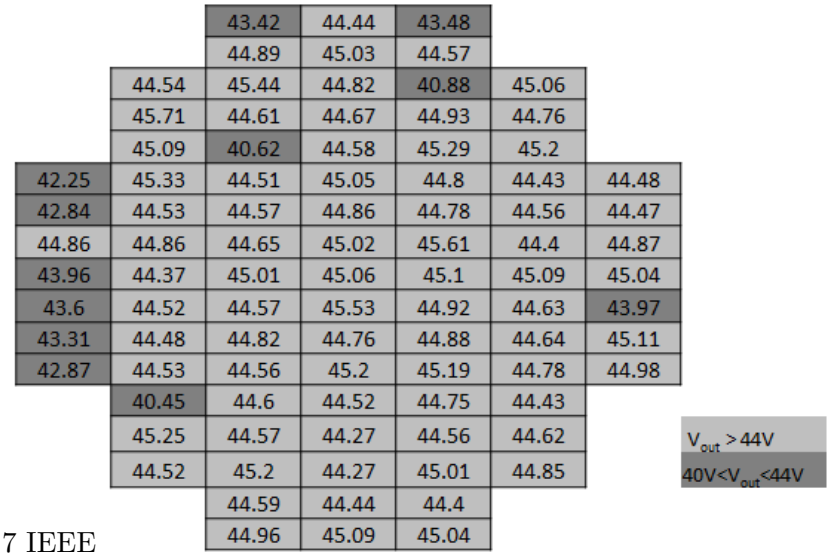

Figure 4.24: The wafer-level measured V_{out} values of RIC's charge pump, showing the yield and uniformity of the BiCMOS process [71].

Charge pump (CP) of the Representative Integrated Circuit (RIC)

The on-wafer yield analysis of the integrated CP V_{out} is performed applying a V_{dd} of 3 V and a V_{ctrl} of 1.1 V. The wafer-level measured V_{out} values are shown in Fig. 4.24. The CPs of the RICs are 100 % functional on wafer-level. The wafer map shows that the 13 % of the chips have generated between 40 V and 44 V V_{out}. The rest of the wafer, 87 % of the chips has generated more than 44 V V_{out} which is sufficient actuation voltage for the RF-MEMS test vehicles.

4.4 Conclusion

Section 4.2 section has presented an RF-MEMS based SPDT switch embedded in IHP's 0.13 µm SiGe BiCMOS process technology. A 140 GHz targeted operating frequency RF-MEMS based SPDT switch, with its measured 1.42 dB insertion loss and 54.5 dB isolation at 140 GHz, has been successfully demonstrated in 110 – 170 GHz frequency band. To the best of my knowledge, the demonstrated SPDT switch is the first RF-MEMS based SPDT switch presented in D-band and provides the lowest insertion loss and the highest isolation values compared to the field-effect transistor (FET) and HBT based SPDTs.

Section 4.3 has presented the performance and yield analyses of packaged RF-MEMS test vehicles; SPST, SPDT and high-voltage CP integrated with SPST switch that are embedded in IHP's 0.25 µm SiGe BiCMOS process technology for space applications at K-Band. Since the S-parameter and C-V measurement results of the SPST and SPDT switches have shown changes after packaging of the test vehicles, the influence of the Si cap packaging is investigated more in detail by extending the EM simulations. As a result of this investigation, the S-parameter measurements and the EM simulations have shown a similar increase of ∼0.2 dB dB for the loss in SPST switch which is introduced by the low resistive Si cap packages, i.e. 1 Ω·cm. To conclude, the presented wafer-level packaging technique has shown a good compromise between low cost and good RF performance for the RF-MEMS switches at K-band.

In Chapter 4, RF-MEMS design examples from both 0.13 µm and 0.25 µm SiGe BiCMOS technologies have been given. In 0.13 µm SiGe BiCMOS technology, a D-band SPST has been firstly developed to be used as the key element during the development of a D-band SPDT switch. Both of the developed switches have shown state-of-the-art RF performances and their EM simulation results have matched very good with the S-parameter measurement results. Later on the design examples of RF-MEMS devices in 0.25 µm SiGe BiCMOS technology have been presented. The presented devices have included K-band RF-MEMS based SPST and SPDT switches and an on-chip CP with an integrated RF-MEMS based SPST switch. The presented switches of the 0.25 µm SiGe BiCMOS technology have shown more than 68 % yield in terms of functionality on 200 mm wafers together with their wafer-to-wafer bonded Si cap packages. The differences in the C-V characteristics between different regions of the wafer can be explained with process variations overall the wafer. With non-uniform deposition and etching processes, membranes of the switches have different initial bending due to stress which causes variations on C_{off},C_{on} and pull-in voltages.

5 Conclusion and Outlook

This chapter summarizes the main challenges, remarks and achievements of this thesis.

5.1 Technology

Monolithical integration of RF-MEMS switches in SiGe BiCMOS technologies has the big advantage of stable and well-controlled fabrication environment. However, this integration also brings challenges during the design and fabrication phase of the devices. More specifically; the devices should use the available metals and the standard metal thicknesses of the BEOL modules, should be full-filling the minimum design rule requirements of the BEOL modules. Additionally, the additional process steps for the fabrication of the devices should not decrease the yield and performance of the standard CMOS devices.

5.2 Modeling of RF-MEMS Switches

For the realization of the high performance mm-wave RF-MEMS switches that are presented in this thesis, it was essential to have accurate electromagnetic models additional to the necessities of well developed process flows and stable process conditions. Therefore, the accurate electromagnetic modeling of mm-wave RF-MEMS switches has been selected as the main focus of this thesis. These accurate EM models made the realization of RF-MEMS switches with state-of-the-art RF performances possible, even up to 320 GHz. The research work done in this thesis has been devoted to the design, electromagnetic modeling and RF optimizations of the mm-wave RF-MEMS switches that are embedded in IHP's BiCMOS technologies.

Packaging of the RF-MEMS devices is not only critical due to the development of an entire process flow but also due to additional RF performances losses that can be caused by the package. The additional loss can become more significant with the increasing operating frequencies. Therefore, the electromagnetic models of mm-wave RF-MEMS devices should include the effect of the packages from the beginning to

foresee the differences in RF performances. Foreseeable effects can be avoided with different packaging strategies or design/process optimizations. An example for avoiding the RF performance loss due to the packaging can be given as the decision of the packaging material. The right selected packaging material would avoid the additional loss in RF performance of the RF-MEMS device, however the cost of the material should be also taken into account before the final decision about the package.

Development of RF-MEMS devices with very good RF performances take years, starting from the process development up to electrical characterization. An accurate model for the EM simulations reduces the final cost and development time of the RF-MEMS devices since the optimizations can be done with the help of the simulators. However, a good match between the simulation and measurement results still takes time until an accurate model is created. Modeling and electrical characterization supplies information to each other as a feedback loop during the optimizations. With the back and forth iterations, an accurate model can be created. The developed feedback methodology can be also used for development of other RF-MEMS devices in the future.

5.3 RF-MEMS Design Examples

The presented wafer-to-wafer Si cap packaging process for the K-band test vehicles has shown successful results in terms of high yield and quality of the bonding process. However, for the Si cap packaging process an additional $\sim$100 µm distance between the pads and the switch is required for the bonding. This distance brings extra cost because of the necessity of a larger area and an additional loss with longer transmission lines. On the other hand, the presented second wafer-level packaging technique, thin film wafer-level encapsulation, has shown more promising results for the future in terms of less number of process steps and lower cost as a result of no additional wafer for bonding and has required no extra distance between the switch and the pads which can cause to additional loss and area.

The necessary voltage for the actuation of the BiCMOS embedded RF-MEMS switches can be provided by on-chip charge pumps [71, 94] with an additional cost due to increased chip area.

The main achievements of this thesis are as follows:

- For the first time, successful demonstration of an RF-MEMS switch in D-band.

  The switch shows maximum isolation of 51.6 dB at 142.8 GHz with the insertion loss of 0.65 dB. With the developed RF-MEMS switch, better than 0.67 dB insertion loss and more than 16 dB isolation in all D-band are achieved.

- For the first time, successful demonstration of an RF-MEMS switch in J-band.

  With the developed RF-MEMS switch, better than 1.22 dB insertion loss and more than 13.24 dB isolation in all J-band are achieved. At 240 GHz, an insertion loss of 0.44 dB and an isolation of 24.6 dB are demonstrated.

- For the first time, successful demonstration of an RF-MEMS based SPDT switch in D-band.

  The demonstrated RF-MEMS SPDT switch shows less than 1.86 dB insertion loss and more than 18.25 dB isolation in all D-band.

- Successful demonstration of high yield RF-MEMS test vehicles with Si cap packaging.

  The presented K-band RF-MEMS test vehicles for space applications show high yield of packaged devices; thus promising for prototyping and volume production.

Despite the state-of-the-art performances of the presented RF-MEMS switches in 0.13 µm SiGe BiCMOS technology, there are additional points that need to be addressed in the near future:

- Yield analysis of the thin-film wafer-level encapsulated RF-MEMS switches has to be done in order to reveal the process related problems that can occur during the wafer-level packaging.

- Investigations on the 0.13 µm SiGe BiCMOS technology RF-MEMS switch reliability have to be performed in order to reveal the failure modes due to the design or process integration.

Bibliography

References

[1] C. L. Goldsmith, Zhimin Yao, S. Eshelman, and D. Denniston. "Performance of low-loss RF MEMS capacitive switches". In: *IEEE Microwave and Guided Wave Letters* 8.8 (Aug. 1998), pp. 269–271. ISSN: 1051-8207. DOI: 10.1109/75.704410.

[2] Y. Q. Zhu, L. Han, L. F. Wang, J. Y. Tang, and Q. A. Huang. "A Novel Three-State RF MEMS Switch for Ultrabroadband (DC-40 GHz) Applications". In: *IEEE Electron Device Letters* 34.8 (Aug. 2013), pp. 1062–1064. ISSN: 0741-3106. DOI: 10.1109/LED.2013.2269993.

[3] A. Dec and K. Suyama. "Micromachined electro-mechanically tunable capacitors and their applications to RF IC's". In: *IEEE Transactions on Microwave Theory and Techniques* 46.12 (Dec. 1998), pp. 2587–2596. ISSN: 0018-9480. DOI: 10.1109/22.739251.

[4] R. Mahameed and G. M. Rebeiz. "Electrostatic RF MEMS tunable capacitors with analog tunability and low temperature sensitivity". In: *2010 IEEE MTT-S International Microwave Symposium*. May 2010, pp. 1254–1257. DOI: 10.1109/MWSYM.2010.5514843.

[5] S. Pinel, F. Cros, S. Nuttinck, S. W. Yoon, M. G. Allen, and J. Laskar. "Very high-Q inductors using RF-MEMS technology for System-On-Package wireless communication integrated module". In: *IEEE MTT-S International Microwave Symposium Digest, 2003*. Vol. 3. June 2003, 1497–1500 vol.3. DOI: 10.1109/MWSYM.2003.1210420.

[6] N. Khalid, J. Singh, H. P. Le, J. Devlin, and Z. Sauli. "A very high Q-factor inductor using MEMS technology". In: *2009 Asia Pacific Conference on Postgraduate Research in Microelectronics Electronics (PrimeAsia)*. Jan. 2009, pp. 77–80. DOI: 10.1109/PRIMEASIA.2009.5397444.

[7] S. S. Li. "CMOS-MEMS resonators and their applications". In: *2013 Joint European Frequency and Time Forum International Frequency Control Symposium (EFTF/IFC)*. July 2013, pp. 915–921. DOI: 10.1109/EFTF-IFC.2013.6702098.

[8] A. Uranga, J. Verd, and N. Barniol. "CMOS-MEMS resonators: From devices to applications". In: *Microelectronic Engineering* 132 (2015). Micro and Nanofabrication Breakthroughs for Electronics, MEMS and Life Sciences, pp. 58–73. ISSN: 0167-9317. DOI: https://doi.org/10.1016/j.mee.2014.08.015.

[9] G.M. Rebeiz. *RF MEMS: Theory, Design, and Technology*. Wiley, 2004. ISBN: 9780471462880.

[10] M. SeyyedEsfahlan, E. Öztürk, M. Kaynak, and I. Tekin. "77-GHz Four-Element Phased-Array Radar Receiver Front End". In: *IEEE Transactions on Components, Packaging and Manufacturing Technology* 6.8 (Aug. 2016), pp. 1162–1173. ISSN: 2156-3950. DOI: 10.1109/TCPMT.2016.2571742.

[11] Project NANOTEC. 2017-08-11. URL: http://project-nanotec.com/.

[12] K. Schmalz, N. Rothbart, P. F. X. Neumaier, J. Borngräber, H. W. Hübers, and D. Kissinger. "Gas Spectroscopy System for Breath Analysis at mm-wave/THz Using SiGe BiCMOS Circuits". In: *IEEE Transactions on Microwave Theory and Techniques* 65.5 (May 2017), pp. 1807–1818. ISSN: 0018-9480. DOI: 10.1109/TMTT.2017.2650915.

[13] B. Heinemann, H. Rücker, R. Barth, F. Bárwolf, J. Drews, G. G. Fischer, A. Fox, O. Fursenko, T. Grabolla, F. Herzel, J. Katzer, J. Korn, A. Krúger, P. Kulse, T. Lenke, M. Lisker, S. Marschmeyer, A. Scheit, D. Schmidt, J. Schmidt, M. A. Schubert, A. Trusch, C. Wipf, and D. Wolansky. "SiGe HBT with fT/fmax of 505 GHz/720 GHz". In: *2016 IEEE International Electron Devices Meeting (IEDM)*. Dec. 2016, pp. 3.1.1–3.1.4. DOI: 10.1109/IEDM.2016.7838335.

[14] G. Q. Zhang. *More than Moore. Creating High Value Micro/Nanoelectronics Systems*. New York Springer, 2009. ISBN: 9780387755922.

[15] M. Kaynak, M. Wietstruck, C. B. Kaynak, A. Göritz, S. Tolunay, and B. Tillack. "MEMS - BiCMOS monolithic integration". In: *2014 XXXIth URSI General Assembly and Scientific Symposium (URSI GASS)*. Aug. 2014, pp. 1–4. DOI: 10.1109/URSIGASS.2014.6929473.

[16] M. Kaynak, M. Wietstruck, C. B. Kaynak, S. Tolunay, A. Göritz, and B. Tillack. "Modular extension of high performance SiGe BiCMOS technologies - Following the More-than-Moore path". In: *2015 Asia-Pacific Microwave Conference (APMC)*. Vol. 1. Dec. 2015, pp. 1–3. DOI: 10.1109/APMC.2015.7411742.

[17] M. Kaynak, M. Wietstruck, A. Göritz, S. Tolunay Wipf, M. Inac, B. Cetindogan, C. Wipf, C. B. Kaynak, M. Wöhrmann, S. Voges, and T. Braun. "0.13 μm SiGe BiCMOS technology with More-than-Moore modules". In: *2017 IEEE Bipolar/BiCMOS Circuits and Technology Meeting (BCTM)*. Oct. 2017, pp. 62–65. DOI: 10.1109/BCTM.2017.8112912.

[18] R. R. Mansour. "RF MEMS-CMOS Device Integration: An Overview of the Potential for RF Researchers". In: *IEEE Microwave Magazine* 14.1 (Jan. 2013), pp. 39–56. ISSN: 1527-3342. DOI: 10.1109/MMM.2012.2226539.

[19] J. Rizk, G.-L. Tan, J. B. Muldavin, and G. M. Rebeiz. "High-isolation W-band MEMS switches". In: *IEEE Microwave and Wireless Components Letters* 11.1 (Jan. 2001), pp. 10–12. ISSN: 1531-1309. DOI: 10.1109/7260.905952.

[20] M. Kaynak, M. Wietstruck, R. Scholz, J. Drews, R. Barth, K.E. Ehwald, A. Fox, U. Haak, D. Knoll, F. Korndorfer, S. Marschmeyer, K. Schulz, C. Wipf, D. Wolansky, B. Tillack, K. Zoschke, T. Fischer, Y.S. Kim, J.S. Kim, W.-G. Lee, and J.W. Kim. "BiCMOS embedded RF-MEMS switch for above 90 GHz applications using backside integration technique". In: *IEEE International Electron Devices Meeting*. Dec. 2010, pp. 36.5.1–36.5.4. DOI: 10.1109/IEDM.2010.5703488.

[21] S. Tolunay Wipf, A. Göritz, C. Wipf, M. Wietstruck, A. Burak, E. Türkmen, Y. Gürbüz, and M. Kaynak. "240 GHz RF-MEMS switch in a 0.13 μm SiGe BiCMOS Technology". In: *2017 IEEE Bipolar/BiCMOS Circuits and Technology Meeting (BCTM)*. Oct. 2017, pp. 54–57. DOI: 10.1109/BCTM.2017.8112910.

[22] M. Kaynak, K. E. Ehwald, J. Drews, R. Scholz, F. Korndörfer, D. Knoll, B. Tillack, R. Barth, M. Birkholz, K. Schulz, Y. M. Sun, D. Wolansky, S. Leidich, S. Kurth, and Y. Gürbüz. "BEOL embedded RF-MEMS switch for mm-wave applications". In: *2009 IEEE International Electron Devices Meeting (IEDM)*. Dec. 2009, pp. 1–4. DOI: 10.1109/IEDM.2009.5424219.

[23] M. Kaynak, F. Korndörfer, M. Wietstruck, D. Knoll, R. Scholz, C. Wipf, C. Krause, and B. Tillack. "Robustness and reliability of BiCMOS embedded RF-MEMS switch". In: *2011 IEEE 11th Topical Meeting on Silicon Monolithic Integrated Circuits in RF Systems*. Jan. 2011, pp. 177–180. DOI: 10.1109/SIRF.2011.5719336.

[24] H. Rücker, B. Heinemann, and A. Fox. "Half-Terahertz SiGe BiCMOS technology". In: *2012 IEEE 12th Topical Meeting on Silicon Monolithic Integrated Circuits in RF Systems*. Jan. 2012, pp. 133–136. DOI: 10.1109/SiRF.2012.6160164.

[25] V. Valenta, H. Schumacher, S. Tolunay Wipf, M. Wietstruck, A. Göritz, M. Kaynak, and W. Winkler. "Single-chip transmit-receive module with a fully integrated differential RF-MEMS antenna switch and a high-voltage generator for F-band radars". In: *IEEE Bipolar/BiCMOS Circuits and Technology Meeting*. Oct. 2015, pp. 40–43. DOI: 10.1109/BCTM.2015.7340564.

[26] T. Chaloun, W. Menzel, F. Tabarani, T. Purtova, H. Schumacher, M. Kaynak, Q. Luo, S. Gao, R. Starec, and V. Ziegler. "Wide-angle scanning active transmit/receive reflectarray". In: *IET Microwaves, Antennas Propagation* 8.11 (Aug. 2014), pp. 811–818. ISSN: 1751-8725. DOI: 10.1049/iet-map.2013.0704.

[27] T. Chaloun, F. Tabarani, S. Tolunay Wipf, M. Kaynak, H. Schumacher, and W. Menzel. "A modular phased array transceiver with RF-MEMS SPDT switches in a 0.25 μm SiGe BiCMOS technology". In: *12th European Conference on Antennas and Propagation (EuCAP 2018)*. Apr. 2018, pp. 1–5. DOI: 10.1049/cp.2018.0615.

[28] H.A.C. Tilmans, J. De Coster, P. Helin, V. Cherman, A. Jourdain, P. De Moor, B. Vandevelde, N.P. Pham, J. Zekry, A. Witvrouw, and I. De Wolf. "MEMS packaging and reliability: An undividable couple". In: *Microelectronics Reliability* 52.9 (2012). Special issue 23rd European Symposium on the reliability of electron devices, failure pyhsics and analysis, pp. 2228–2234. ISSN: 0026-2714. DOI: https://doi.org/10.1016/j.microrel.2012.06.029.

[29] G. M. Rebeiz and J. B. Muldavin. "RF MEMS switches and switch circuits". In: *IEEE Microwave Magazine* 2.4 (Dec. 2001), pp. 59–71. ISSN: 1527-3342. DOI: 10.1109/6668.969936.

[30] S. Fouladi and R. R. Mansour. "Capacitive RF MEMS Switches Fabricated in Standard 0.35 μm CMOS Technology". In: *IEEE Transactions on Microwave Theory and Techniques* 58.2 (Feb. 2010), pp. 478–486. ISSN: 0018-9480. DOI: 10.1109/TMTT.2009.2038446.

[31] Y. Feng and N. S. Barker. "Electrostatic RF MEMS switch working on 500-750 GHz". In: *2016 IEEE 17th Annual Wireless and Microwave Technology Conference (WAMICON)*. Apr. 2016, pp. 1–5. DOI: 10.1109/WAMICON.2016.7483849.

[32] H.C. Lee, J.Y. Park, and J.U. Bu. "Piezoelectrically actuated RF MEMS DC contact switches with low voltage operation". In: *IEEE Microwave and Wireless Components Letters* 15.4 (Apr. 2005), pp. 202–204. ISSN: 1531-1309. DOI: 10.1109/LMWC.2005.845689.

[33] R. G. Polcawich, D. Judy, J. S. Pulskamp, S. Trolier-McKinstry, and M. Dubey. "Advances in Piezoelectrically Actuated RF MEMS Switches and Phase Shifters". In: *2007 IEEE/MTT-S International Microwave Symposium*. June 2007, pp. 2083–2086. DOI: 10.1109/MWSYM.2007.380297.

[34] D. J. Chung, R. G. Polcawich, D. Judy, J. Pulskamp, and J. Papapolymerou. "A SP2T and a SP4T switch using low loss piezoelectric MEMS". In: *2008 IEEE MTT-S International Microwave Symposium Digest*. June 2008, pp. 21–24. DOI: 10.1109/MWSYM.2008.4633093.

[35] D. Girbau, L. Pradell, A. Lazaro, and A. Nebot. "Electrothermally Actuated RF MEMS Switches Suspended on a Low-Resistivity Substrate". In: *Journal of Microelectromechanical Systems* 16.5 (Oct. 2007), pp. 1061–1070. ISSN: 1057-7157. DOI: 10.1109/JMEMS.2007.904744.

[36] M. Bakri-Kassem and R. R. Mansour. "High Power Latching RF MEMS Switches". In: *IEEE Transactions on Microwave Theory and Techniques* 63.1 (Jan. 2015), pp. 222–232. ISSN: 0018-9480. DOI: 10.1109/TMTT.2014.2376932.

[37] Y. Zhang, G. Ding, X. Shun, X. Li, and B. Cai. "Design and analysis of the micromechanical structure for an electromagnetic bistable RF MEMS switch". In: *2005 Asia Pacific Microwave Conference Proceedings*. Vol. 1. Dec. 2005, pp. 4–. DOI: 10.1109/APMC.2005.1606197.

[38] S. Lucyszyn. *Advanced RF MEMS*. 1st ed. New York, NY, USA: Cambridge University Press, 2010. ISBN: 9780521897716.

[39] J. Iannacci. "RF-MEMS: an enabling technology for modern wireless systems bearing a market potential still not fully displayed". In: *Microsystem Technologies* 21.10 (Oct. 2015), pp. 2039–2052. ISSN: 1432-1858. DOI: 10.1007/s00542-015-2665-6.

[40] J. Bouchaud and H. Wicht. "RF MEMS: status of the industry and roadmaps". In: *2005 IEEE Radio Frequency integrated Circuits (RFIC) Symposium - Digest of Papers*. June 2005, pp. 379–384. DOI: 10.1109/RFIC.2005.1489818.

[41] J. Bouchaud and B. Knoblich. *RF MEMS switches deliver on early promise*. 2018-07-18. 2007. URL: http://www.memsjournal.com/2007/10/rf-mems-switche.html.

[42] MEMS Journal. *Cell phone antenna troubles RF MEMS come to the rescue*. 2018-07-18. 2010. URL: http://www.memsjournal.com/2010/09/cell-phone-antenna-troubles-rf-mems-come-to-the-rescue.html.

[43] D. McGrath. *Teardown finds RF MEMS in Samsung handset*. 2018-07-18. 2012. URL: https://www.eetimes.com/document.asp?doc_id=1260917.

[44] J.J. DeLisle. *The Future Of Connectivity: Mobile & Automobiles*. 2018-07-18. 2014. URL: http://www.mwrf.com/systems/future-connectivity-mobile-automobiles.

[45] Gartner. *Gartner Hype Cycle*. 2018-03-02. URL: http://www.gartner.com/technology/research/methodologies/hype-cycle.jsp.

[46] J. Iannacci. "Surfing the hype curve of RF-MEMS passive components: towards the 5th generation (5G) of mobile networks". In: *Microsystem Technologies* (Jan. 2018). ISSN: 1432-1858. DOI: 10.1007/s00542-018-3718-4.

[47] R. Allan. *RF MEMS Switches Are Primed For Mass-Market Applications*. 2018-04-18. 2013. URL: http://www.mwrf.com/active-components/rf-mems-switches-are-primed-mass-market-applications.

[48] Cavendish Kinetics. 2018-03-19. URL: http://www.cavendish-kinetics.com.

[49] J. R. De Luis, A. Morris, Q. Gu, and F. de Flaviis. "Tunable Duplexing Antenna System for Wireless Transceivers". In: *IEEE Transactions on Antennas and Propagation* 60.11 (Nov. 2012), pp. 5484–5487. ISSN: 0018-926X. DOI: 10.1109/TAP.2012.2207869.

[50] J. Iannacci. "RF-MEMS technology: An enabling solution in the transition from 4G-LTE to 5G mobile applications". In: *2017 IEEE SENSORS*. Oct. 2017, pp. 1–3. DOI: 10.1109/ICSENS.2017.8234190.

[51] Y. K. Park and Y. Sung. "A Reconfigurable Antenna for Quad-Band Mobile Handset Applications". In: *IEEE Transactions on Antennas and Propagation* 60.6 (June 2012), pp. 3003–3006. ISSN: 0018-926X.

[52] N. Behdad and K. Sarabandi. "A varactor-tuned dual-band slot antenna". In: *IEEE Transactions on Antennas and Propagation* 54.2 (Feb. 2006), pp. 401–408. ISSN: 0018-926X. DOI: 10.1109/TAP.2005.863373.

[53] V. A. Nguyen, R. A. Bhatti, and S. O. Park. "A Simple PIFA-Based Tunable Internal Antenna for Personal Communication Handsets". In: *IEEE Antennas and Wireless Propagation Letters* 7 (2008), pp. 130–133. ISSN: 1536-1225. DOI: 10.1109/LAWP.2008.921332.

[54] K. R. Boyle and P. G. Steeneken. "A Five-Band Reconfigurable PIFA for Mobile Phones". In: *IEEE Transactions on Antennas and Propagation* 55.11 (Nov. 2007), pp. 3300–3309. ISSN: 0018-926X. DOI: 10.1109/TAP.2007.908822.

[55] P. Bahramzy, O. Jagielski, S. Svendsen, and G. F. Pedersen. "Compact Agile Antenna Concept Utilizing Reconfigurable Front End for Wireless Communications". In: *IEEE Transactions on Antennas and Propagation* 62.9 (Sept. 2014), pp. 4554–4563. ISSN: 0018-926X. DOI: 10.1109/TAP.2014.2325946.

[56] P. Bahramzy, O. Jagielski, S. Svendsen, and G. F. Pedersen. "Self-matched high-Q reconfigurable antenna concept for mobile terminals". In: *IET Science, Measurement Technology* 8.6 (2014), pp. 479–486. ISSN: 1751-8822.

[57] P. Bahramzy, O. Jagielski, S. Svendsen, P. Olesen, and G. F. Pedersen. "Aspects of High-Q Tunable Antennas and Their Deployment for 4G Mobile Communications [Antenna Applications Corner]". In: *IEEE Antennas and Propagation Magazine* 58.4 (Aug. 2016), pp. 70–81. ISSN: 1045-9243. DOI: 10.1109/MAP.2016.2569434.

[58] WiSpry. 2018-07-16. URL: http://wispry.com/.

[59] IHS. *IHS iSuppli Teardown Analysis Service Identifies First Use of RF MEMS Part, Set to be Next Big Thing in Cellphone Radios*. 2018-03-19. URL: http://news.ihsmarkit.com/press-release/design-supply-chain/ihs-isuppli-teardown-analysis-service-identifies-first-use-rf-mems.

[60] A. S. Morris, S. P. Natarajan, Q. Gu, and V. Steel. "Impedance tuners for handsets utilizing high-volume RF-MEMS". In: *2012 42nd European Microwave Conference*. Oct. 2012, pp. 193–196. DOI: 10.23919/EuMC.2012.6459116.

[61] Cavendish Kinetics. *News Releases*. 2018-03-19. URL: http://www.cavendish-kinetics.com/news/news-releases/.

[62] J. Morra. *For Tuning Antennas and Switching Signals, RF MEMS Make Their Mark*. 2018-21-03. 2017. URL: http://www.mwrf.com/analog-semiconductors/tuning-antennas-and-switching-signals-rf-mems-make-their-mark.

[63] Analog Devices. 2018-03-21. URL: http://www.analog.com/en/index.html.

[64] E. Carty, P. Fitzgerald, and P. McDaid. *The Fundamentals of Analog Devices' Revolutionary MEMS Switch Technology*. 2018-03-21. URL: http://www.analog.com/en/technical-articles/fundamentals-adi-revolutionary-mems-switch-technology.html.

[65] M. Kaynak, M. Wietstruck, W. Zhang, J. Drews, R. Scholz, D. Knoll, F. Korndörfer, C. Wipf, K. Schulz, M. Elkhouly, K. Kaletta, M. V. Suchodoletz, K. Zoschke, M. Wilke, O. Ehrmann, V. Mühlhaus, G. Liu, T. Purtova, A. C. Ulusoy, H. Schumacher, and B. Tillack. "RF-MEMS switch module in a 0.25 μm BiCMOS technology". In: *IEEE Topical Meeting on Silicon Monolithic Integrated Circuits in RF Systems*. Jan. 2012, pp. 25–28. DOI: 10.1109/SiRF.2012.6160150.

[66] S. Tolunay Wipf, A. Göritz, M. Wietstruck, C. Wipf, and M. Kaynak. "BiCMOS Embedded RF-MEMS Technologies". In: *MikroSystemTechnik 2017; Congress*. Oct. 2017, pp. 1–3.

[67] IHP. *Low-Volume & Multi-Project Service*. 2018-04-09. URL: https://www.ihp-microelectronics.com/en/services/mpw-prototyping/sigec-bicmos-technologies.html.

[68] IHP. *SG25H3 Process Specifications Document*. IHP, Frankfurt Oder, 2018.

[69] K. Zoschke, M. Wilke, M. Wegner, K. Kaletta, C. A. Manier, H. Oppermann, M. Wietstruck, B. Tillack, M. Kaynak, and K. D. Lang. "Capping technologies for wafer level MEMS packaging based on permanent and temporary wafer bonding". In: *2014 IEEE 64th Electronic Components and Technology Conference (ECTC)*. May 2014, pp. 1204–1211. DOI: 10.1109/ECTC.2014.6897444.

[70] S. Tolunay Wipf, A. Göritz, M. Wietstruck, M. Cirillo, C. Wipf, K. Zoschke, and M. Kaynak. "Effect of wafer-level silicon cap packaging on BiCMOS embedded RF-MEMS switch performance". In: *2017 IMAPS Nordic Conference on Microelectronics Packaging (NordPac)*. June 2017, pp. 31–34. DOI: 10.1109/NORDPAC.2017.7993158.

[71] S. Tolunay Wipf, A. Göritz, M. Wietstruck, M. Cirillo, C. Wipf, W. Winkler, and M. Kaynak. "Packaged BiCMOS embedded RF-MEMS test vehicles for space applications". In: *2017 47th European Microwave Conference (EuMC)*. Oct. 2017, pp. 320–323. DOI: 10.23919/EuMC.2017.8230859.

[72] IHP. *SG25G2/S Process Specifications Document*. IHP, Frankfurt Oder, 2018.

[73] A. Morris and S. Cunningham. "Challenges and Solutions for Cost-effective RF-MEMS Packaging". In: *2007 32nd IEEE/CPMT International Electronic Manufacturing Technology Symposium*. Oct. 2007, pp. 278–285. DOI: 10.1109/IEMT.2007.4417077.

[74] R. N. Candler, W.-T. Park, H. Li, G. Yama, A. Partridge, M. Lutz, and T. W. Kenny. "Single wafer encapsulation of MEMS devices". In: *IEEE Transactions on Advanced Packaging* 26.3 (Aug. 2003), pp. 227–232. ISSN: 1521-3323. DOI: 10.1109/TADVP.2003.818062.

[75] K. D. Leedy, R. E. Strawser, R. Cortez, and J. L. Ebel. "Thin-Film Encapsulated RF MEMS Switches". In: *Journal of Microelectromechanical Systems* 16.2 (Apr. 2007), pp. 304–309. ISSN: 1057-7157. DOI: 10.1109/JMEMS.2007.892915.

[76] F. Barriere, A. Crunteanu, A. Bessaudou, A. Pothier, F. Cosset, D. Mardivirin, and P. Blondy. "Zero level metal thin film package for RF MEMS". In: *2010 Topical Meeting on Silicon Monolithic Integrated Circuits in RF Systems (SiRF)*. Jan. 2010, pp. 148–151. DOI: 10.1109/SMIC.2010.5422957.

[77] R. Gaddi, R. Van Kampen, A. Unamuno, V. Joshi, D. Lacey, M. Renault, C. Smith, R. Knipe, and D. Yost. "MEMS technology integrated in the CMOS back end". In: *Microelectronics Reliability* 50.9 (2010). 21^{st} European Symposium on the Reliability of Electron Devices, Failure Physics and Analysis, pp. 1593–1598. ISSN: 0026-2714. DOI: http://dx.doi.org/10.1016/j.microrel.2010.07.113.

[78] S. P. Natarajan, S. J. Cunningham, A. S. Morris, and D. R. Dereus. "CMOS integrated digital RF MEMS capacitors". In: *2011 IEEE 11^{th} Topical Meeting on Silicon Monolithic Integrated Circuits in RF Systems*. Jan. 2011, pp. 173–176. DOI: 10.1109/SIRF.2011.5719327.

[79] S. Tolunay Wipf, A. Göritz, M. Wietstruck, C. Wipf, B. Tillack, A. Mai, and M. Kaynak. "Thin film wafer level encapsulated RF-MEMS switch for D-band applications". In: *2016 46^{th} European Microwave Conference (EuMC)*. Oct. 2016, pp. 1381–1384. DOI: 10.1109/EuMC.2016.7824610.

[80] S. Tolunay Wipf, A. Göritz, M. Wietstruck, C. Wipf, B. Tillack, A. Mai, and M. Kaynak. "Electromagnetic and small-signal modeling of an encapsulated RF-MEMS switch for D-band applications". In: *International Journal of Microwave and Wireless Technologies* 9.6 (2017), pp. 1271–1278. DOI: 10.1017/S1759078717000137.

[81] W. Zhang, M. Kaynak, M. Wietstruck, V. Mühlhaus, and B. Tillack. "EM and lumped-element model of BiCMOS embedded capacitive RF-MEMS switch". In: *2012 The 7^{th} German Microwave Conference*. Mar. 2012, pp. 1–4.

[82] S. Tolunay, M. Wietstruck, A. Göritz, M. Kaynak, and B. Tillack. "Accurate 3D EM modeling of 140 GHz BiCMOS embedded RF-MEMS switch". In: *14^{th} Symposium on RF-MEMS and RF-Microsystems (MEMSWAVE)*. 2013.

[83] M. Kaynak, M. Wietstruck, W. Zhang, J. Drews, R. Barth, D. Knoll, F. Korndörfer, R. Scholz, K. Schulz, C. Wipf, B. Tillack, K. Kaletta, M. v. Suchodoletz, K. Zoschke, M. Wilke, O. Ehrmann, A. C. Ulusoy, T. Purtova, G. Liu, and H. Schumacher. "Packaged BiCMOS embedded RF-MEMS switches with integrated inductive loads". In: *2012 IEEE/MTT-S International Microwave Symposium Digest*. June 2012, pp. 1–3. DOI: 10.1109/MWSYM.2012.6259417.

[84] N. Torres Matabosch, F. Coccetti, M. Kaynak, W. Zhang, B. Tillack, R. Plana, and J. L. Cazaux. "An accurate and versatile equivalent circuit model for RF-MEMS circuit optimization in BiCMOS technology". In: *2012 7^{th} European Microwave Integrated Circuit Conference*. Oct. 2012, pp. 143–146.

[85] Polytec. 2018-05-08. URL: https://www.polytec.com/us/vibrometry/products/microscope-based-vibrometers/msa-500-micro-system-analyzer/.

[86] S. Tolunay Wipf, A. Göritz, M. Wietstruck, C. Wipf, B. Tillack, and M. Kaynak. "D-Band RF-MEMS SPDT Switch in a 0.13 μm SiGe BiCMOS Technology". In: *IEEE Microwave and Wireless Components Letters* 26.12 (Dec. 2016), pp. 1002–1004. ISSN: 1531-1309. DOI: 10.1109/LMWC.2016.2623245.

[87] C. Nguyen. *Radio-Frequency Integrated-Circuit Engineering*. Wiley Series in Microwave and Optical Engineering. Wiley, 2015. ISBN: 9781118936481.

[88] M. Uzunkol and G. M. Rebeiz. "140-220 GHz SPST and SPDT Switches in 45 nm CMOS SOI". In: *IEEE Microwave and Wireless Components Letters* 22.8 (Aug. 2012), pp. 412–414. ISSN: 1531-1309. DOI: 10.1109/LMWC.2012.2206017.

[89] Y. Kim, H. Lee, and S. Jeon. "A 220 - 320 GHz single-pole single-throw switch". In: *2016 IEEE International Symposium on Radio-Frequency Integration Technology (RFIT)*. Aug. 2016, pp. 1–3. DOI: 10.1109/RFIT.2016.7578184.

[90] J. W. May and G. M. Rebeiz. "Design and Characterization of W-Band SiGe RFICs for Passive Millimeter-Wave Imaging". In: *IEEE Transactions on Microwave Theory and Techniques* 58.5 (May 2010), pp. 1420–1430. ISSN: 0018-9480. DOI: 10.1109/TMTT.2010.2042857.

[91] A. Strodl, S. Tolunay, V. Valenta, M. Kaynak, S. Reyaz, R. Johnson, W. Winkler, R. Malmqvist, and H. Schumacher. "RF-MEMS Switched W-Band mm-Wave Passive Imaging System in a 0.13 μm SiGe BiCMOS Technology". In: *16th Symposium on RF-MEMS and RF-Microsystems (MEMSWAVE)*. 2015.

[92] A. C. Ulusoy, P. Song, R. L. Schmid, W. T. Khan, M. Kaynak, B. Tillack, J. Papapolymerou, and J. D. Cressler. "A Low-Loss and High Isolation D-Band SPDT Switch Utilizing Deep-Saturated SiGe HBTs". In: *IEEE Microwave and Wireless Components Letters* 24.6 (June 2014), pp. 400–402. ISSN: 1531-1309. DOI: 10.1109/LMWC.2014.2313529.

[93] W. T. Khan, A. C. Ulusoy, R. Schmid, T. Chi, J. D. Cressler, H. Wang, and J. Papapolymerou. "A D-band (110 to 170 GHz) SPDT switch in 32 nm CMOS SOI". In: *2015 IEEE MTT-S International Microwave Symposium*. May 2015, pp. 1–3. DOI: 10.1109/MWSYM.2015.7167061.

[94] M. Wietstruck, W. Winkler, A. Göritz, S. Tolunay Wipf, C. Wipf, D. Schmidt, A. Mai, and M. Kaynak. "0.13 μm BiCMOS embedded On-Chip High-Voltage Charge Pump with Stacked BEOL Capacitors for RF-MEMS Applications". In: *17th Symposium on RF-MEMS and RF-Microsystems (MEMSWAVE)*. 2016.

[95] J. B. Muldavin and G. M. Rebeiz. "High-isolation CPW MEMS shunt switches. 1. Modeling". In: *IEEE Transactions on Microwave Theory and Techniques* 48.6 (June 2000), pp. 1045–1052. ISSN: 0018-9480. DOI: 10.1109/22.904743.

[96] Hyun-Ho Yang, A. Yahiaoui, H. Zareie, P. Blondy, and G. M. Rebeiz. "A compact high-isolation DC-50 GHz SP4T RF MEMS switch". In: *2014 IEEE MTT-S International Microwave Symposium (IMS2014)*. June 2014, pp. 1–4. DOI: 10.1109/MWSYM.2014.6848359.

[97] C. Chu, X. Liao, and H. Yan. "Ka-band RF MEMS capacitive switch with low loss, high isolation, long-term reliability and high power handling based on GaAs MMIC technology". In: *IET Microwaves, Antennas Propagation* 11.6 (2017), pp. 942–948. ISSN: 1751-8725. DOI: 10.1049/iet-map.2016.0595.

[98] N. Torres Matabosch, F. Coccetti, M. Kaynak, B., B. Tillack, and J.L. Cazaux. "Equivalent circuit model of reliable RF-MEMS switches for component synthesis, fabrication process characterization and failure analysis". In: *International Journal of Microwave and Wireless Technologies* 6.1 (Feb. 2014), pp. 73–81. DOI: 10.1017/S1759078713000871.

Publications

1. S. Tolunay Wipf, A. Göritz, M. Wietstruck, C. Wipf, and M. Kaynak. "BiCMOS Embedded RF-MEMS Technologies". In: *MikroSystemTechnik 2017; Congress.* Oct. 2017, pp. 1–3.

2. S. Tolunay Wipf, A. Göritz, C. Wipf, M. Wietstruck, A. Burak, E. Türkmen, Y. Gürbüz, and M. Kaynak. "240 GHz RF-MEMS switch in a 0.13 μm SiGe BiCMOS Technology". In: *2017 IEEE Bipolar/BiCMOS Circuits and Technology Meeting (BCTM).* Oct. 2017, pp. 54–57. DOI: 10.1109/BCTM.2017.8112910.

3. S. Tolunay Wipf, A. Göritz, M. Wietstruck, M. Cirillo, C. Wipf, W. Winkler, and M. Kaynak. "Packaged BiCMOS embedded RF-MEMS test vehicles for space applications". In: *2017 47th European Microwave Conference (EuMC).* Oct. 2017, pp. 320–323. DOI: 10.23919/EuMC.2017.8230859.

4. S. Tolunay Wipf, A. Göritz, M. Wietstruck, M. Cirillo, C. Wipf, K. Zoschke, and M. Kaynak. "Effect of wafer-level silicon cap packaging on BiCMOS embedded RF-MEMS switch performance". In: *2017 IMAPS Nordic Conference on Microelectronics Packaging (NordPac).* June 2017, pp. 31–34. DOI: 10.1109/NORDPAC.2017.7993158.

5. S. Tolunay Wipf, A. Göritz, M. Wietstruck, C. Wipf, B. Tillack, A. Mai, and M. Kaynak. "Electromagnetic and small-signal modeling of an encapsulated RF-MEMS switch for D-band applications". In: *International Journal of Microwave and Wireless Technologies* 9.6 (2017), pp. 1271–1278. DOI: 10.1017/S1759078717000137.

6. S. Tolunay Wipf, A. Göritz, M. Wietstruck, C. Wipf, B. Tillack, and M. Kaynak. "D-Band RF-MEMS SPDT Switch in a 0.13 μm SiGe BiCMOS Technology". In: *IEEE Microwave and Wireless Components Letters* 26.12 (Dec. 2016), pp. 1002–1004. ISSN: 1531-1309. DOI: 10.1109/LMWC.2016.2623245.

7. S. Tolunay Wipf, A. Göritz, M. Wietstruck, C. Wipf, B. Tillack, A. Mai, and M. Kaynak. "Thin film wafer level encapsulated RF-MEMS switch for D-band applications". In: *2016 46th European Microwave Conference (EuMC).* Oct. 2016, pp. 1381–1384. DOI: 10.1109/EuMC.2016.7824610.

8. S. Tolunay Wipf, A. Göritz, M. Wietstruck, C. Wipf, and M. Kaynak. "RF Pad Optimization for a 140 GHz RF-MEMS Switch". In: *17th Symposium on RF-MEMS and RF-Microsystems (MEMSWAVE).* 2016.

9. S. Tolunay, A. Göritz, M. Wietstruck, C. Wipf, B. Tillack, and M. Kaynak. "94 GHz RF-MEMS SPDT Switch in a 0.13 μm SiGe BiCMOS Technology". In: *16th Symposium on RF-MEMS and RF-Microsystems (MEMSWAVE)*. 2015.

10. S. Tolunay, M. Wietstruck, A. Göritz, M. Kaynak, and B. Tillack. "Accurate 3D EM modeling of 140 GHz BiCMOS embedded RF-MEMS switch". In: *14th Symposium on RF-MEMS and RF-Microsystems (MEMSWAVE)*. 2013.

Co-authored publications

1. M. Wietstruck, S. Marschmeyer, S. Tolunay Wipf, C. Wipf, T. Voss, M. Bertrand, E. Pistono, G. Acri, F. Podevin, P. Ferrari, and M. Kaynak. "Design Optimization of Through-Silicon Vias for Substrate-Integrated Waveguides embedded in High-Resistive Silicon Interposer". In: *2018 IEEE 20th Electronics Packaging Technology Conference (EPTC)*. Dec. 2018, pp. 195–200.

2. M. Bertrand, E. Pistone, G. Acri, D. Kaddour, F. Podevin, V. Puyal, S. Tolunay Wipf, C. Wipf, M. Wietstruck, M. Kaynak, and P. Ferrari. "Substrate Integrated Waveguides for mm-wave Functionalized Silicon Interposer". In: *2018 IEEE/MTT-S International Microwave Symposium - IMS*. June 2018, pp. 875–878. DOI: 10.1109/MWSYM.2018.8439287.

3. T. Chaloun, F. Tabarani, S. Tolunay Wipf, M. Kaynak, H. Schumacher, and W. Menzel. "A modular phased array transceiver with RF-MEMS SPDT switches in a 0.25 μm SiGe BiCMOS technology". In: *12th European Conference on Antennas and Propagation (EuCAP 2018)*. Apr. 2018, pp. 1–5. DOI: 10.1049/cp.2018.0615.

4. C. Wipf, R. Sorge, A. Göritz, S. Tolunay Wipf, A. Scheit, D. Kissinger, and M. Kaynak. "High voltage LDMOS inverter for on-chip RF-MEMS actuation". In: *2018 IEEE 18th Topical Meeting on Silicon Monolithic Integrated Circuits in RF Systems (SiRF)*. Jan. 2018, pp. 48–50. DOI: 10.1109/SIRF.2018.8304226.

5. P. Rynkiewicz, A.-L. Franc, F. Coccetti, M. Wietstruck, C. Wipf, S. Tolunay Wipf, M. Kaynak, and G. Prigent. "Ring filter synthesis and its BiCMOS 60 GHz implementation". In: *International Journal of Microwave and Wireless Technologies* 10.3 (2018), pp. 291–300. DOI: 10.1017/S1759078718000156.

6. P. Rynkiewicz, A.-L. Franc, F. Coccetti, S. Tolunay Wipf, M. Wietstruck, M. Kaynak, and G. Prigent. "Tunable dual-mode ring filter based on BiCMOS embedded MEMS in V-band". In: *2017 IEEE Asia Pacific Microwave Conference (APMC)*. Nov. 2017, pp. 124–127. DOI: 10.1109/APMC.2017.8251393.

7. P. Rynkiewicz, A.-L. Franc, F. Coccetti, S. Tolunay Wipf, M. Wietstruck, M. Kaynak, and G. Prigent. "Millimeter-wave three-state tunable stopband resonator based on integrated MEMS". In: *2017 IEEE Asia Pacific Microwave Conference (APMC)*. Nov. 2017, pp. 128–131. DOI: 10.1109/APMC.2017.8251394.

8. A. Göritz, S. Tolunay Wipf, M. Wietstruck, M. Kaynak, and A. Mai. "Prozesskontrolle für die Dünnschichtverkapselung von BiCMOS HF-MEMS-Schaltern mittels BEOL-integriertem Pirani-Element". In: *MikroSystemTechnik 2017; Congress*. Oct. 2017, pp. 1–3.

9. M. Kaynak, M. Wietstruck, A. Göritz, S. Tolunay Wipf, M. Inac, B. Cetindogan, C. Wipf, C. B. Kaynak, M. Wöhrmann, S. Voges, and T. Braun. "0.13 μm SiGe BiCMOS technology with More-than-Moore modules". In: *2017 IEEE Bipolar/BiCMOS Circuits and Technology Meeting (BCTM)*. Oct. 2017, pp. 62–65. DOI: 10.1109/BCTM.2017.8112912.

10. P. Rynkiewicz, A.-L. Franc, F. Coccetti, S. Tolunay Wipf, M. Wietstruck, M. Kaynak, and G. Prigent. "Résonateur Bi-Mode Accordable Intégré en Bande Millimétrique". In: *Journées Nationales Micro-Ondes (JNM)*. 2017.

11. S. Lischke, D. Knoll, S. Tolunay-Wipf, C. Wipf, C. Mai, A. Fox, F. Herzel, and M. Kaynak. "Side-use of a Ge p-i-n photo diode for electrical application in a photonic BiCMOS technology". In: *2016 IEEE Bipolar/BiCMOS Circuits and Technology Meeting (BCTM)*. Sept. 2016, pp. 126–129. DOI: 10.1109/BCTM.2016.7738970.

12. M. Wietstruck, W. Winkler, A. Göritz, S. Tolunay Wipf, C. Wipf, D. Schmidt, A. Mai, and M. Kaynak. "0.13 μm BiCMOS embedded On-Chip High-Voltage Charge Pump with Stacked BEOL Capacitors for RF-MEMS Applications". In: *17th Symposium on RF-MEMS and RF-Microsystems (MEMSWAVE)*. 2016.

13. Y. J. Du, W. Su, Y. Li, S. Tolunay, M. Kaynak, R. Scholz, and Y. Z. Xiong. "D-band MEMS switch in standard BiCMOS technology". In: *2015 Asia-Pacific Microwave Conference (APMC)*. Vol. 3. Dec. 2015, pp. 1–3. DOI: 10.1109/APMC.2015.7413319.

14. M. Kaynak, M. Wietstruck, C. B. Kaynak, S. Tolunay, A. Göritz, and B. Tillack. "Modular extension of high performance SiGe BiCMOS technologies - Following the More-than-Moore path". In: *2015 Asia-Pacific Microwave Conference (APMC)*. Vol. 1. Dec. 2015, pp. 1–3. DOI: 10.1109/APMC.2015.7411742.

15. Y. J. Du, W. Su, S. Tolunay, L. Zhang, M. Kaynak, R. Scholz, and Y. Z. Xiong. "220GHz wide-band MEMS switch in standard BiCMOS technology". In: *2015 IEEE Asian Solid-State Circuits Conference (A-SSCC)*. Nov. 2015, pp. 1–4. DOI: 10.1109/ASSCC.2015.7387512.

16. V. Valenta, H. Schumacher, S. Tolunay Wipf, M. Wietstruck, A. Göritz, M. Kaynak, and W. Winkler. "Single-chip transmit-receive module with a fully integrated differential RF-MEMS antenna switch and a high-voltage generator for F-band radars". In: *IEEE Bipolar/BiCMOS Circuits and Technology Meeting*. Oct. 2015, pp. 40–43. DOI: 10.1109/BCTM.2015.7340564.

17. A. Göritz, M. Lisker, S. Tolunay, M. Wietstruck, and M. Kaynak. "Wafer-Level Encapsulation for BiCMOS embedded RF-MEMS Application". In: *International Conference on Micro and Nano Engineering (MNE)*. 2015.

18. A. Strodl, S. Tolunay, V. Valenta, M. Kaynak, S. Reyaz, R. Johnson, W. Winkler, R. Malmqvist, and H. Schumacher. "RF-MEMS Switched W-Band mm-Wave Passive Imaging System in a 0.13 μm SiGe BiCMOS Technology". In: *16th Symposium on RF-MEMS and RF-Microsystems (MEMSWAVE)*. 2015.

19. M. Wietstruck, G. Kahmen, A. Göritz, S. Tolunay, B. Tillack, and M. Kaynak. "Reliability of BiCMOS embedded MEMS Varactors for Wideband RF VCO Applications". In: *16th Symposium on RF-MEMS and RF-Microsystems (MEMSWAVE)*. 2015.

20. M. Kaynak, M. Wietstruck, C. B. Kaynak, A. Göritz, S. Tolunay, and B. Tillack. "MEMS - BiCMOS monolithic integration". In: *2014 XXXIth URSI General Assembly and Scientific Symposium (URSI GASS)*. Aug. 2014, pp. 1–4. DOI: 10.1109/URSIGASS.2014.6929473.

21. M. Wietstruck, M. Kaynak, A. Göritz, S. Tolunay, and B. Tillack. "Accurate Contact Analysis of a BiCMOS Embedded Capacitive-Type RF-MEMS Switch". In: *15th Symposium on RF-MEMS and RF-Microsystems (MEMSWAVE)*. 2014.

22. M. Wietstruck, M. Kaynak, St. Marschmeyer, A. Göritz, S. Tolunay, and B. Tillack. "Monolithisch-integrierte Through-Silicon Vias für Grounding, Power Distribution Networks und System-on-Chip Anwendungen". In: *MikroSystemTechnik 2013; Congress*. Oct. 2013, pp. 1–4.

23. M. Wietstruck, M. Kaynak, St. Marschmeyer, A. Göritz, S. Tolunay, S. Kurth, and B. Tillack. "High-Frequency Optimization of BiCMOS Embedded Through-Silicon Vias for Backside-Integrated MEMS". In: *14th Symposium on RF-MEMS and RF-Microsystems (MEMSWAVE)*. 2013.

24. A. Göritz, M. Fraschke, J. Drews, M. Wietstruck, S. Tolunay, M. Kaynak, and B. Tillack. "Anwendung eines HF-Gasphasenätzprozesses zum Freilegen von mono-

lithisch integrierten RF-MEMS-Schaltern". In: *MikroSystemTechnik 2013; Congress*. Oct. 2013, pp. 1–3.

List of Figures

List of Tables

Erklärung

Ich erkläre hiermit, dass die vorliegende Arbeit von mir selbst und ohne fremde Hilfe verfasst wurde. Alle benutzten Quellen sind im Literaturverzeichnis angegeben. Die Arbeit hat in gleicher oder ähnlicher Form noch keiner Prüfungsbehörde vorgelegen.

Frankfurt(Oder), den